Investigation of Light-Matter Interactions for Single Event Effects Testing in Microelectronic and Photonic Devices

By

Landen Daniel Ryder

Dissertation
Submitted to the Faculty of the
Graduate School of Vanderbilt University
in partial fulfillment of the requirements
for the degree of
DOCTOR OF PHILOSOPHY
In
Electrical Engineering
June 30, 2021
Nashville, Tennessee

Approved:

Sharon M. Weiss, Ph.D
Robert A. Reed, Ph.D
Ronald D. Schrimpf, Ph.D
Andrew L. Sternberg, Ph.D
Joshua D. Caldwell, Ph.D

“From a long view of the history of mankind—seen from, say, ten thousand years from now—there can be little doubt that the most significant event of the 19th century will be judged as Maxwell’s discovery of the laws of electrodynamics…”

- Richard P. Feynman

ACKNOWLEDGEMENTS

Science is a collaborative endeavor, and given the interdisciplinary nature of this work, there is no shortage of people that have impacted my time at Vanderbilt. Principally, I thank my advisor, Dr. Sharon Weiss, not only for her technical knowledge, but also her patience and willingness to “hear me out on this one”. I would also like to extend my gratitude to my committee members for providing the wide-ranging expertise to guide this work.

During my time in graduate school, I have been fortunate to have worked with many graduate students that have both contributed to my technical knowledge but also the enjoyment of my time in graduate school. I would like to extend my gratitude to Dr. Kevin Miller, Dr. Francis Afzal, Sam Halimi, and Josh Allen for the countless hours spent toiling against the optical simulation tools that at times seemed to be actively resisting use in this work. From the radiation effects side of this work, I am thankful for the opportunity to have worked alongside Dr. Andrew Tonigan, Dr. Rebekah Austin, Rachel Brewer, and Brandon Smith. Finally, I would like to thank my colleague and wife, Kaitlyn Ryder, for her support and experimental expertise.

As research is not free, I would also like to extend my gratitude to the Defense Threat Reduction Agency’s basic research program for funding this work.

Table of Contents

Acknowledgements iii

List of Tables vii

List of Figures viii

I. Introduction 1

II. Overview of Radiation Effects 4

A. Natural Space Radiation Sources 4

B. Radiation Degradation 7

1) Single Event Effects 8

2) Total Ionizing Dose 12

3) Displacement Damage 14

III. Optics for Pulsed Laser Single Event Effects Testing and Photonic Devices 17

A. Electromagnetics 17

B. Absorption 19

C. Nonlinear Optics 23

D. Focused Beam Propagation 25

E. Integrated Photonics 27

1) Waveguides 27

2) Photon Sources 28

3) Interferometric Devices 29

4) Modulators 32

5) Radiation Effects in Integrated Photonic Systems 34

IV. Pulsed Laser Single Event Effects Simulation Infrastructure 39

A. Relevant Physics 40

1) Nonlinear Optical Processes 41

2) Charge Transport Solvers 43

3) Simulation Output 44

B. Demonstration 46

1) Test Structure 46

2) Experimental and Simulation Inputs 47

3) Comparison with Experiments 48

C. Other Applications 51

1) Correlation of PL-SEE and Heavy Ion Measurements 51

2) PL-SEE Testing of Silicon Power MOSFET 51

D. Comparison with Existing Methodologies 52

E. Looking Forward 53

V. Nanophotonic Effects in PL-SEE Measurements of FinFETs 55

A. Introduction 55

B. Experimental Setup 57

C. Measurements 58

D. Discussion 61

E. Mechanism 64

1) Optical Simulations 65

F. Conclusions 69

VI. Pulsed Laser Single Event Effects Testing of Waveguide-Integrated Photodiodes 71

A. Introduction 71

B. Experimental Setup 73

C. Measurements 75

D. Discussion 77

1) Device Physics Simulations 80

2) Potential Mitigation Approaches 83

E. Conclusion 85

VII. Radiation-Induced Transient Optical Response of Photonic Devices 86

A. Radiation-Induced Optical Response 86

B. Modeling 88

C. Charge Transport 93

D. Mitigation Techniques - Waveguide Geometries 98

E. Photonic Integrated Circuits 100

1) Passive Ring Resonator Filter 101

2) Mach-Zehdner Modulator 103

3) PL-SEE Testing 105

F. Conclusion 106

VIII. Conclusions and Future Work 107

References 109

LIST OF TABLES

III.1 Bandgap energies and electron-hole pair generation energy for a small subset of semiconductor materials.......... 22

III.2 Gaussian optics parameters.......... 27

V.1 Table of effective refractive index of the GSP optical mode supported by the fin structure computed by independent methods. The agreement between the methods affirms the potenital for SPPs to contribute to optical energy deposition from PL-SEE testing of FinFET devices. 68

LIST OF FIGURES

II.1 Proton flux distributions as a function of altitude for various energies trapped within Earth's Van Allen Belt 5
II.2 Production of secondary particles induced by a galactic cosmic ray colliding with a particle in the Earth's atmosphere 6
II.3 Solar flare captured by CCD image arrays on SOHO (Left). Solar particles arrive at the satellite and disrupts proper pixel operation (Right) 7
II.4 An ionizing particle passing through a p-n junction creates electron-hole pairs that are collected by drift and diffusion processes. These collection processes can be observed based in the single event transient measured on the contact 8
II.5 LET curves as a function of depth in silicon for 690 MeV copper atom (blue) and a 1.3 GeV xenon ion (red). Note that for both ions the LET initially increases with depth material before reaching a maximum LET (Bragg Peak) before decreasing and eventually stopping in the silicon. Data is generated with CRÈME 9
II.6 Notional scaling for gate charge in an inverter as a function of the technology node (feature size). It can be seen that as the feature sizes decrease the amount of charge that is responsible for storing information also decreases, resulting in increased sensitivity from charge deposited from ionizing particles 11
II.7 Energy band illustration of the creation of bulk trapped charge and interface traps from ionizing particles in an oxide 13
II.8 The fractional yield of unrecombined holes as function of applied electric field in silicon dioxide from common ionizing radiation sources. Ionizing radiation interacting with silicon dioxide with minimal electric field applied will experience a low fractional yield of unrecombined holes 14
II.9 (a) Illustration of potential isolated defects in Si induced by an incident particle. (b) Representation of the initial defect configuration related to the energy of the primary knock on-atom in Si 15
II.10 Depiction of defect energy states and an associated device degradation mechanism: a) defect-assisted thermal generation, b) defect-assisted recombination, c) defect-assisted carrier trapping, d) doping compensation, and e) defect-assisted tunneling 16
III.1 Band structure of silicon (left) and gallium arsenide (right) depicting an indirect and direct bandgap material respectively 20
III.2 Simplified depiction of interband transition (left) and intraband transistions (right) 21
III.3 Absorption spectra of silicon with a variety of doping densities. Note that absorption for the undoped silicon falls off the at the bandgap energy, but doped silicon is absorptive to photons with sub-bandgap energies 23
III.4 Simplified depiction of single photon absorption (left) and two photon absorption (right). Note that TPA can occur with photons with energy less than the bandgap 24
III.5 Intensity contours (Eqn. III.12) for a focused Gaussian beam where the red curves mark the e^{-2} decay from the on-axis intensity. The labeled variables are provided in Table III.2 26
III.6 Electric field intensity spatial distribution in a silicon ridge waveguide for the fundamental TE and TM modes. Note that in the case of the TM mode, there is significant electric field located in the cladding material 28
III.7 A schematic of a simple MZI. The transmission of the MZI as a function accumulated phase in one of the arms. 30
III.8 A schematic of a simple ring resonator with bus waveguide. The transmission of a ring resonator as a function accumulated phase. 31

III.9 Schematics for phase shifters using three different carrier modulation techniques. The dashed lines denote the location of the waveguide intersection with the modulator region (a) Carrier depletion through reverse biasing p-n junction. (b) Carrier injection through a forward bias p-i-n junction. (c) Carrier accumulation from a thin oxide region separating a p-doped and n-doped region 33
III.10 Schematic representation of an optical transceiver/receiver implementation with different photonic and electronic components necessary to function. 35
IV.1 Schematic of PL-SEE measurement system at Vanderbilt University. The optical simulations capture all components related to the laser pulse in the system. Charge collection simulators are responsible for electrical components of the measurement setup 41
IV.2 Flow chart of the PL-SEE simulation infrastructure discussed in this chapter 45
IV.3 The large area epitaxial silicon diode used as test vehicle for comparing the simulation infrastructure with PL-SEE measurements. Note the hole in the topside of the diode allows for topside access for the laser pulse 47
IV.4 Cross-sectional cuts optically generated charge densities that result from a 400 pJ pulse at focal positions: 0 μm (surface), 10.5 μm, and 24.5 μm. The arrow indicates the direction of the laser pulse propagation. Note that changing the focal position of laser pulse changes the spatial distribution of charge in the silicon diode 49
IV.5 Experimental and simulated transients for a 990 pJ focused at the surface of the diode for -5 V (left) and -90 V (right) 50
IV.6 Depth scans of the silicon diode for pulse energies of 400 pJ and 750 pJ for two reverse bias conditions: -5 V (left) and -90 V (right). Experimental error bars represent one standard deviation based on 200 collected transients 50
V.1 Topside view of the FinFET device structure under test with associated dimensions provided 57
V.2 Modified PL-SEE measurement system. The waveplate is added after any polarization-dependent optical components to ensure that no polarization-dependent losses in the laser pulse are introduced 58
V.3 (A) Voltage response [V] as a function of polarization angle rotation for a power meter placed at the DUT location in the measurement system. Uniform response shows there are no polarization dependent losses in the measurement system. The two measurements at 200 degrees represent the initial and final polarization angle measured. (B) Average peak photodiode response [V] as a function of polarization angle. Photodiode response is used to monitor the energy of individual pulses during measurements. Uniform response shows there is no variation in pulse energy over the course of the measurement 59
V.4 (A) Average peak current response [mA] of the 40 nm fin width FinFET as a function of polarization angle. Error bars represent one standard deviation of the collected transients. Initial rotation angle is 120 degrees. (B) Average peak current response [mA] of the 30 nm fin width FinFET as a function of polarization angle. Error bars represent one standard deviation of the collected transients. Initial rotation angle is 70 degrees 60
V.5 Average peak current response [mA] of the large area silicon diode as a function of polarization angle. Error bars, representing one standard deviation of the collected transients, fall within the extent of the data point 61
V.6 Device under test in high-speed packaging used for transient capture. Device orientation are estimated relative to the features on the package itself. These package 62

features are then used to estimate the orientation relative to features on the optical measurement system, where the polarization of the light is known ....

V.7 The two polarization directions in this work are defined by the geometry of the device, as shown with respect to the fin cross-section. Note that the field direction is directed out of the page in the right image 63

V.8 Normalized cross-section of optical energy density squared induced in a single silicon fin structure from optical simulations to estimate distribution of optically generated charge. White symbols in the lower right corner of each plot indicate the direction of electric field polarization. Color bar scales are equivalent 66

V.9 Normalized cross-section of the electric field intensity induced in a single elongated silicon fin structure. Note the interference fringes associated with reflections from the metallization at the top of the fin. White symbols in the lower right corner of plot indicates the direction of electric field polarization... 67

V.10 An visual representation of the impact of package placement relative to the polarization direction of light from the measurement setup 68

VI.1 Cross-sectional cut of waveguide integrated photodiodes for LPIN, VPIN device geometries considered in this work. In standard operation, the optical signal propagates perpendicular to these cross-sections. White dashed lines denote the direction of the electric field lines in germanium. 74

VI.2 Full-width half-maximum (FWHM) of SETs collected as a function of laser pulse energy under four bias conditions: -0.5 V, -1.0 V, -1.5 V, -2.0 V. Device labels correspond to dimensions outlined in Fig. VII.1. 76

VI.3 SETs as a function of bias for the same laser pulse energy (500 pJ) for LPIN (left) and VPIN (right)... 77

VI.4 FWHM of SETs as a function of pulse energy for all devices under the same bias condition. 79

VI.5 Schematic diagram of the simplified LPIN and VPIN photodiodes that were used in transient TCAD simulations. Doped regions used a dopant density of 10^{19} based on similar structures in literature 81

VI.6 Electric field distributions of the photodiodes under two bias conditions: -0.5 V and -2.0 V. For the LPIN device, increasing the bias results in an increased electric field amplitude in the germanium for charge collection. In the case of the VPIN device, there is a strong electric field across the germanium even at low bias. 82

VI.7 FWHMs of simulated SETs in VPIN and LPIN photodetectors as a function of charge injection under four bias conditions: -0.5V, -1.0V, -1.5V, -2.0V. Note that the LPIN devices demonstrate the similar trend of dependence on the injected charge on the induced device response. 83

VI.8 Simulated SETs as a function of bias for the same charge injection conditions (1 pC/μm) for VPIN and LPIN devices. Note that the simulated SETs demonstrate the same bias-dependent behavior that was observed during PL-SEE testing. As these are 2D simulations, the normalization length used was 1 μm. 83

VII.1 a) A diagram of a silicon ridge waveguide with the waveguide width and height denoted as the WW and HH. Light confined to the waveguide will propagate along the along the waveguide in the z-direction. b) The optical mode profile for a TE mode supported by a waveguide with dimensions of WW = 450nm and WH = 220 nm. c) A plot of the optical mode along the dashed line in (b) with the dotted lines corresponding to the Si/SiO_2 interface. Note that the optical mode practically extents into the surrounding oxide and is not uniformly distributed within the waveguide....................................... 87

VII.2 (Top) Radiation-induced phase shift and (bottom) change in transmission in reference to standard operation. Data points represent results from 3D FDTD simulations and solid lines represent effective index perturbation calculations. 92
VII.3 Radiation-induced change in transmission in a ridge waveguide for charge deposited of 22 fC, 110 fC and 220 fC (equivalent to a particle LET of 10, 50, and 100 MeV•cm^2/mg) with a width of σ = 10 nm. Charge injection occurs at 100 ps. 94
VII.4 A linecut of the hole density along the width of the waveguide (dashed lines correspond to silicon boundary) at injection and 5 ps after injection of charge equivalent to a particle LET of 50 MeV•cm^2/mg. The prompt lateral diffusion reduces the peak electron density, resulting in a more uniform distribution of carriers. 95
VII.5 a) Peak hole density and b) Transmission for an injection event with an equivalent charge of a particle with an LET of 10 MeV•cm^2/mg injected at 100 ps for four different widths: 10 nm, 50 nm, 100 nm, 200 nm. Though there is an initial difference in the device response, the prompt lateral diffusion results across the waveguide results in equivalent device response on the order of picoseconds. Subsequent charge movement is longitudinal and as the deposited charge will remain in the waveguide core, the response remains consistent. The dotted line notionally separates the two diffusion regimes. 96
VII.6 Transmission as function of the width of the charge distribution for total charge deposited of 22 fC, 110 fC and 220 fC, corresponding to charge deposited from particles with an LET of 10 MeV•cm^2/mg, 50 MeV•cm^2/mg, and 100 MeV•cm^2/mg respectively. As the width of the distribution increases, the transmission asymptotically approaches a transmission value consistent with a uniform density of carriers in the waveguide. This behavior is analogous to the transmission response of the device in time as the carriers diffuse in the waveguide.. 97
VII.7 a) Cross-sectional cut of a rib waveguide. In addition to the width (WW) and height (WH) of the waveguide, the slab height (SH) is a device dimension that impacts the optical mode. b) An optical mode of rib waveguide with WW = 450 nm, WH = 220 nm, and SH of 100 nm. c) Charge deposited in the waveguide core can diffuse into the silicon and delocalize from the mode. Note the presence of the field in the silicon slab as the mode is less confined. The black box notionally defines the waveguide for comparisons. 99
VII.8 The radiation-induced response from an ionizing particle with an LET of 50 MeV•cm^2/mg is examined for a ridge waveguide and rib waveguide with three different slab heights: 50 nm, 100 nm, 150 nm. a) Charge in the waveguide core (black box in Fig. VIII.7) normalized to the total deposited charge and b) The transient response of the transmission of the waveguide. As the slab allows for carriers to diffuse away from the waveguide core, the duration of the transient will be decreased............................ 100
VII.9 Ring resonator used as wavelength filter. On-resonance wavelength light (purple arrow) passes through the ring to the "Drop" port while non-resonant wavelength light (red arrow) passes to the "Through" port of the device.……………………………… 102
VII.10 Transmission of an on-resonance signal at the Through and Drop ports of the ring resonator filter as a function of the charge injected into the waveguide. Note that as the charge increases, the resonance of the ring shifts, resulting in the signal becoming routed through the incorrect port. 102
VII.11 A schematic of a Mach-Zehnder modulator with active phase in the bottom arm. An input continuous wave (CW) signal is input into the device and a voltage signal is encoded onto the device. The impact of the device response for a particle strike (red x) at the input and at the arm is considered... 103

VII.12 The change in transmission of the MZM as function of time for a particle strike at two locations: the input (red) and the arm (blue). For this operating condition, the strike at the arm results in a greater decrease in transmission than for a strike at the input as the radiation-induced phase shift also impacts the interferometric behavior of the MZM. . 104
VII.13 Transmission as a function of pulse energy for TPA charge injection for three spot size (e^{-2}): 1.7 μm, 3.4 μm, and 5.0 μm. Note that increasing the beam spot size increases the threshold pulse energy. 105

CHAPTER I

INTRODUCTION

On October 4th, 1957 the Soviet Union launched the Sputnik 1 satellite, capturing the distinction as the first man-made object to orbit the earth. This event stands as the start of the Space Age that has seen lunar landings, deep space probes, and droves of earth orbiting satellites. Space-based systems touch almost every facet of life from telecommunication to meteorology and earth sciences to military applications with some estimates of the number of operational satellites in the thousands [1]. Given both the immense cost and criticality of these space-based systems, great care is taken to ensure reliable operation for the entirety of the mission lifetime. While there are many factors that qualify the space environment as a hostile environment compared to terrestrial environments, the bombardment of energetic particles is of particular concern to the electronic and photonic devices onboard. To ensure that space-based systems are able to survive their harsh operating environments, preliminary ground-based testing is commonly performed to assess the sensitivity of the system and estimate the likelihood of mission failure to radiation-induced degradation.

The space radiation environment results in both cumulative degradation over the mission lifetime and instantaneous effects introduced by single energetic particles, referred to as single event effects (SEEs). As a broad class of radiation effects, SEEs can be responsible for a variety of errors in system operation such as a temporary distortion of a signal state, potentially creating bit flip in a data stream or memory architecture, to more sustained effects such as latch up and gate rupture that can irreparably damage devices. As microelectronic feature sizes and nodal capacitances decrease, more particles in the space environment can deposit enough charge to induce an SEE within a device, requiring greater amounts of test data to reliable quantify risk for designers. To further complicate this, the adoption of new technologies like integrated photonics require extensive characterization efforts prior to integration into space-based applications.

The ever-expanding space industry coupled with a relatively short supply of test hours at high energy particle facilities has led to the examination of alternative means to perform SEE testing with more available facilities. One such popular technique is pulsed-laser single event effects (PL-SEE) testing which intends to imitate the ion-induced SEE response of a device with

an ultrafast laser pulse. Given that PL-SEE testing relies on optical absorption from a focused laser pulse, it is unsurprising that the spatial extent of energy deposited by pulsed laser is significantly different than that from an ionizing particle. This work focuses on the exploration of charge injection using pulsed lasers in lieu of ionizing particles on both microelectronic and photonic devices, creating simulation tools to better describe and predict the results seen in PL-SEE measurements.

Chapter II provides an introduction to the naturally occurring radiation sources that make up the space radiation environment as well as an overview of the physical mechanisms underpinning the three broad categories of radiation-induced device degradation: single event effects, total ionizing dose, and displacement damage. Though this work will focus on SEE in microelectronic and photonic devices, the physical mechanisms that underpin total ionizing dose and displacement damage are also discussed for sake of completeness.

As essentially every chapter in this work is related to light-matter interaction, **Chapter III** contains a general description of light-matter interaction, nonlinear optics, and beam propagation that provides the groundwork for simulation approaches discussed in future chapters. Furthermore, the relative lack of radiation effects characterization on photonic devices necessitates a general overview of integrated photonic devices and potential radiation sensitivities. **Chapter IV** describes the PL-SEE simulation infrastructure that was developed to directly simulate the current transient measured from a microelectronic device during testing. The application of this simulation infrastructure as well as how this tool compares with other methodologies for simulating PL-SEE measurements is discussed. **Chapter V** details PL-SEE measurements conducted on silicon-on-insulator (SOI) FinFETs that demonstrated a dependence on the polarization of the laser light with respect to the device orientation. This dependence is due to energy enhancement from excitation of surface plasmons within the fin structure of the device, an effect demonstrated with simulations prior to measurements.

In the latter portion of this work, the SEE response of integrated photonic devices are considered. **Chapter VI** documents PL-SEE measurements on two geometries of waveguide-integrated germanium photodiodes that would be used for signal conversion in a silicon photonics system. It was demonstrated that the photodiode geometry critically impacts the radiation response, consistent with the behavior seen during standard operation. Rather than characterizing the electrical transient as has been done in the previous chapters, **Chapter VII** focuses on an

exploration of the radiation-induced optical response of a photonic waveguide. A computationally efficient simulation approach to estimating the radiation-induced optical response of photonic waveguide is discussed and used to examine the charge transport mechanisms that drive the optical response of a device. Furthermore, the impact of using alternative testing techniques that do not match the charge profile from an ionizing particle are discussed. Finally, **Chapter VIII** highlights important conclusions from this work and provides thoughts for future work related to the impact of PL-SEE testing in microelectronic and photonic devices.

CHAPTER II

OVERVIEW OF RADIATION EFFECTS

Spacecrafts must be designed to withstand a variety of environmental hazards such as micro-meteoroids, man-made debris, high-energy photons, and high-energy particle radiation. The naturally occurring radiation environment in space can actively degrade materials, impacting the performance of critical microelectronic and optical devices. To develop reliable and cost-effective space-based systems, extensive efforts have focused on 1) the identification of the natural radiation sources and 2) accurate climatology models of the space radiation environment informed by data collected by science payloads on a variety of spacecrafts. Following an accurate forecast of the radiation environment, the total impact of the radiation environment can be considered and appropriate mitigation techniques (shielding, redundancy, etc.) can be applied to ensure system reliability while minimizing costly and unnecessary overhead [2]–[4]. In this chapter, a brief introduction to the naturally occurring space radiation environment and the associated material and device degradation mechanisms is provided.

A. Natural Space Radiation Sources

The origin of very high energy galactic cosmic rays is believed to be collapsed supernovae. These very high energy particles that bombard Earth are formed during nuclear fusion processes (i.e., lighter elements combining to form heavier elements) within distant stars that are then accelerated towards our solar system during their birth star's collapse [5]. Nuclear reactions at the core of the star produce the necessary energy to remain active through conversion of lighter elements like hydrogen into increasingly heavier elements. Iron represents an inflection point in the nuclear fusion process ongoing within stars, as the conversion of iron into heavier elements is endothermic rather than the previously exothermic processes. As the core begins to cool, and the excess fusion energy begins to diminish, gravity will eventually cause the collapse of the star. The galactic cosmic ray (GCRs) spectrum mainly consists of hydrogen (~90%), helium (~9%) and

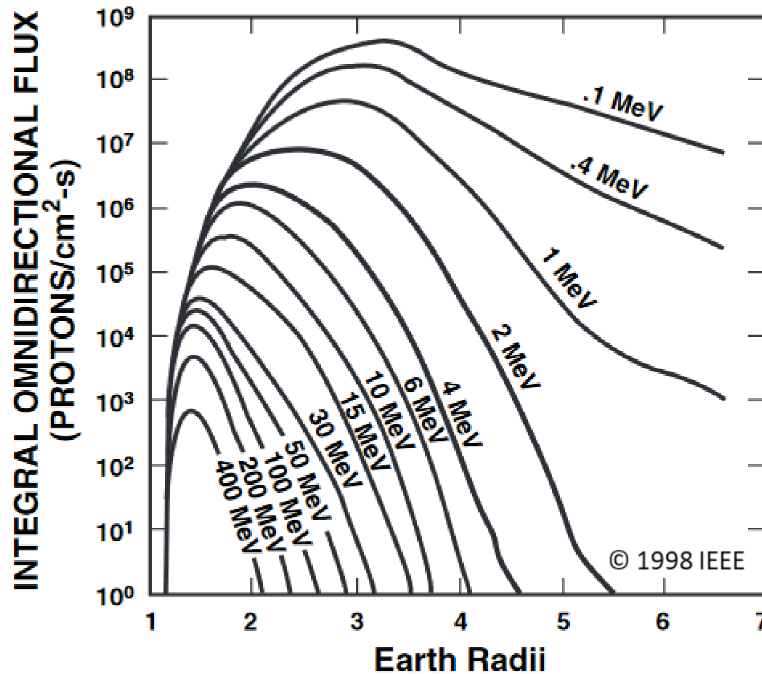

Figure II.1. Proton flux distributions as a function of altitude for various energies trapped within Earth's Van Allen Belt. After [7].

other lighter elements, with a very notable drop in prevalence of elements heavier than iron, commonly referred to as the iron knee [6].

In 1958, the United States launched the Explorer 1 and Explorer 3 satellites with the intention of detecting GCRs, but instead discovered the presence of a belt of charged particles trapped by the magnetic field of the Earth that saturated the onboard detectors. These trapped charged particles, called the Van Allen Belts, exist over a wide range of altitudes with a spectrum of particle energies that fluctuate based on solar activity and cosmic ray fluctuations (Fig. II.1) [7]. Since the trapped charged particles are a consequence of the magnetic field of a cosmic body, earth is not the only planet that exhibits this class of radiation environment. The strong magnetic field of Jupiter has resulted in an infamous trapped radiation environment that has drawn extensive interest since the Pioneer spacecraft provided the first measurements of the Jovian environment captured on its way to interstellar space.

First observed in the 1940s by ground-based detectors, the sun can be a source of highly energetic particles (predominantly protons) that are emitted from the sun in the form of the solar winds or during coronal mass ejections. As GCRs and solar particles bombard the Earth's

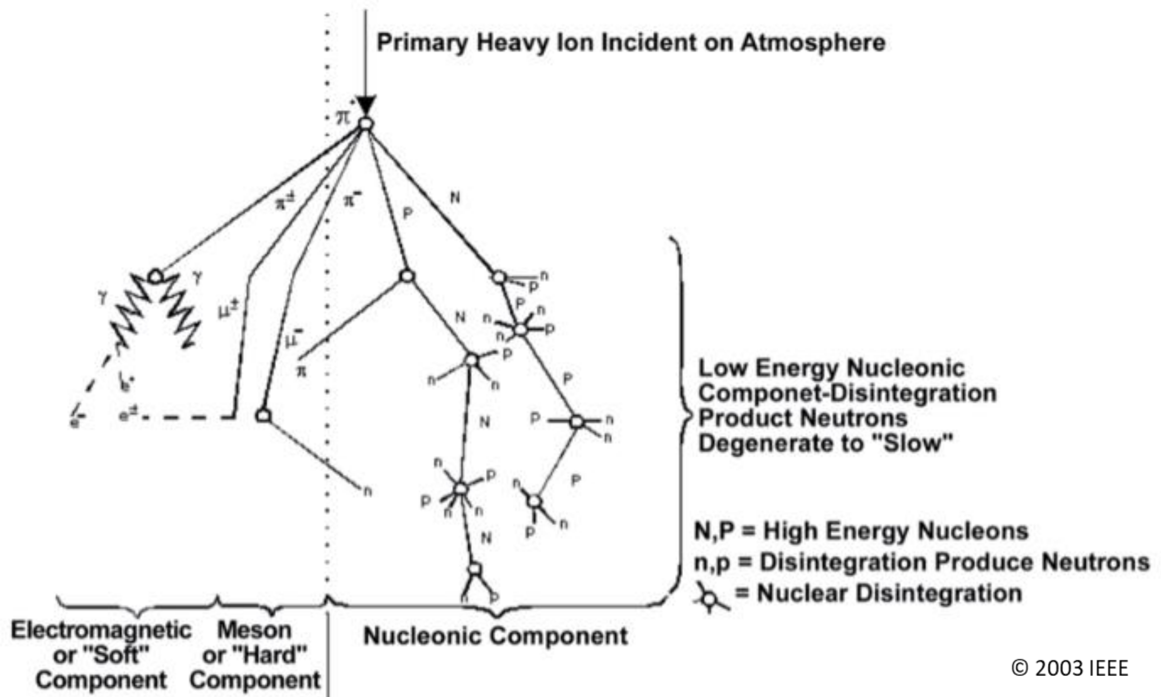

Figure II.2. Production of secondary particles induced by a galactic cosmic ray colliding with a particle in the Earth's atmosphere. After [8].

atmosphere, collisions with atomic nuclei and electrons result in the production of secondary particles such as protons, neutrons, muons, and pions (Fig. II.2) [8]. These secondary particles can reach ground level, contributing to the terrestrial population of these particles. While these solar processes can occur at any time, solar activity cycles through solar maximums and minimums with an approximately eleven-year period that result in the fluctuation of the radiation environment over the mission lifetime of a system [9].

Overall, these naturally occurring radiation sources present a reliability concern for microelectronics operating in a space environment. One of the most recognizable demonstrations of the impact of radiation on an environment is the interaction of ionizing particles on image sensors. The Solar and Heliospheric Observatory (SOHO) satellite is a collaboration between international space agencies to observe a variety of solar processes which includes the use of charge-coupled device (CCD) imaging arrays to capture images of coronal mass ejections. In the event that the satellite is in the path of the solar energetic particles produced by the coronal mass ejection, the charged particles will strike the imaging arrays and disrupt nominal operation by creating white streaks in the measured image (Fig. II.3) [10]. Given the cost associated with

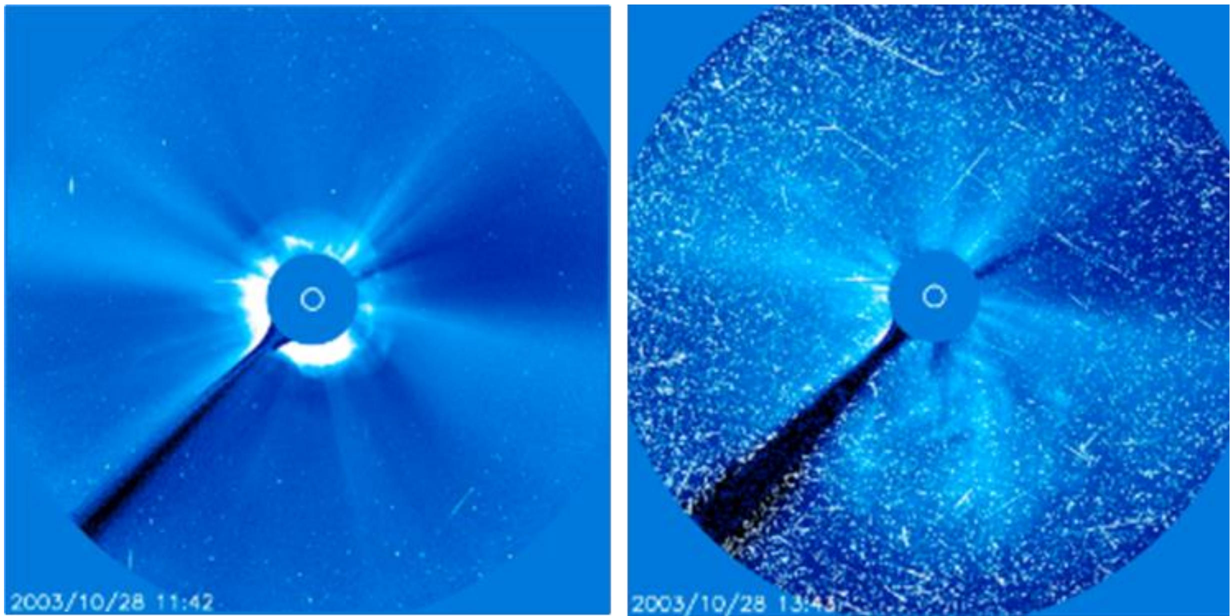

Figure II.3. Solar flare captured by CCD image arrays on SOHO (Left). Solar particles arrive at the satellite and disrupts proper pixel operation (Right). After [10].

deploying spacecraft and minimal maintenance capacity, development of reliable, radiation-tolerant systems is necessary for space-based applications.

B. Radiation Degradation

Data driven models are critical for assessing the radiation environment that a space-based system must operate in, requiring orbital information and mission lifetime to estimate the impact of the solar cycle on the radiation environment. While each radiation source is independently modelled, simulation packages such as Cosmic Ray Effects on MicroElectronics (CRÈME96) [11]–[13] and The Space ENVironment Information System (SPENVIS) [14] provide the total contribution of each radiation source as a spectra of particle species and energies for a given orbital trajectory and timeframe. The potential for radiation-induced degradation for a given particle is largely dependent upon its species and energy, therefore accurate accounting of the spectra of these particles is critical for accessing the total degradation expected within a device or system. The variety of radiation effects that can impact device performance is discussed in the following sections.

1) Single Event Effects

Single event effects represent a classification of radiation effects centered on the impact of an individual ionizing particle passing through the sensitive regions of devices. Although certain device geometries and operating conditions can result in vulnerability to destructive, long-term modifications to device behavior (i.e., burn-out, latch-up, gate rupture), this work focuses on the exploration of non-destructive transient effects from single ionizing particles.

Charge collection during a single ionizing particle event is commonly decomposed into three distinct physical processes based on response time [15]–[18]. An individual high energy particle (typically a heavy ion) passing through a material will primarily dissipate energy through Coulombic interactions that result in a dense track of electron-hole pairs along its trajectory. This track of plasma represents a system that is out of thermal equilibrium and must return to equilibrium (i.e., thermalization of the electron-hole pairs) through scattering processes with phonons and other electrons. Following thermalization, electron-hole pairs deposited in a region with an electric field are subject to prompt collection via drift (order of ps). Electron-hole pairs residing in regions without an electric field can still be collected by slowly migrating to regions with electric fields through diffusion (order on 100s of ps). From a practical perspective, electron-hole pairs are collected on the contacts of a device and result in a current transient that will exhibit temporal behavior related to collection processes. Conceptually, the decomposition into distinct processes is visualized for a p-n junction in Fig. II.4 [15].

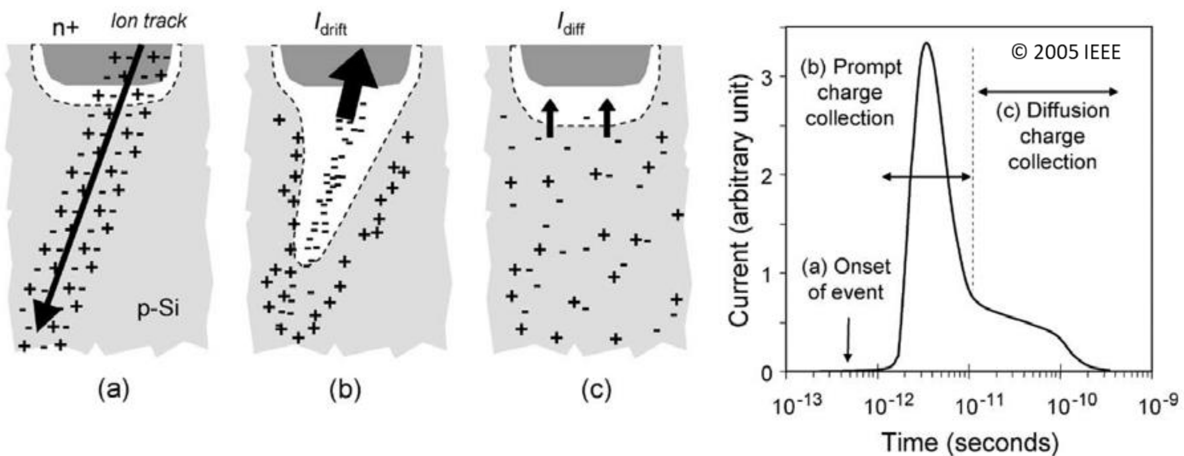

Figure II.4. An ionizing particle passing through a p-n junction creates electron-hole pairs that are collected by drift and diffusion processes. These collection processes can be observed based in the single event transient measured on the contact. After [15].

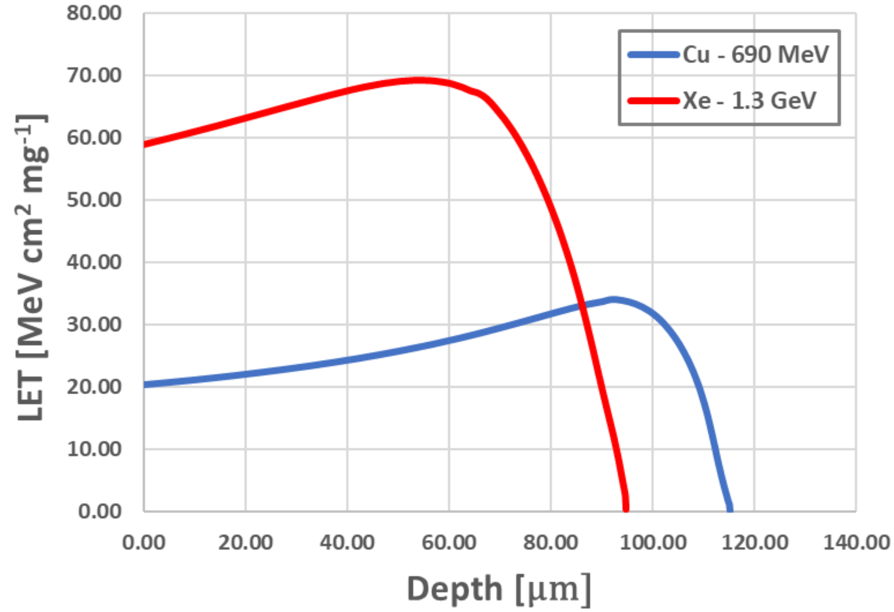

Figure II.5. LET curves as a function of depth in silicon for 690 MeV copper atom (blue) and a 1.3 GeV xenon ion (red). Note that for both ions the LET initially increases with depth in the material before reaching a maximum LET (Bragg Peak) and decreasing until eventually stopping in the silicon. Data was generated with Stopping Range In Matter (SRIM).

The energy dissipated by a particle is dependent upon both the energy and species of the particle, with the rate of energy transfer to the material defined as the linear energy transfer (LET)

$$LET(z) = -\frac{1}{\rho}\frac{dE}{dz} \tag{II.1}$$

where z is the path length of the particle's trajectory in the material, ρ is the density of the material, and $\frac{dE}{dz}$ is the stopping power of the particle. The particle loses energy as it passes through the material and the LET of the particle changes along its trajectory; this is indicated by the functional dependence of the LET on path length. Since lower energy particles tend to dissipate energy at higher rates than higher energy particles, the LET of a particle initially increases as it passes through the material as the energy of the particle decreases from energy dissipation. Eventually, the LET will reach a peak value referred to as the Bragg peak before the LET quickly decreases as the particle has lost the majority of its initial energy. An example of this behavior is shown in Fig. II.5 for 690 MeV copper and 1.3 GeV xenon ions as they pass through a slab of silicon [19].

An ionizing particle will result in an ensemble of free electrons with a distribution of energies in excess of the conduction band energy. These energetic electrons will dissipate energy during thermalization until an equilibrated carrier density can be acted upon by charge collection processes. While it is possible to model the complex behavior of the initially energetic electrons using nuclear physics and band structure-based simulations, the conversion of energy lost by the ion into the charge deposited in the material is typically performed using an empirically determined average electron-hole pair creation energy E_{ehp}. With this conversion factor, the deposited charge Q_{gen} in a region of material can be written as the integral over the length of the region.

$$Q_{gen} = \frac{\rho}{E_{ehp}} \int LET(z)\, dz \quad \text{(II.2)}$$

Not all deposited charge in a material contributes to the radiation response of the device. Charge deposited in a junction will likely be collected by the electric field while charge deposited in a doped region away the active region of device may not contribute to the device response at all. To capture this spatial sensitivity of charge collection, a device may be decomposed into sub-regions with an associated collection efficiency, α. These regions are referred to as sensitive volumes and are used with deposited charge curves to express the total collected charge Q_{col} from an ionizing particle in a device [20]–[23].

$$Q_{col} = \int \alpha(z) Q_{gen}(z)\, dz \approx \sum_i \alpha_i Q_{gen,i} \quad \text{(II.3)}$$

Collection efficiencies are typically empirically determined for an individual device; physically-informed sensitive volumes can be combined with an experimentally-measured collected charge and computed LET curves to extract the collection efficiencies. Once sensitive volumes and associated collection efficiencies have been determined, the collected charge from an untested particle can be predicted by applying the sensitive volume to its corresponding LET curve. A central assumption of the sensitive volume approach is that device physics impacting charge generation and collection remain equivalent during its application. Sensitive volumes derived from a particle that results in a tightly collimated track will likely be insufficient when applied to a

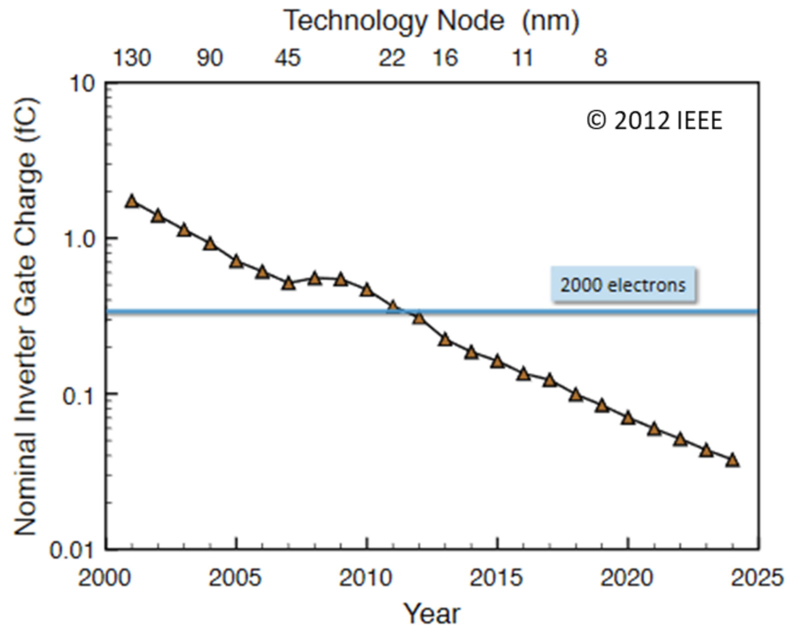

Figure II.6. Notional scaling for gate charge in an inverter as a function of the technology node (feature size). It can be seen that as the feature sizes decrease the amount of charge that is responsible for storing information also decreases, resulting in increased sensitivity from charge deposited from ionizing particles. After [28].

particle that creates secondary ionizing particles along its track (e.g., the charge collection efficiency may vary between drastically different radiation events [22], [24]).

To this point, SEE have been described at a device physics level, as carrier densities are subjected to drift and diffusion processes. The definition of sensitive volumes serves as a vehicle to move up the layers of abstraction to describe radiation effects of circuits and systems. For circuit level SEE modeling, the parameterization of charge injected at a circuit node through sensitive volumes and LET curves can be used as a perturbation of the system, with the resulting system response constituting a radiation response of the system [25]–[27]. In many cases, circuit nodes can sustain operation up to a critical charge threshold, after which operation may be temporarily disrupted. In the event that a circuit was to be operated in a radiation environment, an LET spectrum of the environment can be used in conjunction with calibrated sensitive volumes to identify the flux of particles with LETs that will exceed the critical charge of a node and estimate an error rate [2]. As a general rule, shrinking device feature sizes results in increasing device sensitivities to charge injection (Fig. II.6) [28]. Within the past decade, even individual electrons and muons have been shown to be potentially important contributors to a system's SEE

susceptibility [29]. Therefore, it will become increasingly important to develop radiation hardened by design concepts alongside error detection and correction algorithms to ensure the sustained operation of systems which leverage modern electronics in radiation environments.

2) Total Ionizing Dose

As described in the SEE section above, an ionizing particle passing through a material will generate electron-hole pairs through Columbic interactions with the material. In the case of a non-destructive SEE, the focus is on electron-hole pairs generated in semiconductor material near the active region of the device by particles with sufficient LET to temporarily disrupt the device (heavy ions and high energy protons). However, any ionizing particle can generate electron-hole pairs in a material as long as an amount of energy greater than the bandgap of the material is transferred, including in oxides and insulators. As lower energy ionizing particles dominate the total fluence of particles present in a space environment, the cumulative degradation associated with the total ionizing dose (TID) that a device is subjected to is a concern for reliable device operation (e.g., threshold voltage shifts in transistors). It should be noted that while TID is typically focused on the electron-hole pairs that are generated in oxides and their migration to material interfaces, TID degradation can also be the consequence of electron-hole pairs modifying the charge state of defects within non-insulating materials (e.g., color centers in optical fibers [30]).

Within the field of microelectronics, the ubiquitous example used to describe TID degradation mechanisms centers on the gate oxide in silicon metal-oxide-semiconductor field effect transistors (MOSFETs) [31]–[33]. Electron-hole pairs that are generated from ionizing radiation passing through the gate oxide will either recombine or become spatially delocalized and move through the oxide via drift in accordance with the electric field induced in the oxide from voltage applied by the gate contact. Since electrons have a much greater mobility than holes in the oxide, electrons will escape the oxide quickly while the holes slowly migrate towards a material interface by “hopping” through defect energy states introduced by vacancies and contaminate atoms. As holes interact with these defect energy states they can potentially be “permanently” captured by deep energy defect states, altering the charge state of the defect and creating oxide trapped charge that may perturb the electrostatics of the device. Additionally, interactions with defect energy states that are associated with contaminate hydrogen can result in the release of charged protons in the oxide that readily diffuse towards the material interface. At the interface,

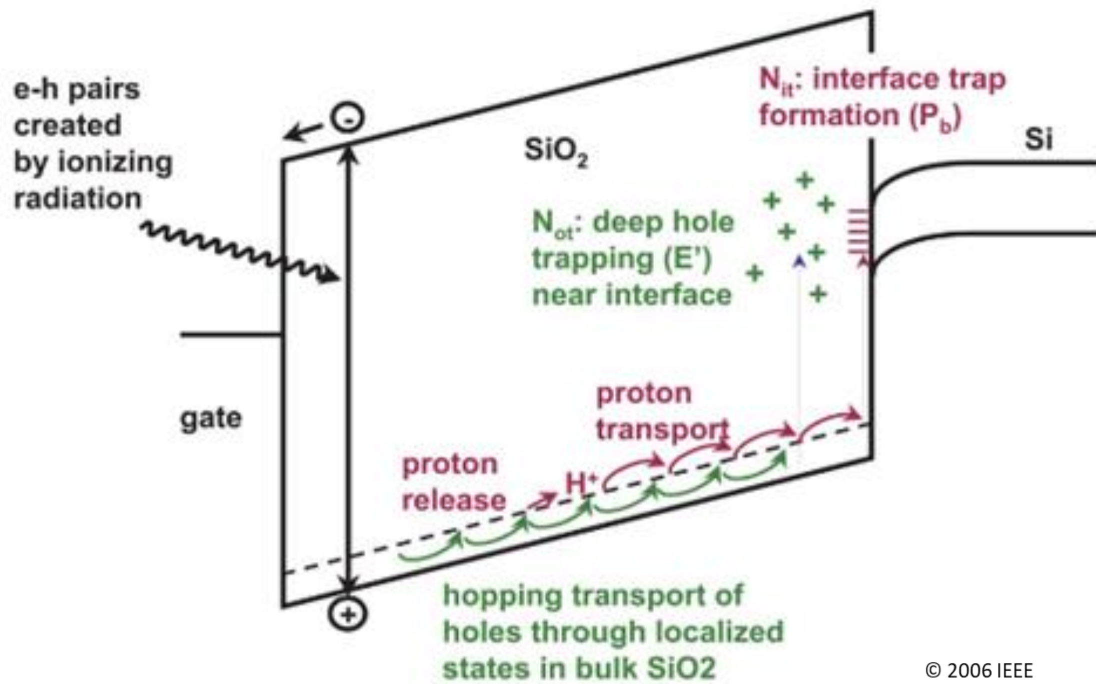

Figure II.7. Energy band illustration of the creation of bulk trapped charge and interface traps from ionizing particles in an oxide. After [31].

the released protons interact with hydrogen-passivated silicon (introduced as a part of common manufacturing techniques) and form dangling silicon bonds that act as interface traps that can also impact device operation [34]. This notional process is illustrated in Fig. II.7 [31].

Following the initial creation of electron-hole pairs in a material via ionization processes, prompt recombination processes reduce the total number of carriers remaining in the materials. Notionally, carrier recombination is a spatially localized process, with increasing carrier densities resulting in an increased availability of potential carriers for recombination. This principle is realized as carrier density-dependent recombination lifetimes, which show a decreasing recombination lifetime for increasing carrier densities. Therefore, the ratio of charge that is not removed via recombination to the total deposited charge (referred to as fractional yield) will be increased as 1) the carrier density from the ionization decreases and 2) the electron-hole pairs are separated via drift and diffusion processes. In the case of oxides, charge separation will be dominated by drift processes, implying that an increasing electric field across an oxide will

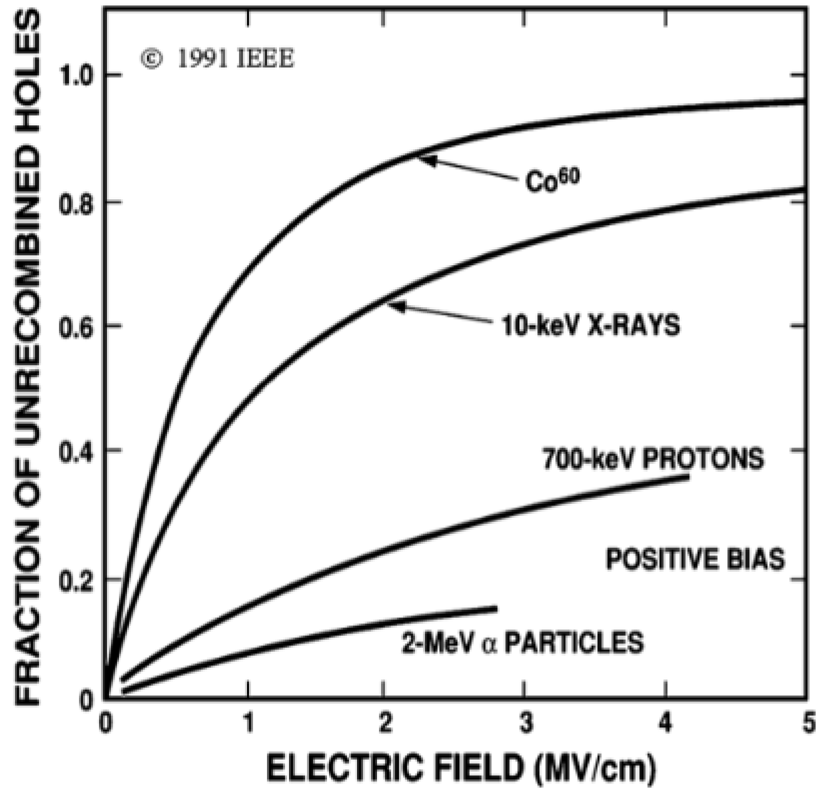

Figure II.8. The fractional yield of unrecombined holes as a function of the applied electric field in silicon dioxide from common ionizing radiation test sources. Ionizing radiation interacting with silicon dioxide with minimal electric field applied will experience a low fractional yield of unrecombined holes. After [31].

increase the fractional yield of an ionization process. A common demonstration of this is provided in Fig. II.8 [31], which depicts the fractional yield in silicon dioxide for different ionization sources as a function of electric field. Since the strength of the electric field is crucial in the fractional yield process, the thickness of the oxide along with bias voltages and internal electric fields are also important factors for estimating the amount of carriers in the oxide that can contribute to total ionizing dose effects.

3) Displacement Damage

An energetic particles incident on a material can dissipate energy through interactions with the crystalline lattice of the material, such as phonon creation and the displacement of atoms through elastic and inelastic collisions with the atomic nuclei (i.e., displacement damage) [35]. Provided that the incident particle has sufficient energy to dislodge an atom from its normal lattice position, a pair of defects will be generated within the lattice of the material. Similar to an electron-

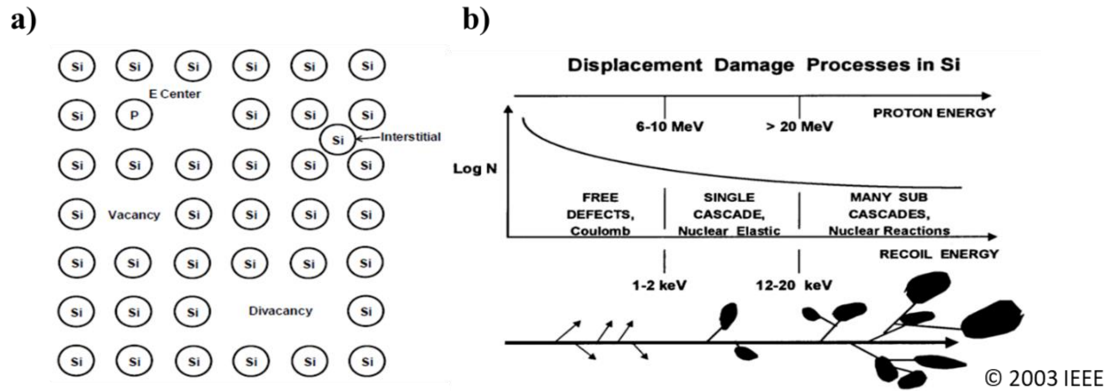

Figure II.9. (a) Illustration of potential isolated defects in Si induced by an incident particle. (b) Representation of the initial defect configuration related to the energy of the primary knock on-atom in Si. After [36].

hole pair, the displaced atom can recombine with the lattice vacancy, thereby repairing the displacement damage, or be spatially separated and form quasi-stable defects. The absence of an atom from a normally occupied location within the lattice is referred to as a vacancy and the presence of a dislodged atom in a non-lattice position is referred to as interstitial. Depending on the amount of energy transferred to the originally displaced atom (primary knock-on atom), the displaced atom can in-turn displace additional atoms, creating a cascade of defects that form localized clusters of disorder (Fig. II.9) [36]. The overall density of generated defects will depend on the energy of the incoming particle. Higher incident energy particles are more likely to transfer sufficient energy to the initial atom to generate cascaded defect clusters.

These radiation-induced defects can result in a variety of defect types that range in stability and impact on material characteristics. The foundation of semiconductor device physics is the band structure resulting from the crystal lattice of a semiconductor material, with any disruption of the periodicity resulting in the introduction of defect energy states in the bandgap. Defect states can lead to device degradation depending on the energy level of the defect state introduced into the bandgap of the material. Defect energy states introduced near mid-gap facilitate generation of carriers by providing an intermediary state for an electron in the valence band to be thermally excited to before subsequent excitement to the conduction band. These energy states can also serve as recombination centers by capturing both an electron and a hole from their respective bands. For defect energy levels introduced near the valence/conduction bands, carriers from the band can be temporarily captured before being returned to the band. No recombination occurs in this case as

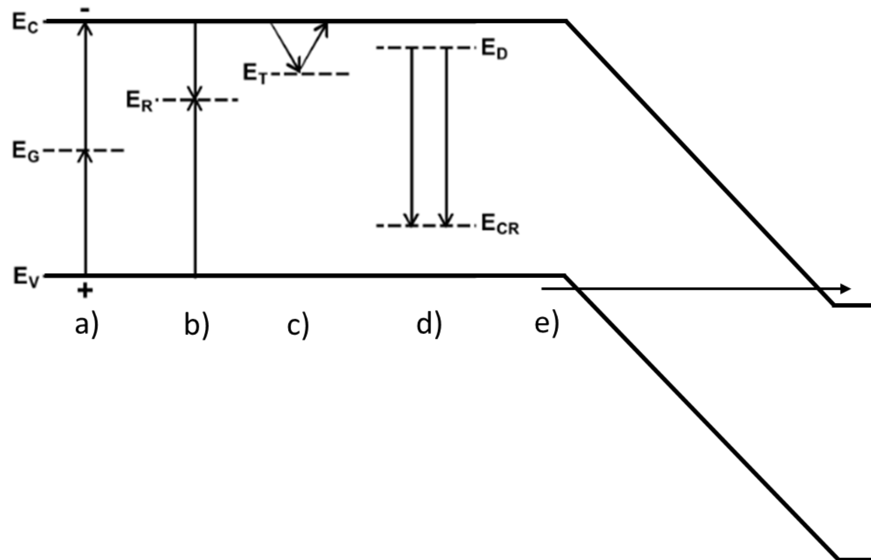

Figure II.10. Depiction of defect energy states and an associated device degradation mechanism: a) defect-assisted thermal generation, b) defect-assisted recombination, c) defect-assisted carrier trapping, d) doping compensation, and e) defect-assisted tunneling. Modified from [37].

the close proximity to a single band implies that the likelihood of capturing a carrier from the other band is minimal. Depending on the doping of the material, defect energies can potentially compensate donor or acceptor atoms, reducing equilibrium carrier concentrations induced by the dopant atoms. Finally, defect levels introduced near potential barriers, such as in a p^+n junction, can assist with carriers tunneling through the junction. These defect energy levels and the associated transitions are depicted in Fig. II.10 [37].

At a device response level, introduction of defects can result in degradation of device performance and, with high enough defect densities, degradation can exceed acceptable operating conditions [36], [37]. Increased thermal generation and junction tunneling results in increased leakage currents (referred to as dark current in some devices) for devices with depletion regions. From a system level, this equates to increased power consumption and a degraded signal-to-noise ratio. Defect-assisted recombination (Shockley-Read-Hall recombination) and charge trapping results in removal of mobile carriers from their bands, reducing transistor gain and output current of detectors. Doping compensation impacts the overall carrier density of a device, impacting parameters that are very sensitive to the doping levels in particular regions, such as the collector in a bipolar transistor or intrinsically doped regions in an PIN diode [38].

CHAPTER III

OPTICS FOR PULSED LASER SINGLE EVENT EFFECTS TESTING AND PHOTONIC DEVICES

As light-matter interaction is at the core of both energy deposition from nonlinear optical processes and the behavior of photonic devices, a brief discussion is pertinent for providing the conceptual framework for the following chapters. Electromagnetic fields are governed by Maxwell's equations, representing light with both phase and amplitude information that can be modified through interactions with materials. The physical mechanisms behind a given optical process is important for understanding how light will be modulated and material parameters are used to quantify this behavior. Overall, this processes of describing light can be used to define optical behavior such as nonlinear optical absorption for energy deposition as well as spatial evolution of light as it propagates through a material [39]–[41].

A. Electromagnetics

Classical electromagnetics considers the behavior of an ensemble of low energy photons as electromagnetic fields that satisfy a set of coupled partial differential equations collectively referred to as Maxwell's equations. At a microscopic scale, Maxwell's equations consider the interaction of discrete charge (volumetric charge density ρ) and the current (current densities, $\boldsymbol{J}$) with electric ($\boldsymbol{E}$) and magnetic flux density fields ($\boldsymbol{B}$).

$$\nabla \times \boldsymbol{E} = -\partial_t \boldsymbol{B} \tag{III.1A}$$

$$\nabla \cdot \boldsymbol{E} = \frac{\rho}{\varepsilon_0} \tag{III.1B}$$

$$\nabla \times \boldsymbol{B} = \mu_0(\varepsilon_0 \partial_t \boldsymbol{E} + \boldsymbol{J}) \tag{III.1C}$$

$$\nabla \cdot \boldsymbol{B} = 0 \tag{III.1D}$$

In a vacuum ($\rho = \boldsymbol{J} = 0$), the electric field can be analytically represented as a homogenous wave equation and consequentially represent the temporal evolution of the electric field as it propagates through space as an exponential function

$$\boldsymbol{E}(r,t) = \boldsymbol{A_\omega} e^{i\boldsymbol{k_0}\cdot\boldsymbol{r} - i\omega t} \tag{III.2}$$

where $\boldsymbol{A_\omega}$ is the amplitude, ω is the angular frequency of the wave, and k_0 is the wavevector of the wave. This representation of electromagnetic fields as complex-valued functions serves to emphasize that 1) light is characterized by both amplitude and phase and 2) modification of these quantities impacts the spatial propagation.

Even in the case of an electrically neutral atom, an electric field can locally displace the negatively charged bound electrons from the positively charged nucleus, inducing an electric dipole moment in each atom. The formation of these dipoles is not instantaneous; the electrons must respond to the presence of the electric field. This required response time of the electron to the electric field creates a dependence of the individual dipole moment not only on the instantaneous state of electric field but on the previous electric field behavior as well. While it is theoretically possible to consider a bulk material at the atomic level with the microscopic Maxwell equations, the sheer number of atoms in a material preclude any computationally feasible approach. Rather than considering the electric field of each dipole individually, the total population of dipoles per unit density can be used to compute a polarization density field ($\boldsymbol{P}$) that can be incorporated into Maxwell's equations as a response function

$$\boldsymbol{P}(r,t) = \varepsilon_0 \int_{-\infty}^{t} \int_{-\infty}^{\infty} \boldsymbol{\chi}(r' - r, t' - t) \boldsymbol{E}(r', t') dr' dt' \tag{III.3}$$

where $\boldsymbol{\chi}$ is the electric susceptibility of the material [39]–[41]. Due to the temporal convolution, it is much more common for polarization densities to be represented in the frequency domain where the electric susceptibility is transformed to a complex-valued material parameter.

With the capability to incorporate light-matter interactions into Maxwell equations, the impact of the polarization density on light propagating in material can be modelled as a solution to the inhomogeneous wave equation

$$\nabla^2 \boldsymbol{E} - \mu_0 \varepsilon_0 \partial_{tt} \boldsymbol{E} = \mu_0 \partial_{tt} \boldsymbol{P} \tag{III.4}$$

As this is an inhomogeneous differential equation, the solution will be sum of the inhomogeneous solution (Eqn. III.2) as well as the particular solution defined by the inclusion of the polarization density. In a general sense, the polarization density induced by the electromagnetic field in the material results in a modification of light propagation in a vacuum. As an example, a simplified case of a linear polarization density that is proportional to the electric field can be used with Eqn. III.2 and Eq. III.4 to calculate a new wavevector (k) for light propagating in a material of

$$\left(-k^2 + \frac{\omega^2}{c^2} + \frac{\omega^2}{c^2}\chi\right)\boldsymbol{E}(r,t) = 0 \qquad \text{(III.5)}$$

where $k = k_0\sqrt{1+\chi}$. The most common way to represent linear optical behavior of a material is the complex dielectric function of the material

$$n + i\kappa = \sqrt{1+\chi^{(1)}} \qquad \text{(III.6)}$$

with the real part of the dielectric function referred to as the refractive index (n) and the imaginary part referred to as the extinction coefficient (κ). Based on this representation of material parameters, it can be said the refractive index of a material impacts the accumulation of phase as light propagates within a material while the extinction coefficient impacts the amplitude of the light. In general, an optical process can be incorporated into Maxwell's equation as a polarization density that will effectively modify the complex dielectric function of the material.

B. Absorption

For an individual atom, each electron inhabits a discrete energy state that is defined by the structure of its associated atomic orbital. As additional atoms are brought closer to form molecular bonds, the discrete electron energy state for each orbital coalesce into finely spaced energy states as the Pauli exclusion principle requires that two electrons cannot occupy the same energy state. Taken to the extreme, the electronic band structure of crystalline lattice of atoms is a description of the energy states that electrons can occupy within the lattice, a consequence of the electronic

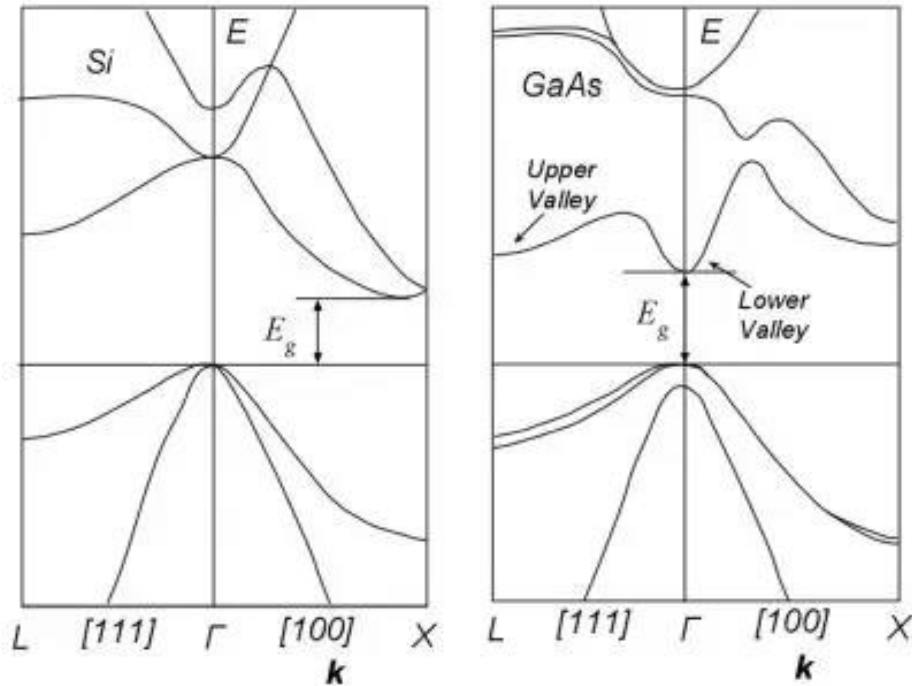

Figure III.1. Band structure of silicon (left) and gallium arsenide (right) depicting an indirect and direct bandgap material, respectively. After [42].

potential induced by the periodicity of atoms within the lattice. In the same way that unique atoms only allow electrons to exist at discrete energy levels, the available energy states for an electron in a crystalline material only exists for bands of energy [42]. Electrons cannot exist at energy states outside these energy bands, with the range of energy separating these allowable bands referred to as the bandgap of the material. Though there are many bands, discussion of band structures typically focus on two bands: the highest energy band with mostly occupied states (valence band) and the next energy band with mostly unoccupied states (conduction band). Semiconductor materials are classified as direct bandgap if the minima of the conduction band and the maxima of the valence band occur at the same momentum value and indirect bandgap if the band extrema do not. Example band structures for silicon (indirect) and gallium arsenide (direct) are provided in Fig. III.1 [42].

Since each energy state corresponds to a specific energy and momentum quantity, an electron can transition between energy states as long as the change in momentum and energy is accounted for by a scattering process. An electron can transition to energy states within the same energy band (intraband) or between energy bands (interband) (Fig. III.2). While interactions with

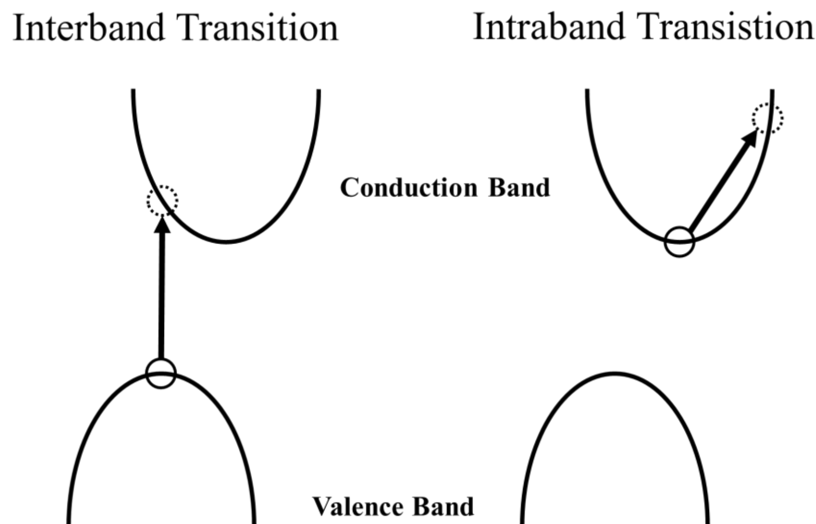

Figure III.2. Simplified depiction of interband transition (left) and intraband transistions (right).

single particles can provide both a source of momentum and energy for an electron, both photons and phonons are crucial to electron transitions as a source of energy and momentum, respectively. A common demonstration of scattering mechanisms is the creation of an electron-hole pair from an interband transition of an electron in direct and indirect bandgap materials. In a direct bandgap material, the conduction band minimum occurs at the same momentum as the valence band maximum, requiring only an energy contribution to transition between bands; this occurrence underpins the dominance of direct bandgap materials as both efficient photon absorbers and emitters. In contrast, indirect bandgap materials exhibit conduction band minima and valence band maxima at different momentum values, requiring both energy and momentum contribution to move between bands. Intraband transitions at the bandgap energy can still occur with phonon-assisted mechanisms (e.g., phonon-assisted absorption, phonon-assisted tunneling, etc.). While it is possible for an electron to transition between the bands using only energy contributions, it will require greater energy than the bandgap.

From the perspective of electron-hole pair generation, an interband electron transition creates a single electron-hole pair, with any photon energy greater than the bandgap of the material "wasted" on promoting the electron to a higher energy state within the same energy band as opposed to creating additional electron-hole pairs. For photon energies on the order of eVs, the electron will thermalize through subsequent scattering processes to the lowest available energy state in the band without generating additional electron-hole pairs (e.g., hot electrons in solar cells).

However, electron transitions associated with X-ray absorption or Coulombic interactions can result in free electrons in the range of keVs. At these energies the electrons have sufficient energy to create secondary electron-hole pairs as they relax to lower energy states, resulting in a single interband transition producing multiple electron-hole pairs. The potential for a single electron transition resulting in multiple electron-hole pairs is typically captured by empirically measured electron-hole pair creation energy E_{ehp} that is used to convert energy deposition to electron hole pairs for high energy radiation sources. A table of bandgaps and electron-hole pair creation energy for common device materials are provided in Table III.1 [42]–[44]. Note that the bandgap is less than the electron-hole pair creation energy due to the loss of energy to non-generative thermalization processes.

Material	Bandgap	Bandgap Energy [eV]	E_{ehp} [eV]
Silicon	Indirect	1.12	3.6
Germanium	Direct	0.67	2.8
Gallium Arsenide	Direct	1.42	4.2
Gallium Phosphide	Indirect	2.26	6.1

Table III.1 Bandgap energies and electron-hole pair generation energy for a small subset of semiconductor materials [42]–[44].

In a pristine material, the energy states in the valence band are almost entirely occupied while the energy states in the conduction band are largely unoccupied. The lack of unoccupied states in the valence band precludes intraband transition of an electron, effectively establishing a minimum energy investment of the bandgap energy for electron transition. This description translates to the notional model of photon absorption in a material, where photons with energy greater than the bandgap of the material can be absorbed to create an electron-hole pair in the material while photons with energy less than the bandgap pass through the material unabsorbed. Once an electron occupies an energy state in the conduction band, the vast availability of unoccupied energy states for intraband transitions results in the absorption of photons with a range of energies, including photons with energies less than the bandgap of the material (termed free carrier absorption). As the density of electrons in the conduction band increases through processes like interband photon absorption or ionization of dopant atoms, the potential for intraband photon

absorption increases. At sufficiently high electron densities, the materials can be opaque to photons even for sub-bandgap photon energies (i.e., doping-dependent absorption in Fig. III.3 [45]).

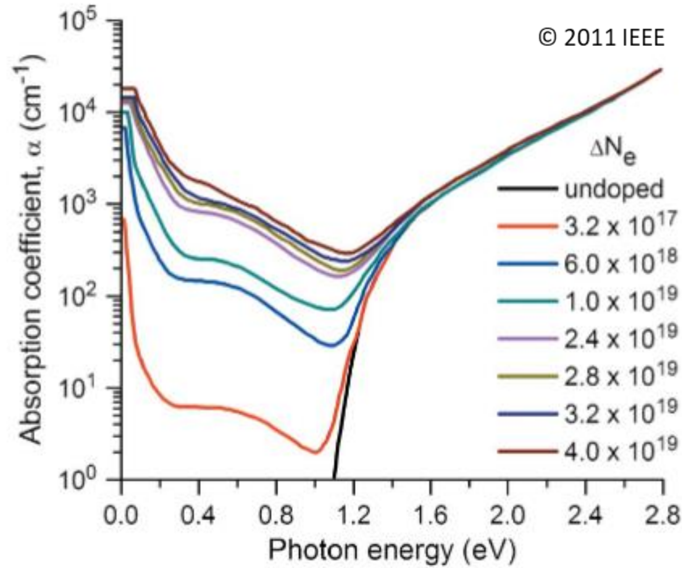

Figure III.3. Absorption spectra of silicon with a variety of doping densities. Note that absorption for the undoped silicon falls off the at the bandgap energy, but doped silicon is absorptive to photons with sub-bandgap energies. After [45].

C. Nonlinear Optics

Rather than a singular term, nonlinear optics expresses the polarization density induced in a material as a power series in the electric field amplitude

$$P(t) = \chi^{(1)}\boldsymbol{E}(\boldsymbol{t}) + \chi^{(2)}\boldsymbol{E}^{2}(\boldsymbol{t}) + \chi^{(3)}\boldsymbol{E}^{3}(\boldsymbol{t}) + \cdots \qquad \text{(III. 7)}$$

with $\boldsymbol{\chi}^{(n)}$ corresponding to higher order optical parameters analogous to the dielectric function in the linear polarization case [41]. Given the high electric field intensity required to the induce the higher-order terms, the higher order optical parameters are quite small and are not accessible in most cases. These higher order polarization density terms give rise to interesting phenomena that are not possible without high fields from focused laser pulses necessary to induced simultaneous photon interactions with the materials.

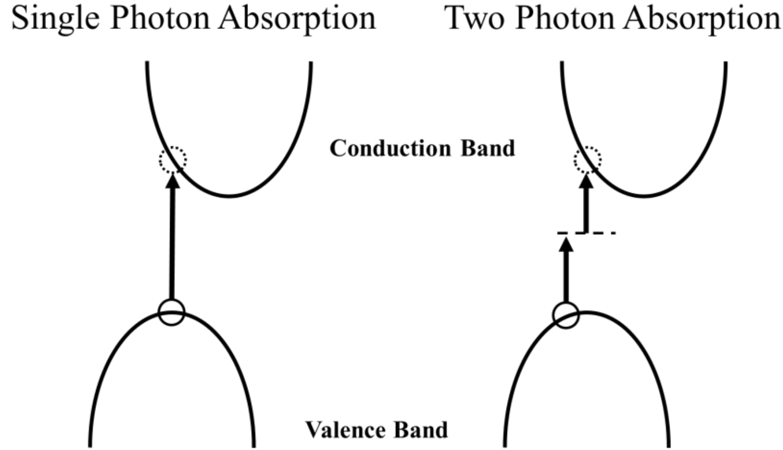

Figure III.4. Simplified depiction of single photon absorption (left) and two photon absorption (right). Note that TPA can occur with photons with energy less than the bandgap.

While nonlinear optical processes find use in a variety of applications, the nonlinear optical processes that are of interest for energy deposition in pulsed laser radiation effects testing are the multiphoton absorptive processes. For single photon absorption, absorption is parameterized with an absorption coefficient (α_0) that is used in conjunction with Beer's law

$$I(z) = I_0 e^{-\alpha_0 z} \tag{III.8}$$

to model the attenuation of light as it propagates in a lossy material. At higher order polarization densities, the simultaneous absorption of photons can result in an interband electron transition with an energy requirement that is the sum of the interacting photons energies. As an example, two photon absorption (TPA) is a third order nonlinearity that describes the absorption of two photons simultaneously. Even in the case the individual photons have subbandgap energies, as long as each photon energy greater than half the bandgap, an interband transition can occur. A notional depiction of this processes is provided in Fig. III.4.

As the nonlinear optical processes are expressed as polarization density terms, they can be considered as modifications of the linear material parameters. In the case of TPA, the total absorption coefficient α of the material can be expressed as

$$\alpha(I) = \alpha_0 + \beta I(t) \tag{III.9}$$

where *I(t)* is the intensity of the electric field and β is the two photon absorption coefficient, a measured material parameter. In a similar fashion, strong electric fields can result in modification of the refractive index of the material in process called the Kerr effect. While these nonlinear processes are largely dormant in many optical fields, the extremely high electric fields induced by high intensity pulsed lasers result in a material response that is largely dominated by the creation of electron-hole pairs through interband transitions and perturbations to the spatial distribution of light as it propagates through the material. A thorough review of nonlinear optical effects can be found in "Nonlinear Optics" by *Boyd* [41].

D. Focused Beam Propagation

As described in Eqn. III.2, an electromagnetic wave propagating in a homogenous, lossless material can be expressed as a solution to the wave equation. Rather than a uniform wavefront, consider the impact of a small modification of the electric field amplitude perpendicular to the propagation direction of the wave

$$\boldsymbol{E}(x, y, z) = A(x, y, z)e^{-ikz}\hat{\boldsymbol{z}} \tag{III.10}$$

where A(x,y,z) is a spatial envelope function that modifies the amplitude of the electromagnetic field as the light propagates in the z-direction. This non-uniform wavefront results in a wavefront that spatially evolves as it propagates, where the spatial profile of the electric field can be calculated by using Eqn. III.4. with the wave equations. Under the slowly varying envelope approximation, an analytic solutions of the A(x,y,z) can be computed (the derivations of this approach can be found in literature [46]).

The culmination of these analytic calculations, referred to as Gaussian optics, is an electric field that notionally describes a focused laser beam

$$\boldsymbol{E}(r, z) = E_0 \frac{w_0}{w(z)} exp\left(\frac{-r^2}{w^2(z)}\right) exp\left(i \left(tan^{-1}\left(\frac{z}{z_r}\right) - \frac{kr^2}{2R} - kz\right)\right)\hat{\boldsymbol{z}} \tag{III.11}$$

$$I(r,z) = |E(r,z)|^2 = I_0 \left(\frac{w_0}{w(z)}\right)^2 exp\left(-\frac{2r^2}{w^2(z)}\right) \quad \text{(III.12)}$$

with the parameters and their physical significance summarized in Fig. III.5 and Table III.2. While not strictly applicable to highly focused laser systems due to the approximations used, the equations still provide physical intuition that is useful for understanding the intensity profile of a laser pulse. Likely the most important observation for pulsed laser-based energy deposition is the relationship between the beam width (radial confinement) and the Rayleigh range (lateral confinement). A distinctive feature of ion tracks is the tight radial confinement over a long lateral distance, which is a configuration that is not possible for focused laser beams using conventional optics due to the fact that increasing the radial confinement of light at the focus of the beam also increases the lateral confinement.

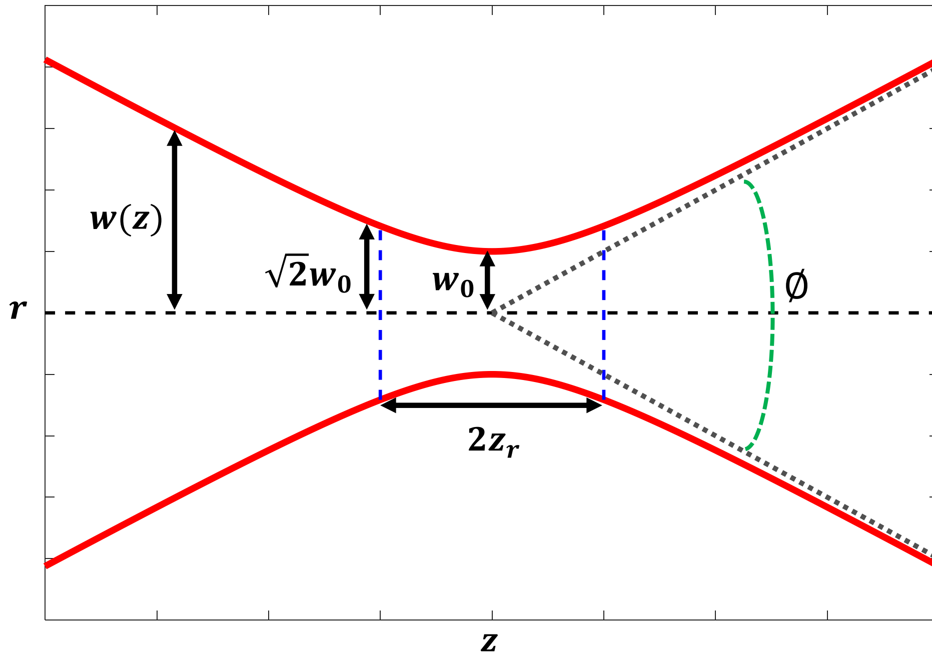

Figure III.5. Intensity contours (Eqn. III.12) for a focused Gaussian beam where the red curves mark the e^{-2} decay from the on-axis intensity. The labeled variables are provided in Table III.2.

Parameter Name	Symbol	Formula	Description based on intensity profile
Beam width	w_0	$\mathbf{w_0}$	Smallest radius of the beam, at the focal point of the beam
Rayleigh range	z_r	$\frac{\mathbf{kw_0^2}}{\mathbf{2}}$	Distance along the central axis to reach half the peak intensity
Beam waist	$w(z)$	$\mathbf{w_0^2\left(1+\frac{z^2}{z_r^2}\right)}$	Radius of the beam at distance z from focal point
Toal angular spread	$\emptyset$	$\frac{\mathbf{2\lambda_0}}{\mathbf{n\pi w_0}}$	Far-field divergence of focused beam

Table III.2. Gaussian optics parameters.

E. Integrated Photonics

The realization of light as a medium for data transmission is motivated by the increased data throughput and reduced energy dissipation achievable by photonic devices compared to electronic devices [47]. Given the tight operational budget for resources in space applications, potential for sizeable reduction in size, weight, and power represents a strong motivator for incorporating integrated photonic devices into space-related systems. To understand the potential degradation mechanisms for integrated photonic devices, it is useful to decompose an active photonic device into its constituent parts.

1) Waveguides

As an analog to the metal traces that shepherd electronic signals, optical waveguides are a broad class of physical structures that serve to route light at the intrachip scale. Total internal reflection (TIR) dictates that under appropriate conditions, light can be confined in a material with a higher refractive index than the surrounding material [48]. Introduction of multiple interfaces that support TIR can be used to further localize the light to the higher index material; the simplest waveguides are comprised of a higher index core material with a lower index cladding material. Waveguides are realized in a variety of geometries and material systems. The material systems available to CMOS compatible silicon photonics rely on silicon or silicon nitride waveguide cores and silicon dioxide cladding [49].

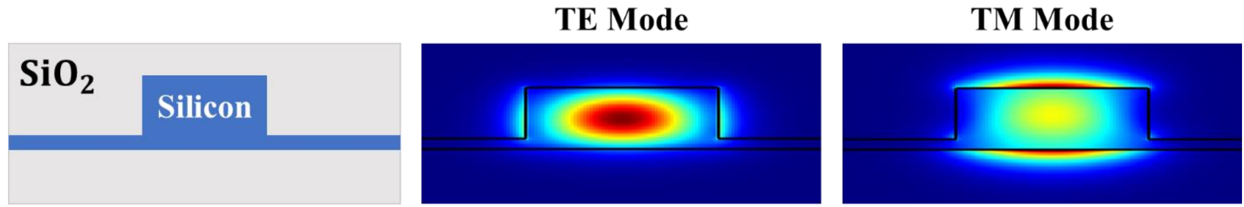

Figure III.6. Electric field intensity spatial distribution in a silicon rib waveguide for the fundamental TE and TM modes. Note that in the case of the TM mode, there is significant electric field located in the cladding material.

Light propagating within a waveguide is not equally distributed within the material, rather it is spatially localized within the waveguide. The distribution of the electric field in a waveguide is called an optical mode. Through the use of numerical techniques to solve Maxwell's equations, a spatial profile of the electric field for an optical mode supported by the defined waveguide can be computed [50]. With the appropriate dimensions and material composition, a waveguide can support multiple modes of both transverse electric (TE) and transverse magnetic (TM) polarizations that can be guided concurrently in waveguide. Using an eigenmode electromagnetic solver, the electric field distribution of the fundamental TE and TM mode for a rib waveguide structure is provided in Fig. III.6.

From the electric field distributions in Fig. III.6, it can be observed that there is electric field in both the waveguide as well as the surrounding cladding material. In an effort to consolidate the complexity of an optical mode for use in other applications, an optical mode is parameterized with an effective refractive index and a confinement factor. Similar to light propagation in a bulk material, an optical mode propagating in a waveguide will accumulate phase proportional to the effective index of the waveguide. A common metric for characterizing an optical mode, referred to as the confinement factor, is the fraction of the electric field intensity in the waveguide core compared to the total electric field intensity.

2) Photon Sources

While it is possible to couple off-chip light sources for on-chip applications to leverage high efficiency technologies, the large coupling loss and complex integration approach naturally point to the integration of the photon sources on-chip as the optimal implementation. To completely integrate photonics and electronic on chip, on-chip photon sources are required provide the

continuous wave light that is used to carry the optical signal encoded by active modulators. In the case of silicon photonics, on-chip sources are required to produce photons near 1310 and 1550 nm (O-band and C-band, respectively) while also supporting conventional lasing behavior through electrical pumping in a small form factor. These sources must achieve this behavior while maintaining high wall-plug efficiency and compatibility with silicon foundry processes [51], [52]. Potential candidate platforms include band-engineered germanium-on-silicon and heterogeneously integrated III-V materials. Due to the complexity of the field, on-chip sources have significantly lagged behind the development of photonic device fabrication and will exhibit radiation susceptibility distinct from that of other integrated photonic components.

3) Interferometric Devices

Creation of an electromagnetic wave from the interference of two other waves can be expressed from a compact modelling perspective as a device with two input ports and one output port. To calculate the output wave from the two interfering input waves, knowledge of the intensity of each input wave and the relative difference in phase between the input waves is required. The intensity of the output wave I_{out} from the interference of two input waves is expressed as

$$I_{out} = I_1 + I_2 + 2\sqrt{I_1 I_2}\,cos(\Delta\emptyset) \quad \text{(III.13)}$$

where I_1, I_2 are the intensities of the input waves and $\Delta\emptyset$ is the difference in phase of the input waves. Based on the functional form of Eqn. III.13 the range of potential intensities of the output wave is determined by the intensity of the two input waves. However, the intensity of the output wave is determined by the difference in phase of the input waves. Providing active modulation over the difference in phase form the basis for optical switches and optical logic devices used in dynamic optical systems.

a) Mach-Zehnder Interferometer

A Mach-Zehnder Interferometer (MZI) is a straightforward interferometric device that relies on constructive and destructive interference to modulate the intensity of the output optical signal. In a symmetric two arm MZI, an incoming optical signal of intensity I_{in} propagating in a

waveguide is split equally into two optical signals. As the electric field is split equally among the two signals, the optical signal propagating along each arm has an intensity of the $\frac{1}{4}I_{in}$ as the optical intensity is proportional to the square of the electric field. At the end of the separate waveguide arms, optical signals in each waveguide arm are interfered together to produce a single optical signal in the output waveguide. The output of the MZI can be modelled by a transfer function

$$\frac{I_{out}}{I_{in}} = \frac{1}{2}(1 + \cos(\Delta\emptyset)) \tag{III.14}$$

where the output intensity of the device is modulated by the difference in accumulated phase ($\Delta\emptyset$) between the two waveguide arms. A simple MZI diagram and output transmission as a function of accumulated phase is provided in Fig. III.7 for reference.

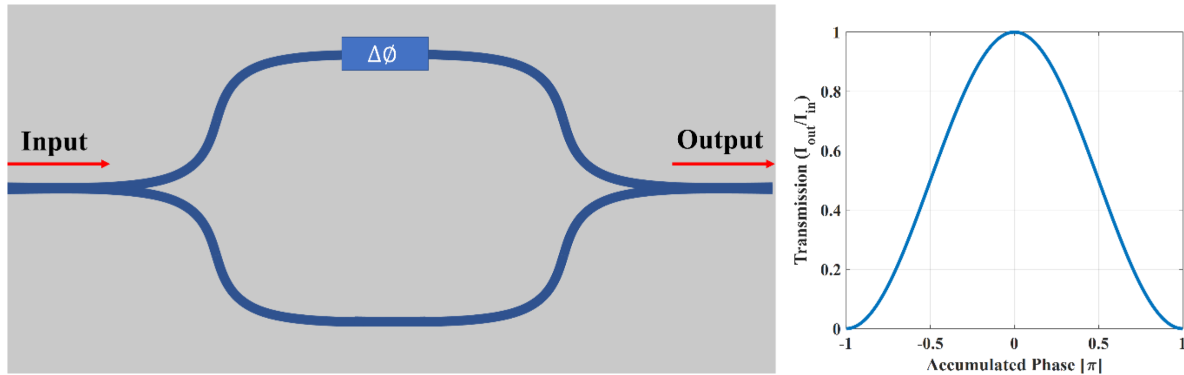

Figure III.7. A schematic of a simple MZI. The transmission of the MZI as a function accumulated phase in one of the arms.

b) Ring Resonator

In a broad sense, a ring resonator is comprised of closed path optical waveguide (ring) and a bus waveguide for coupling light into and out of the ring structure. Light coupled into the ring waveguide will accumulate phase as it propagates along the circumference of the ring and returns to the initial coupling location. As the light completes a round trip around the ring, there is the potential for interference with light that is coupling into the ring. When the accumulated phase of the light from a round trip of the ring is an integer multiple of 2π, the light completing the round

trip will constructively interfere (on resonance) with light entering the ring; any other amount of phase will result is some amount of destructive interference. An example ring resonator geometry is displayed in Fig. III.8; it should be noted that the ring structure need not be circular, just a closed loop.

Under continuous wave operation, a coupled mode approach facilitates the calculation of the transmission intensity [53], [54]. For a critically coupled ring resonator, the transmission (output/input) as a function of accumulated phase $\emptyset$ from a round trip in the ring can be written as a transfer function

$$\frac{I_{out}}{I_{in}} = \frac{2r^2(1 - \cos(\emptyset))}{1 - 2r^2\cos(\emptyset) + r^4} \qquad \text{(III. 15)}$$

where r is the coupling coefficient of a bus waveguide to the ring waveguide. To demonstrate valuable metrics for ring resonators, transmission as a function of accumulate phase is depicted in Fig. III.8. The modulation depth of a resonator, defined as the difference between the maximum and minimum transmission, captures the range in the possible output signal intensities that the device can produce. The full width half maximum of the resonator defines the amount of accumulated phase required to achieve a transmission intensity midway between the maximum and minimum transmissions.

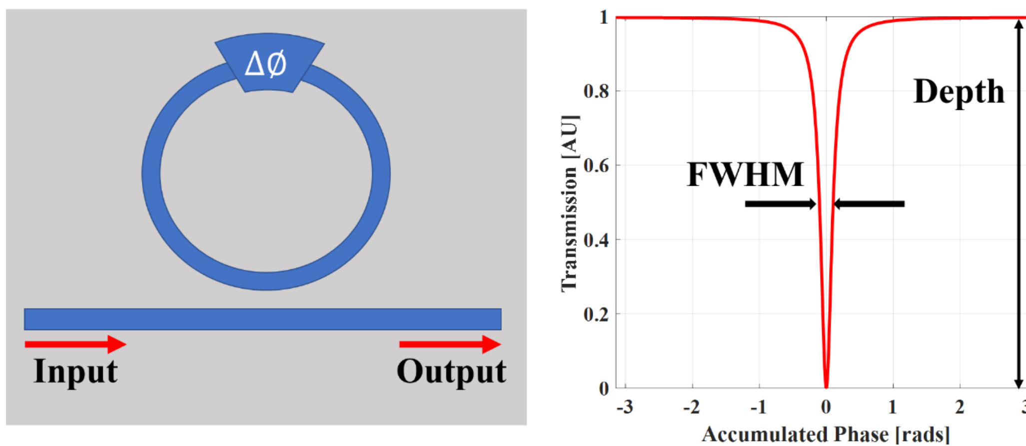

Figure III.8. A schematic of a simple ring resonator with bus waveguide. The transmission of a ring resonator as a function accumulated phase.

4) Modulators

The role of an optical modulator is to manipulate the physical characteristics of an optical signal such as the amplitude, phase, and polarization. To this point, the development of the analytic equations for interferometric photonic devices is centered around the idea of light accumulating phase as it propagates through a waveguide. For a waveguide of the length L, the accumulated phase of the propagating light can be calculated using the effective index of the optical mode. In most cases, the length of the waveguide is fixed post-fabrication, so any control over the accumulated phase in the waveguide must be through modification of the effective index of the waveguide mode.

$$\Delta\emptyset = \frac{2\pi L}{\lambda}\Delta n_{eff} \tag{III.16}$$

While nonlinear optical processes such as the Pockels effect and Kerr effect exhibit strong refractive index modulation capabilities in some materials, silicon is notorious for weak nonlinear optical effects. Therefore, development of optical modulators in silicon photonic devices for active manipulation of an optical signal requires application of alternative techniques for refractive index modulation.

In most cases the transfer function does not exhibit a linear dependence on the phase accumulation, implying an inherent efficiency to modulation based on the region of operation. In the case of the MZM transfer function defined in Eqn. III.14, the first order derivative with respect the phase difference provides a notional modulation efficiency

$$\left|\frac{dT}{d\Delta\emptyset}\right| = \frac{1}{2}\sin(\Delta\emptyset) \tag{III.17}$$

which shows that the peak modulation efficiency occurs at ½π (referred to as the quadrature point). To maximize efficiency and reduce operation voltage requirements, modulators often do not operate in the entire transmission window of the device (0 to 1) but instead operate over a subinterval of the transmission window centered on the quadrature point.

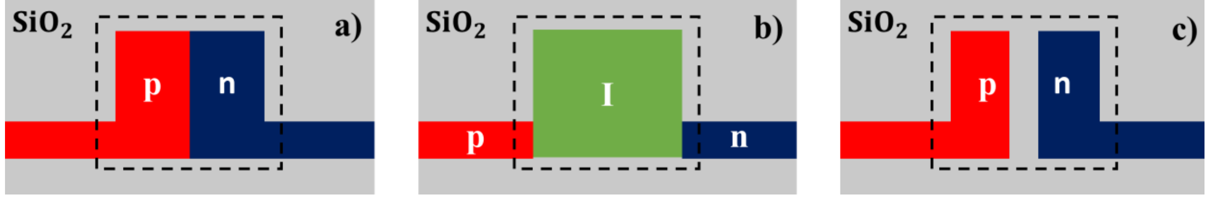

Figure III.9. Schematics for phase shifters using three different carrier modulation techniques. The dashed lines denote the location of the waveguide intersection with the modulator region (a) Carrier depletion through reverse biasing p-n junction. (b) Carrier injection through a forward bias p-i-n junction. (c) Carrier accumulation from a thin oxide region separating a p-doped and n-doped region

a) Electro-Optic

A common technique for providing active control over phase accumulation for light in a waveguide relies on controlling the distribution of free carriers within the waveguide. Free carriers within a material serve to modify the refractive index (n_0) of the base material through free carrier effects such as the plasma dispersion effect (Δn). The complexity of the free carrier effects models varies from material to material. In the case of silicon, the plasma dispersion effect is modeled as

$$\Delta n = -(8.8\ x\ 10^{-22}\ \Delta N_e + 8.5\ x\ 10^{-18}\ \Delta N_h^{0.8}) \left(\frac{\lambda}{1.55}\right)^2 \qquad \text{(III. 18)}$$

where λ is the wavelength of light in microns and ΔN_e, ΔN_h is the change in concentration of free electrons and free holes, respectively [55]. Therefore, controlling the distribution of carriers in a waveguide changes the refractive index for light propagating through the waveguide. Using inspiration from device physics, electronic control over the distribution of carriers in a material can be achieved with carrier depletion [56], [57], injection [58], and accumulation [59] using doped junctions (Fig. III.9).

b) Thermorefractive

Silicon exhibits a relatively large thermo-optic coefficient that has been commonly exploited for providing active modulation [60] as well as fine tuning device performance [61]. The temperature dependence of the refractive index is parametrically described as

$$n(T) = n_0 + \alpha_T(T - T_0) \qquad \text{(III. 19)}$$

where n_0 is the refractive index measured at a reference temperature T_0 and α_T is the thermo-optic coefficient of the material. Strips of metal located near a device form a microheater that heats the surrounding material through resistive heating of the metal. Optically, the inclusion of the metal on a photonic device is problematic as the lossy nature results in attenuation of the optical signal. While thermal modulation might be considered too slow for active modulation in data processing, it is still likely to be used in post-fabrication tuning of photonic devices [61].

5) Radiation Effects in Integrated Photonic Systems

Investigation of radiation effects in silicon photonic integrated circuits relies on the decomposition of integrated photonic systems into sub-components that are more 1) widely available and 2) tractable for tabletop testing. Rather than radiation effects on a complete on-chip optical transceiver-receiver, radiation effects characterization will be conducted on the control electronics, photonic switches, optical sources, and photodetectors separately. Through the use of existing radiation effects knowledge, potential radiation degradation mechanisms can be identified in silicon photonic devices.

Optical transceivers/receivers represent the interconnection of the electronic and optical domains for the purposes of communication (Fig. III.10) [62]. Conversion of a data signal between the electrical and optical domain requires the development of integrated photonic devices that can manipulate light in the same way that electronics control the flow of electrons. Integrated optical sources, such as laser diodes, generate light that can be routed using optical fibers, waveguides, and splitters. Optical switches (photonic device with modulator region) are used to imprint a signal onto the routed light, while photodetectors convert the optical signal into an electronic signal. In typical photonic architectures, electronic devices are integrated alongside photonic devices in order to provide the active control necessary for data processing and transmission, although alternative architectures that rely on light itself to control photonic devices are also possible [62], [63].

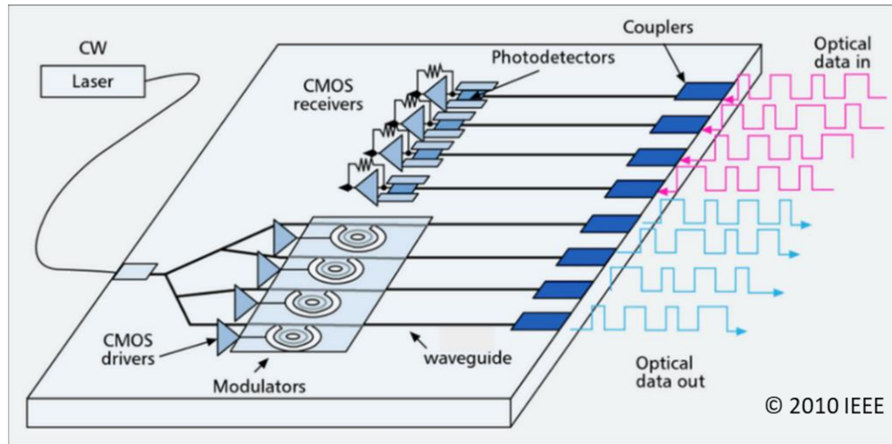

Figure III.10. Schematic representation of an optical transceiver/receiver implementation with different photonic and electronic components necessary to function. After [62].

a) Photonic Devices

Similar to the creation of color centers that increase fiber losses in integrated optics, radiation degradation in passive photonic devices (no electronics) will manifest as modification of the optical properties of materials used in the fabrication of the devices. For example, modification of the refractive index of a waveguide core or cladding material can impact the effective index of a waveguide. This type of degradation has been reported from TID-induced oxide growth on unpassivated silicon ring resonators [64] or through displacement damage in more exotic material systems [65], [66]. However, this type of degradation provides a negligible impact to device operation, requiring the use of ring resonators to achieve enough light-matter interaction to observe a change in the output of the device. In regards to SEEs, simulation efforts have demonstrated that the SEEs can impact an optical signal to a minor extent through injecting free carriers into the waveguide [67]. These observations have led to the growing belief that on-chip passive photonic devices are an inherently radiation tolerate technology.

For active photonic devices, the modulator region presents a distinctly different susceptibility to radiation degradation than the surrounding photonic structure. As the modulator region represents the conversion of an electrical signal to an optical signal, radiation degradation in the electrical behavior of the device can also be observed in the optical output of the device [68]. For example, displacement damage in the depletion region of a junction results in crystal defects that can lead to increased leakage current across the junction [36]. The implication of this increased

leakage current can be interpreted as an increase in power consumption of the modulator (electrical) as well as reduced modulation of the effective index (optical). From an electrical perspective, the radiation degradation of p-n and p-i-n junctions have been extensively investigated [36], [38], [69], [70] and can be used as the basis of radiation effects in modulators. However, the unique junction geometry in tandem with the surrounding oxide has been shown to introduce the potential for degradation of total ionizing dose through introduction of interface traps [57].

b) Drive Electronics

In most cases, the operational voltage for the optical modulator is larger than the voltage used to encode data in the electronic domain of the device and requires amplifier circuitry to boost the data signal to a sufficient voltage. Therefore, radiation degradation that disrupts the ability to accurately amplify a signal voltage represents a significant concern. Given the role of bipolar devices in amplifiers, radiation-induced gain degradation from displacement damage is a potential concern due to reduction in the output voltage of the amplifier [36]. With a reduced output voltage from the amplifier, the capability of the driver circuity to operate the modulator is reduced and results in a smaller output range of the photonic device. In addition to cumulative degradation, the voltage output of the driver can be temporarily disrupted by SETs. While any transistor in the driver circuit can be susceptible to SETs, amplifier circuits are particularly sensitive to SETs on the input transistor as the voltage transient is subject to amplification in the same way as an input voltage signal [71].

c) Waveguide-Integrated Photodetectors

Conversion of an optical signal into an electronic signal is performed through interband absorption that produces electron-hole pairs that are promptly collected by a depleted junction. Since the photodetector needs to absorb light that propagates within the material systems used in the photonic device, a material with a bandgap less than the photon energy of the optical signal is required. In the case of silicon photonics, a common realization of this functionality is a p-i-n structure in the waveguide (similar to a modulator structure) where the intrinsic region is intrinsically doped germanium for electron-hole pair production. Though discrete photodetectors have received radiation testing due to their use in integrated optical systems, waveguide-integrated photodetectors are beginning to receive attention [57], [72]. The intrinsically doped region of the

junction is susceptible to displacement damage that can degrade its collection efficiency as well as increase the leakage current of the junction. Furthermore, as the detector is essentially a reverse-biased junction for collection, SEE sensitivity will be problematic in these devices.

d) Modulator Length

A common technique for characterizing the susceptibility of a device to ionizing particles is the identification of sensitive volumes within a device. For modern electronic devices, the dimensions of these sensitive regions are in the nanometer regime for single devices. In contrast, the length of the conventional modulators is currently on the order of millimeters for MZI applications. Due to the dramatic difference in size scale, there is the potential for photonic modulators to dominate the sensitive area of the device. Fortunately for the SET response of the modulator, the buried oxide layer is reminiscent of silicon-on-insulator electronics which are inherently less susceptible to SEEs; the presence of the buried oxide layer prohibits the collection of charge deposited in the substrate below the oxide.

The collection of deposited charge in the modulator induces a voltage transient on the electrical terminals that competes with the voltage signal driven by the transceiver electronics. Depending on the amplitude of the voltage transient relative to the voltage signal, the impact of the transient can range from negligible to temporary disruption of the signal state. From this perspective, increasing the amplitude of the voltage signal reduces the SET susceptibility of the optical modulator. As the operating voltage and length are implicitly connected through Eqn. III.16, an increased operating voltage necessitates a decreased modulator length to produce the same device output. Therefore, reduction of the length of modulators 1) reduces the SET sensitive device area and 2) requires higher operational voltages which are less susceptible to voltage SETs.

e) Thermal Management

As alluded to previously, silicon exhibits a relatively strong thermo-refractive index that can be considered a double-edged sword for photonic devices. Through the inclusion of microheaters near photonic structures, the local refractive index of the material can be tuned by ohmic heating [61]. While this index modulation could be used for optical switching, the relaxation time for thermal processes is typically considered too slow. Thermal tuning has found much more favor as a mechanism for post-fabrication tuning of devices. Due to the importance of device dimensions

in the operation of a photonic device, fabrication imperfections can significantly impact the output of a fabricated device. Therefore, post-fabrication thermal tuning of individual devices to operate at an intended wavelength has become an attractive process for maximizing performance.

Additional thermal sources, such as power dissipation from neighboring electronics or from the operating environment, can adversely impact photonic devices through the same thermo-refractive modulation. The inclusion of thermal monitoring and control circuitry with photonic devices has been posited as a potential mitigation strategy. Parametric degradation from cumulative radiation damage of electronics tasked with monitoring and dynamically adjusting on-chip temperature can result in inaccurate thermal tuning operation that can significantly disrupt proper device operation. Furthermore, the composition of CMOS-compatible microheaters can have implications in radiation effects if fabricated with high-Z materials, such as tungsten, that can result in secondaries particles which can be problematic for radiation effects [24].

CHAPTER IV

PULSED LASER SINGLE EVENT EFFECTS SIMULATION INFRASTRUCTURE

Traditional ground-based testing for inducing SEEs in microelectronic devices and circuits relies on particle accelerators to accelerate atomic nuclei to energy ranges comparable with particles that could be seen during the course of a mission lifetime. Each accelerator facility provides discrete particle energies dictated by the accelerator design as well as the available "cocktail" of ion species, with most measurement campaigns requiring data collection at multiple particle energies to adequately capture the SEE response of the device. The required particle energy and range in a device drive the selection of testing facilities and can significantly limit the candidate test facilities for most measurement campaigns. Due to the increasing demand for SEE testing of devices, limiting the candidate testing facilities exacerbates the growing scarcity of SEE testing hours at facilities that are meant for interdisciplinary science exploration [73]. The exploration of alternative SEE testing techniques to bolster existing testing infrastructure is critical to not only contribute additional testing hours but also provide testing functionality not available during traditional SEE testing [74]–[76].

PL-SEE testing has become a staple testing technique that leverages tabletop pulsed laser systems for charge injection through photon absorption as opposed to the charge generated by Coulombic interactions from an ionizing particle [76]–[80]. As charge generation is derived from the specifics of the optical pulse, the spatial and temporal control over the laser pulse translates to greater spatial and temporal resolution with PL-SEE testing than traditional heavy ion facilities. Given the cost of tabletop laser systems relative to the particle accelerators used for traditional testing, PL-SEE measurement systems stand to provide more accessible SEE testing infrastructure. These advantages have led to proliferation of PL-SEE facilities and commercial systems.

Production of an electron-hole pair in materials requires sufficient energy to be transferred to an electron such that the electron can be move to an excited state through an interband transition. For photon energies greater than the bandgap of the material, a single photon can be used to create a single electron-hole pair in process commonly referred to as single photon absorption modelled by Beer's Law [39]. While an individual photon with sub-bandgap energies is unable to provide sufficient energy to create an electron-hole pair, nonlinear optical processes can facilitate

electron-hole pair generation with sub-bandgap photons. Multiphoton absorption is a nonlinear optical process that occurs when multiple photons simultaneously interact with a single electron; the total energy of the photons provide enough energy to generate an electron-hole pair. As multiphoton absorption processes require multiple photons, there is dependence on the intensity of the light [41] and charge generation can be localized to regions of high intensity. Using focusing optics, sub-bandgap wavelength laser pulses can be used to deposit charge locally at the focal point of the pulse without depositing charge from single photon absorption [81].

Though PL-SEE measurements have proven invaluable to the radiation effects community as a qualitative technique, a recurring concern is the appropriate strategy for interpreting PL-SEE measurements in regard to heavy ion induced single event transients (SETs). To better address these concerns, interest for developing the technique on a quantitative foundation has been gaining momentum. Though simple correlative techniques between heavy ion and PL-SEE measurements are attractive, the prerequisite heavy ion measurements do not allow for prediction of heavy ion measurements strictly from PL-SEE measurements [82]–[84]. A more general approach to predicting heavy ion results from PL-SEE requires comparison of the three-dimensional distribution of generated charge induced by both a laser pulse and a heavy ion. Though simulation capabilities for ionizing particles are extensively developed and validated by the radiation effects community [85]–[87], equivalent capabilities for pulsed lasers have only recently begun to be developed. To this point, a first-principles simulation approach for PL-SEE measurements from pulse to electrical measurements has been developed at Vanderbilt University and is briefly discussed below [88].

A. Relevant Physics

A common principle used in SEE testing is the decomposition of the entire event into charge generation and subsequent charge collection through drift and diffusion processes. Reviewing the entire pulsed laser measurement at Vanderbilt [88] (Fig. IV.1), the role of individual components can be identified and implemented within the simulation infrastructure. For instance, a majority of the setup is devoted to characterizing and routing an individual laser pulse. From a simulation perspective all this information can be condensed into a pulse, defined by the parameters of the system, and the objective lens used for focusing the pulse onto the device under

test (DUT). Therefore, the optical side of PL-SEE testing can be represented with the geometry of the DUT, complete with material and doping information, and the parameterization of the laser pulse used to deposit charge. Following the charge deposition in the device, charge is collected by junctions in the device and induce currents on the contact of the device that are measured by the electrical measurement systems. From a simulation perspective, these electronic processes are suitably captured using charge transport solvers like technology aided computer design toolkits.

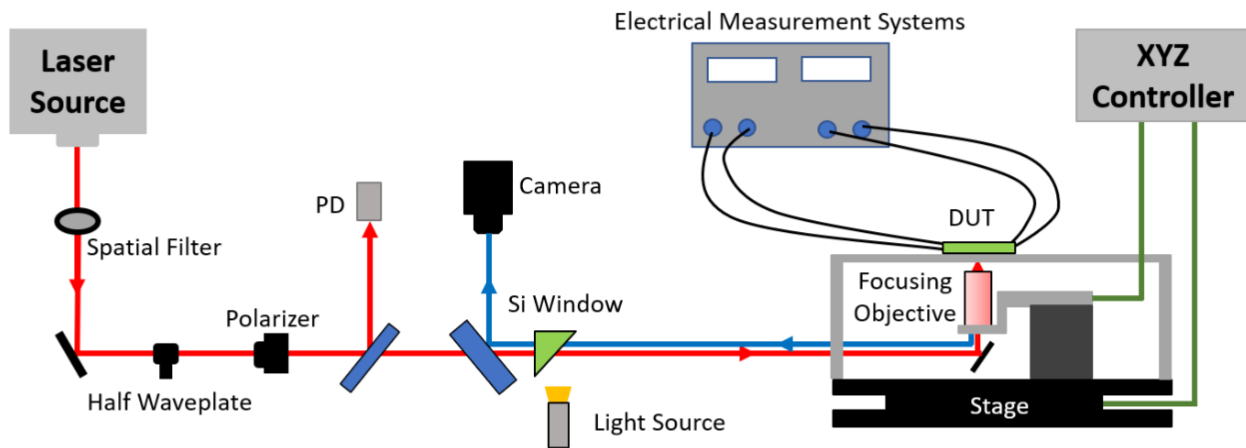

Figure IV.1. Schematic of PL-SEE measurement system at Vanderbilt University. The optical simulations capture all components related to the laser pulse in the system. Charge collection simulators are responsible for electrical components of the measurement setup.

1) Nonlinear Optical Processes

As optical processes are exploited for electron-hole pair generation, accurately capturing light-matter interaction is crucial for modeling the spatial distribution of electron-hole pairs produced from a laser pulse passing through a material. Classical electrodynamics, defined by Maxwell's equations, characterize light with an amplitude and phase; light-matter interaction is captured as modification of the amplitude and/or phase of the light interacting with the material [39], [41]. The capability of materials to modulate light is parametrized as the refractive index and the absorption coefficient. These materials parameters are introduced into Maxwell's equation as linear optical processes. However, nonlinear optical processes can be included into Maxwell's equations by expressing higher order optical processes as intensity-dependent modulation of the linear material parameters [41].

Due to the spatial and temporal confinement of the focused laser pulse used in PL-SEE testing, the optical intensities present during electron-hole pair generation certainly induces nonlinear optical processes near the focal position [89]. The third order nonlinear perturbation of the refractive index and the absorption coefficient is termed the Kerr effect and two photon absorption, respectively. An additional complication introduced during PL-SEE testing is the impact of free carriers on light propagation in the material. High free carrier densities are present in doped semiconductor regions as well as in the region in which charge is being generated via photon absorption. These free carriers can impact both amplitude and phase of light through free carrier absorption and free carrier refraction, respectively [39], [89].

Though there are simplified examples where field distributions can be expressed in analytic terms, most electromagnetics problems require computational techniques to achieve numerical results. The two Maxwell's equations that address wave propagation are the curl equations

$$\boldsymbol{\nabla} \times \boldsymbol{E} = -\mu_0 \partial_t \boldsymbol{H} \tag{IV.1A}$$

$$\boldsymbol{\nabla} \times \boldsymbol{H} = \partial_t \boldsymbol{D} \tag{IV.1B}$$

which, combined with the constitutive equation for the displacement field ($\boldsymbol{D}$), comprise a system of coupled differential equations. Several varieties of algorithms can be used for solving Maxwell's equations; the most natural technique involves expressing electromagnetic fields as coupled quantities that propagate forward in time [90]. Finite Difference Time Domain (FDTD) algorithms rely on difference formulas to discretize both the temporal and spatial derivatives to define update equations that rely on previously defined field components to calculate future field components. As this algorithm solves the Maxwell equations in the time domain, it is amenable to incorporation of additional nonlinear models through the displacement field component. Furthermore, the first-principles nature of this solution technique allows for the simulation of 3D structures of arbitrary complexity without loss of generality.

Lumerical is a commercial, multi-physics software suite that seeks to provide optical modeling of capabilities from light interaction with nanoscale features [91]–[93] to photonic integrated circuits [79], [94]. FDTD Solutions is a material level simulation tool that simulates the electromagnetic response of user defined structures based on the FDTD algorithm [95]. Given the

spatial discretization of the FDTD algorithm, the only limit on device complexity is the resolution of the spatial mesh and the computational resources necessary to run the simulation. While there are other FDTD solver packages [96], [97], FDTD Solutions provides an easy to use GUI as well as additional functionality to improve simulation accuracy, reduce resource consumption, and reduce wall time. Additionally, FDTD Solutions provides the capability for users to define custom physics models for implementation with the solver. This "user plug-in" functionality is what allows FDTD Solutions to be sufficiently modified to incorporate nonlinear models germane to PL-SEE testing.

2) Charge Transport Solvers

Sentaurus is a suite of technology computer-aided design (TCAD) software tools developed for the simulation of semiconductor device behavior[98]. Similar to electromagnetics, charge transport is governed by partial differential equations that can be solved using numerical techniques [99]; these solvers are integral tools for electrical characterization of devices. The spatial distribution of free and bound charge within the material induces an electrostatic potential (φ) distribution that is described by Poisson's equation

$$\nabla \cdot (\varepsilon_s \nabla \varphi) = -q(p - n + N_D^+ - N_A^+) \qquad \text{(IV. 2)}$$

where the charge is contributed from the density of free electrons (n) and holes (p) as well as the density of ionized donor (N_D^+) and acceptor (N_A^+) dopant species. The DC electric permittivity (ε_s) captures the impact of additional screening of the potential from the base material system. The temporal behavior of the density of free carriers is captured through the carrier continuity equations that carrier current density ($\boldsymbol{J_{n,p}}$) flowing as the net contribution of recombination (R_{net}) and generation process G_{net}

$$\boldsymbol{\nabla} \cdot \boldsymbol{J_n} = q(R_{net} + G_{net}) \qquad \text{(IV. 3A)}$$

$$-\boldsymbol{\nabla} \cdot \boldsymbol{J_p} = q(R_{net} + G_{net}) \qquad \text{(IV. 3B)}$$

Physically, the electron-hole pairs produced from a laser pulse are represented as a generation process in the continuity equations. Sentaurus TCAD provides the capability for defining custom generation models, which is used to incorporate the carrier distributions simulated from the optical simulations into charge transport simulations [98].

To completely model a transient captured from a PL-SEE measurement system, it is not only necessary to capture the device response at the device level, but also the circuit response of the measurement system. Even in the case of discrete devices, parasitic contributions from device packaging, cabling, and measurement components can distort the measured transient by increasing the duration and decreasing the peak response. Therefore, accurate emulation of the measurement circuit within the device physics simulations is required to capture the temporal behavior of the PL-SEE transient. Sentaurus TCAD mixed mode simulations allow for the incorporation of the electronic measurement system as lumped-element circuit elements to simulate the system-level response that is the output of a PL-SEE measurement system.

3) Simulation Output

The intent of the simulation infrastructure is to simulate a PL-SEE measurement from the laser pulse to the electrical measurements made on the contact of the device. To facilitate this, the output of an optical simulation is the spatial distribution of charge generated from the laser pulse that can be used as an input for custom models defined in Sentaurus. With the generated carriers input to TCAD, the electrical measurements made on the contact of the device can be simulated and compared to experimental results. From this perspective, two types of outputs can be extracted from PL-SEE simulations: the spatial distribution of optically generated charge and the current transient induced by the pulse. A box diagram of this simulation infrastructure is provided in Fig. IV.2.

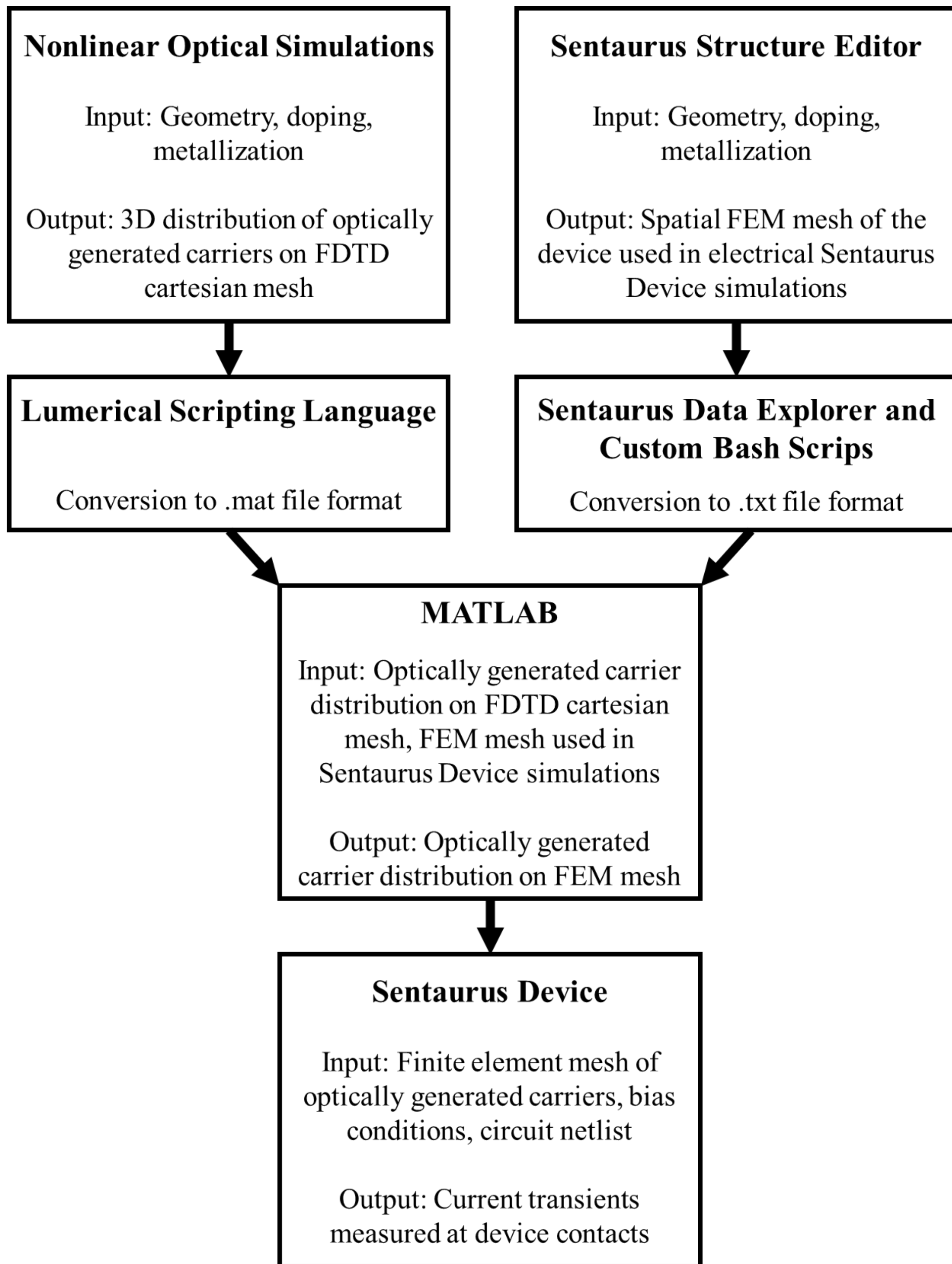

Figure IV.2. Flow chart of the PL-SEE simulation infrastructure discussed in this chapter.

B. Demonstration

1) Test Structure

The test vehicle for this work is a large area epitaxial silicon diode by Beijing Microelectronics Technology Institute, with the schematic representation provide in Fig. IV.3 [100]. To provide access to the active silicon of the device, the topside contact has a periodic inclusion of circular holes with a measured diameter of 14 μm. It should be noted that the areal contribution of the individual holes (~154 μm^2) is negligible compared to the total contact area (2.25 mm^2) and won't impact the electrostatics of the device. The width depletion region (w) of the junction formed by p-doped region and lightly n-doped epitaxial region can be analytically expressed as

$$w = \sqrt{\frac{2\varepsilon_s}{q}\left(\frac{1}{N_A} + \frac{1}{N_D}\right)(V_{bi} - V_a)} \quad \text{(IV.4)}$$

where is ε_s the static permittivity of the material, q is the fundamental charge of an electron, V_{bi} is the built-in potential of the junction, and N_A and N_D are the dopant densities of the p and n regions of the junction respectively [99]. It can be seen from the analytic model that width of the depletion region depends on both the dopant densities used to form the junction as well as the applied bias V_a. In the junction formed from asymmetrically doped regions, the extent that depletion region extends into each region is a function of the dopant density mismatch

$$x_n = w\frac{N_A}{N_A + N_D} \quad \text{(IV.5)}$$

where x_n is the width of the depletion region that protrudes into the n-doped region. In the case of the device used in this work, the lightly doped epitaxial region results in a depletion region that 1) is primarily within the epitaxial region due to the low dopant density relative to the p-region and 2) can expand all the way to the heavily doped substate by applying sufficiently high reverse bias to the junction. Therefore, the contribution of charge collection mechanisms from the depletion

region and from potential modulation in the epitaxial region can be tuned through adjustment of the applied bias during measurements [101].

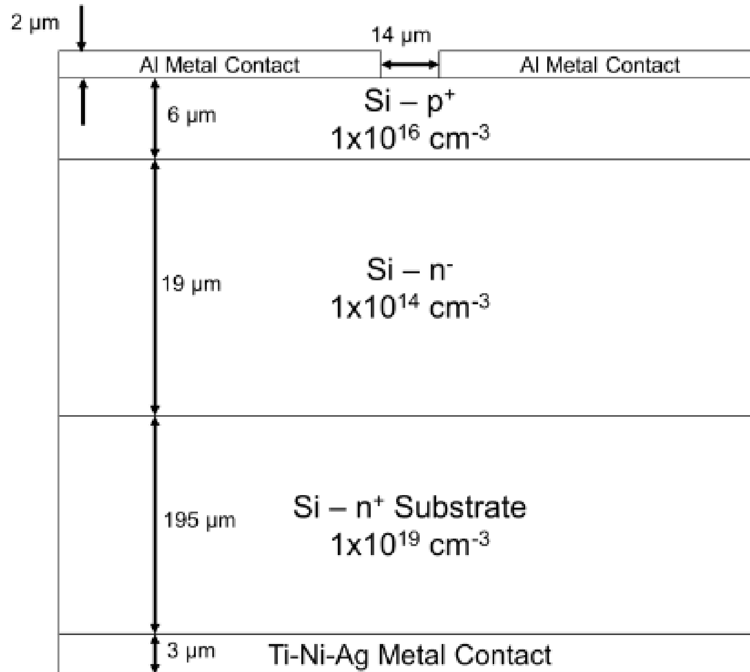

Figure IV.3. The large area epitaxial silicon diode used as test vehicle for comparing the simulation infrastructure with PL-SEE measurements. Note the hole in the topside of the diode allows for topside access for the laser pulse. After [99].

2) Experimental and Simulation Inputs

TPA PL-SEE measurements were conducted at Naval Research Laboratory Ultrafast Laser facility at an operating wavelength of 1260 nm and using an 100x objective. Pre-test dosimetry measurements report laser pulses with temporal full-width at half-maximum (FWHM) of 130 fs and a FWHM spot diameter of 1.36 μm [102]. The diode test vehicle was packaged in a custom fabricated high-speed electronic measurement package, with each terminal connected to a high voltage 12.5 GHz bias tee through SMA connecters. The AC side of the oscilloscope was monitored using a 16 GHz high-speed oscilloscope while a bias is applied to the diode on the DC side of the bias tee. Two voltages were examined during PL-SEE testing: 5 V and 90 V.

For the nonlinear optical simulations, the experimental parameters extracted from the PL-SEE measurement system were used to characterize the laser pulse (pulse duration and

focusing objective) that is used to inject charge in the device and complete device information (materials, doping, metallization) was used to build a 3D model of the device. As the test structure is a silicon diode, the linear and nonlinear optical coefficients can be taken from the literature to define a user-defined material: a refractive index of 3.5 [103], TPA coefficient of 1 cm/GW [104], Kerr coefficient of $4x10^{-18}$ m/W [104], free carrier absorption coefficient of $5x10^{-21}$ m^2 [104], and the free carrier refraction outlined by *Soref and Bennet* [105]. Following incorporation of these system parameters into the optical simulations, 3D spatial distribution of optically generated charge from TPA can be accurately modeled. These spatial distributions of optically generated charge can then be incorporated into TCAD simulations to serve as the initial distribution of charge injected into an equilibrized device. Following this approach, the time-dependent current waveform measured at the device contacts and circuit nodes can be simulated for direct comparison with the transients captured during PL-SEE measurements.

3) Comparison with Experiments

As the objective of the PL-SEE simulation infrastructure is intended to be broadly applicable, ensuring that the experimental data collected for quantitative comparisons span a wide variety of charge transport phenomena. To first-order, the transient response of the device is a consequence of the placement of deposited charge relative the depletion region of the junction as it impacts the proportion of charge collected via drift and diffusion. The most common technique to modulate the charge collection mechanisms within the device is the applied bias that modulates the thickness of the depletion region of the diode. In the case of the PL-SEE testing, charge generated through TPA from focused laser pulses is localized near the focus, giving rise to a common measurement technique in PL-SEE that uses a motorized stage to move the focus through the depth of the device (Fig. IV.4).

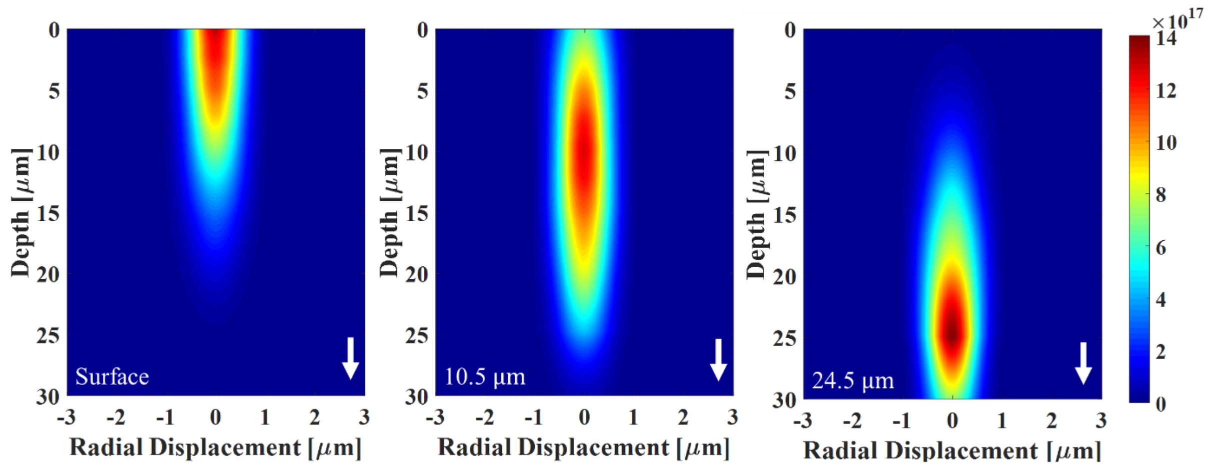

Figure IV.4. Cross-sectional cuts optically generated charge densities that result from a 400 pJ pulse at focal positions: 0 µm (surface), 10.5 µm, and 24.5 µm The arrow indicates the direction of the laser pulse propagation. Note that changing the focal position of laser pulse changes the spatial distribution of charge in the silicon diode.

Depth scan measurements at multiple bias conditions were conducted for multiple pulse energies; individual transients were captured at each test condition for direct comparison. As a demonstration of the output of PL-SEE simulations, a simulated transient is compared with an experimental transient induced by a 990 pJ laser pulse focused at the surface of the diode with a -5 V and -90 V bias is provided in Fig. IV.5. Current waveforms are often reduced down to metrics that characterize the time-integrated response (collected charge) as well as the temporal characteristics of the waveform (e.g. peak height, fall time, etc.). To simplify the comparison with experimental results, collected charge as a function of focal position and bias for 400 pJ and 750 pJ is provided in Fig. IV.6 The excellent agreement across a variety of test conditions legitimizes the approach outlined in this chapter for quantitative PL-SEE simulations.

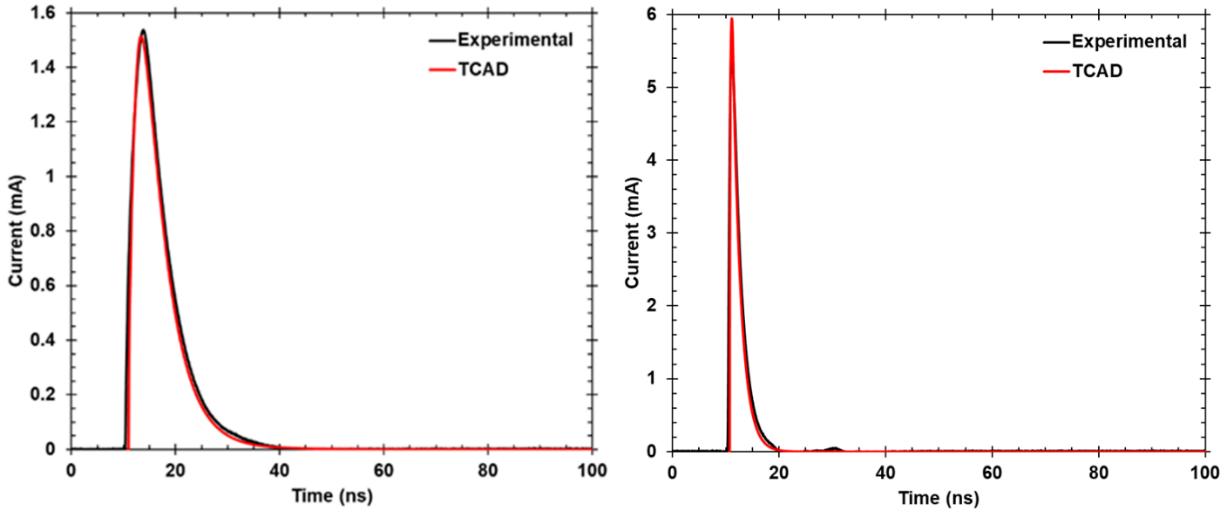

Figure IV.5. Experimental and simulated transients for a 990 pJ focused at the surface of the diode for -5 V (left) and -90 V (right).

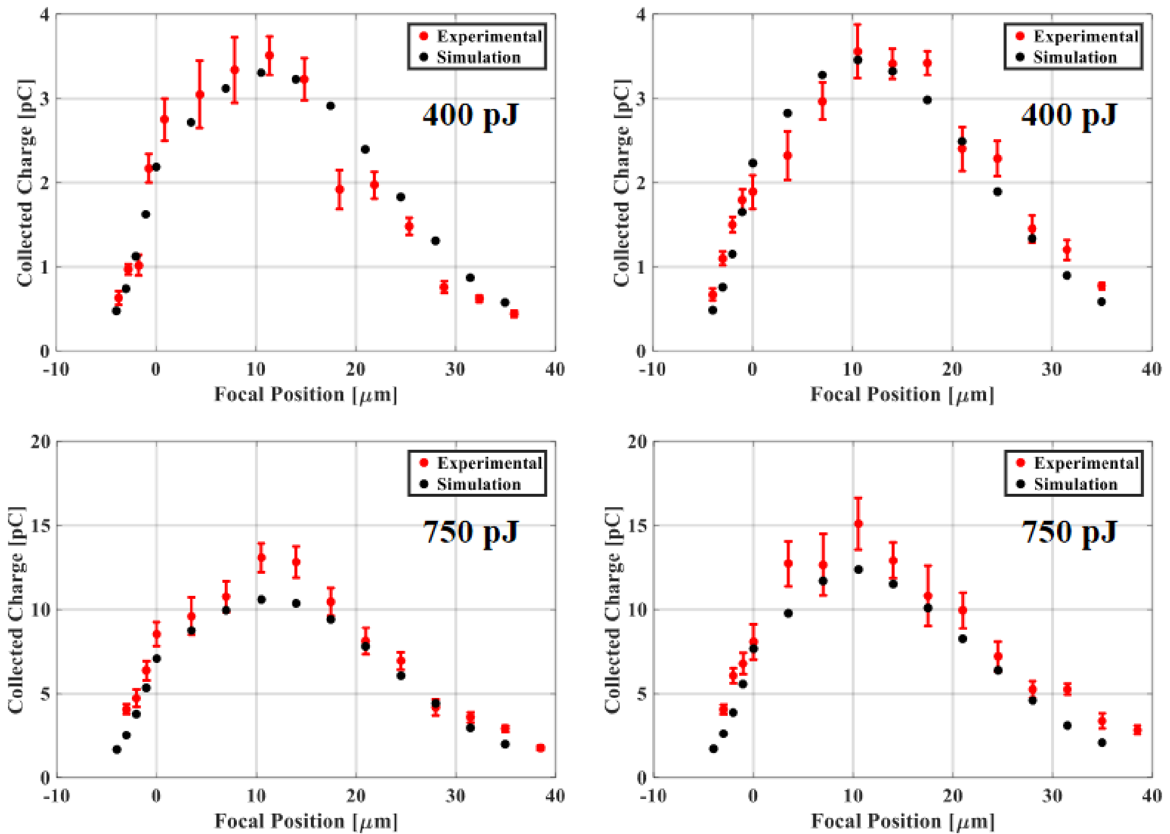

Figure IV.6. Depth scans of the silicon diode for pulse energies of 400 pJ and 750 pJ for two reverse bias conditions: -5 V (left) and -90 V (right). Experimental error bars represent one standard deviation based on 200 collected transients.

C. Other Applications

By design, the nanophotonic simulations and the PL-SEE simulation infrastructure are intended to be generalized tools that can help predict and understand PL-SEE results in a broad sense. The PL-SEE measurements and simulations discussed in the previous sections were intended to demonstrate the qualitative agreement with of the simulation infrastructure with measurements. However, the intended use of this tool is to augment PL-SEE data collection and analysis similar to the that software tools like Monte Carlo simulations [12], [86] and nuclear physics codes [85] are used for ion measurements. To this point, PL-SEE simulations have found use as support tools to investigate physical mechanisms and are briefly outlined below.

1) Correlation of PL-SEE and Heavy Ion Measurements

In addition to the PL-SEE measurements discussed in this chapter, heavy ion and focus X-ray induced transient responses were captured on the large area silicon diode with the intention of probing charge collection mechanisms at play for each SEE measurement technique. A key numerical technique for sampling charge collection processes in SEE testing is the definition of spatial regions within a device that collect charge deposited within the regions. As the spatial distribution of deposited charge is necessary for both the development and application of sensitive volumes, the ability to quantitatively simulate the distribution of carriers with the device is critical. The intention of this work is to leverage both the distribution of generated charge from the laser pulse and the contact measurements from charge transport simulations to create pulsed laser sensitive volumes. It was shown that pulsed laser sensitive volumes differ from heavy ion induced sensitive volumes, showing that even in simple device structures using PL-SEE measurements to predict heavy ion results is more complex than simple correlation [100], [106].

2) PL-SEE Testing of Silicon Power MOSFET

Two photon absorption PL-SEE measurements (481 nm) were conducted on silicon carbide (SiC) power MOSFETs and power junction barrier Schottky diodes to interrogate bias-dependent charge collection involved with single event burnout [107]. Given the structure similarity between the diode and the MOSFET structures, the intent of this work is to use PL-SEE measurements

conducted on both structures to isolate charge collection mechanisms unique to the MOSFET devices. It was observed during the measurement campaign that for the same pulse energy, charge collection is enhanced for focal positions beneath the gate compared to positions beneath the source region of the device. Based on this previous work, this enhancement was suspected to be parasitic bipolar amplification seen in other vertical power devices.

Due to the use of PL-SEE measurements, demonstrating that the enhanced charge collection was not associated with enhanced optical charge generation from interfacial reflections allows for the relegation of the enhancement to a charge collection process. From inspection of the geometry, the device can be simplified to a material stack; the source region becomes a metal/SiC interface and the gate region becomes a metal/polysilicon/SiC interface. For a laser pulse focused at the edge of at the edge of the SiC, a cross section of optically generated carriers was simulated using Lumerical. Due to the highly absorptive nature of the polysilicon, reflections from the metal contact in the gate region of the device is significantly attenuated by the polysilicon layer compared to source region. This observation demonstrates that not only is the enhanced charge collection from the gate region not related to enhanced optical charge generation, less optical charge deposition is expected in the gate region than the source region.

D. Comparison with Existing Methodologies

Given that energy deposition from an ionizing particle is quantitively defined by the linear energy transfer (LET) of the particle in the material, a natural tendency is to define a similar framework for energy deposition from a laser pulse. A simple correlative technique involves the empirical comparison between PL-SEE and heavy ion data on the same device and attempting to map pulse energies to ion LETs based on the device response [83], [84], [108]. Aside from the simplicity, the utility of this technique relies on the ability to use initial ion measurements to "seed" the empirical correlation; PL-SEE testing could then, in principle, emulate any ion LET within the range of the of the correlation. While this technique has found use in the RadFX community, the reliance on both heavy ion and PL-SEE measurements to "calibrate" the technique means that PL-SEE measurements cannot be used as an *a priori* technique for heavy ion measurements. Furthermore, the technique relies on the assumption that differences between energy deposition and charge collection mechanisms for heavy ion and pulsed lasers are negligible. Attempts to

improve the technique have involved incorporation of analytic models based on gaussian optics and modification of the PL-SEE measurement setup to spatially deposit charge more similar to ions [108]–[110].

Simulation tools for calculating energy deposition from ions and secondaries form a cornerstone of SEE testing and mechanism modeling in RadFX community [85]–[87]. Therefore, development of comparable simulation tools for PL-SEE is necessary for building the foundation of PL-SEE testing as a predictive tool. In the same way that nuclear physics codes are necessary simulating ion testing, nonlinear optical physics codes are necessary for representing PL-SEE testing. The first successful implementation of a nonlinear optical solver leveraged the Nonlinear Optical Beam Propagation Method (NLO-BPM) tool created at UCF [111] to calculate carriers deposited in bulk materials [104], [112]. Disciples of this tool have found success in matching simulated results with experimental measurements in some devices, even with the bulk material approximation prohibiting device complexities from being considered in the simulator [83], [108], [109]. However, in the case that material interfaces and asymmetries are prominent in the device geometry, the bulk material approximation is insufficient to capture the relevant optical physics [113].

E. Looking Forward

The family of FDTD algorithms can be very resource intensive due to the discretization of the all three spatial dimensions as well as the temporal steps; numerical stability criteria only serve to exacerbate this by mandating shrinking time steps as the spatial mesh shrinks [90], [114]. Quantitative PL-SEE measurements require 3D simulations that can result in extensive wall time simulations, even on the high-performance computing available at ACCRE. However, expensive quantitative simulations are not always necessary to examine interesting and relevant physical processes. Qualitative simulations can significantly reduce resource consumption through simplifying structures and 2D simulations; less resource consumption per simulation results in more simulations to probe the simulation space (spatial sweeps, energy sweeps, geometric dependence) for the same cost. To maximize the application space and extract the most utility from the simulation infrastructure, a hybrid of both qualitative and quantitative simulations should be used. Given the fundamental difference between near-infrared photons and high energy ionizing

particles depositing charge in a material, this simulation approach is uniquely situated for identifying optical phenomena that impact charge deposition in ways not observed with ionizing particles [113], [115]. Natural candidates for these optical phenomena are small dimensions, material interfaces, and asymmetries [116].

Chapter V

Nanophotonic Effects in PL-SEE Measurements of FinFETs

The following chapter contains materials adapted with permission from L. D. Ryder *et al* "Polarization Dependence of Pulsed Laser-Induced SEEs in SOI FinFETs," *IEEE Trans. Nucl. Sci.*, vol. 67, no. 1, pp. 38–43, Jan. 2020 [113]. This chapter focuses on the PL-SEE measurements conducted on SOI FinFETs that were shown to exhibit dependence on the polarization of the laser light with respect to the device orientation, an effect that was first predicted by the optical simulations described in the previous chapter. Due the small feature size and large asymmetry of the fin, surface plasmons induced at the dielectric/metal interface of the fin result in enhanced optical energy densities to generate carriers within the active silicon of the device. Since the excitation of surface plasmons requires an electric field normal to the interface, the polarization of the light relative to the device orientation dictates how much electric field satisfies this condition, giving rise to the polarization-dependence observed in the measurements. These measurements represent the first time nanophotonic processes have been demonstrated to impact the SEE response of a device, raising specific concerns about the repeatability of PL-SEE measurements of small-scale devices as well as the impact of nanophotonic processes for correlation efforts with heavy ion measurements.

A. Introduction

Though ground-based heavy ion testing is the predominant methodology for single event effects testing, the cost and scarcity of testing hours necessitates alternate testing techniques to augment heavy ion testing [76]. PL-SEE testing has become a popular technique due to the ability to use table top laser systems to inject spatially localized charge into devices through photon absorptive processes in lieu of charge injected by a heavy ion [81]. Due to the tunability of laser energy and wavelength, and 3D control of focal position afforded by a pulsed laser measurement system, the technique has found extensive use within the radiation effects community for applications such as spatial mapping of device sensitivity [117] and examination of charge collection contributions from buried junctions [118]. The spatial control afforded by pulsed-laser

testing has been used to understand geometry-dependent effects in the single-event response of FinFET devices and circuits [116], [119], [120].

In order to create a more quantitative foundation for the pulsed laser-induced SEE testing, it is necessary to consider optical phenomena relevant to the geometry of the device. For some device geometries, it is sufficient to consider light propagating in bulk material [83], [121], but such approximations are insufficient for more complex devices exhibiting asymmetry and complex material systems. As device features become much smaller than the wavelength of the light used for testing, experimental measurements and results need to be reviewed from a more optics-centric approach.

The pulsed laser-induced current transient response of FinFETs as a function of the polarization of the laser pulse is experimentally examined for a sub-bandgap testing wavelength of 1260 nm. Due to the nanoscale feature sizes and metal/dielectric interfaces in the fin region, it is likely that plasmonic effects are responsible for the polarization dependence of the measured transients. A surface plasmon is an electromagnetic surface wave that results from the coupling of electromagnetic fields and collective oscillations of electrons at a metal/dielectric interface [122]. Due to their subwavelength confinement at the metal/dielectric interface and their large field and energy density enhancements, surface plasmons have been exploited with materials commonly found in device fabrication for numerous nanophotonics applications, including nonlinear optics [123], sensing [124], and compact light routing [125]. Plasmonic effects are inherently polarization dependent and therefore provide enhanced energy density and charge deposition for only certain polarization angles of the incident light [122]. A polarization-dependent device response has significant ramifications for the implementation and interpretation of pulsed laser measurements and simulations in highly scaled devices possessing both nanoscale feature sizes and metal/dielectric interfaces. The polarization dependence arises from an optical effect and therefore represents a fundamental difference between energy deposition from optical processes and heavy-ion processes. Hence, modeling of laser testing requires simulation capabilities that capture all optical processes involved in energy deposition. From a practical perspective, during laser testing, device orientation with respect to the incident laser polarization must be consistent across all measurements to ensure that the same pulse energy and laser focal position produce equivalent results.

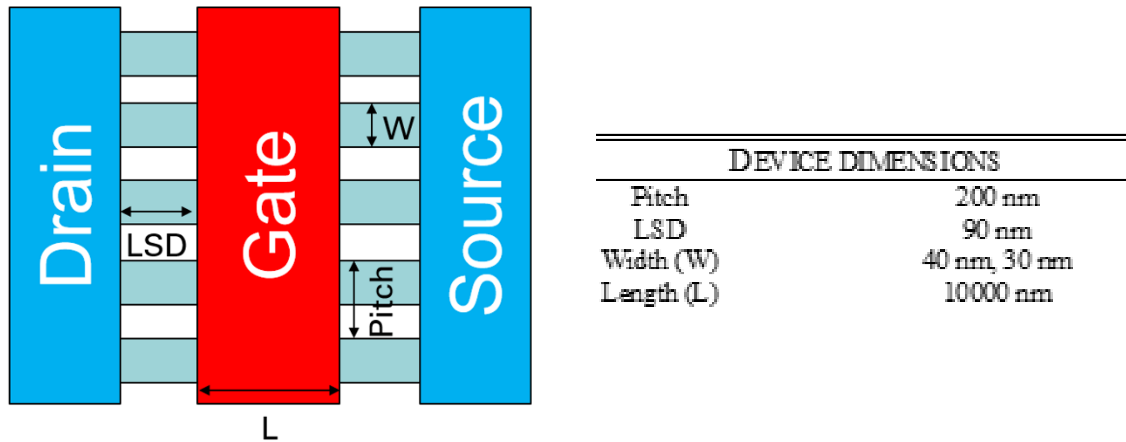

DEVICE DIMENSIONS	
Pitch	200 nm
LSD	90 nm
Width (W)	40 nm, 30 nm
Length (L)	10000 nm

Figure V.1. Topside view of the FinFET device structure under test with associated dimensions. After [112].

B. Experimental Setup

Silicon-on-insulator FinFETs, fabricated by imec, were used as the test structures. Specifically, two 5-fin n-channel FinFETs, of different fin widths, with dumbbell contacts were examined with the top side layout and device dimensions provided in Fig. V.1. The devices feature a high-k gate dielectric (2.3 nm HfO2 on 1 nm interfacial oxide) and 100 nm of polysilicon on top of a 5 nm TiN metal gate. The source/drain access region was formed by Selective Epitaxial Growth (SEG) of Si on the source and drain areas, followed by NiPt silicidation [126]. To allow for charge injection, the backside metallization was removed and the backside polished to provide access to the substrate of the device. A symmetric, large area silicon epitaxial diode was used to provide a control structure, with full device details provided in [106]. Periodic inclusion of circular holes of 14 micrometer diameter (~154 square micrometer area) are included in the top contact to allow for topside illumination of the device without perturbing the electrostatics of the diode.

Pulsed laser measurements were conducted at Vanderbilt University [127]. Through-substrate illumination was used to avoid topside metallization of the FinFETs while topside illumination was used for the silicon diode. A laser wavelength of 1260 nm, with 100x objective to produce an experimental FWHM spot diameter of 1.62 µm (knife-edge), was used to inject charge by two photon absorption in the active silicon region of the devices. Devices were packaged in custom high-speed packages [128], with all terminals connected to 40 GHz bias tees to allow for connection of the AC side of the bias tees to an oscilloscope through high speed cables. A 36 GHz bandwidth, 80 GS/s Teledyne Lecroy Labmaster oscilloscope was used to capture individual

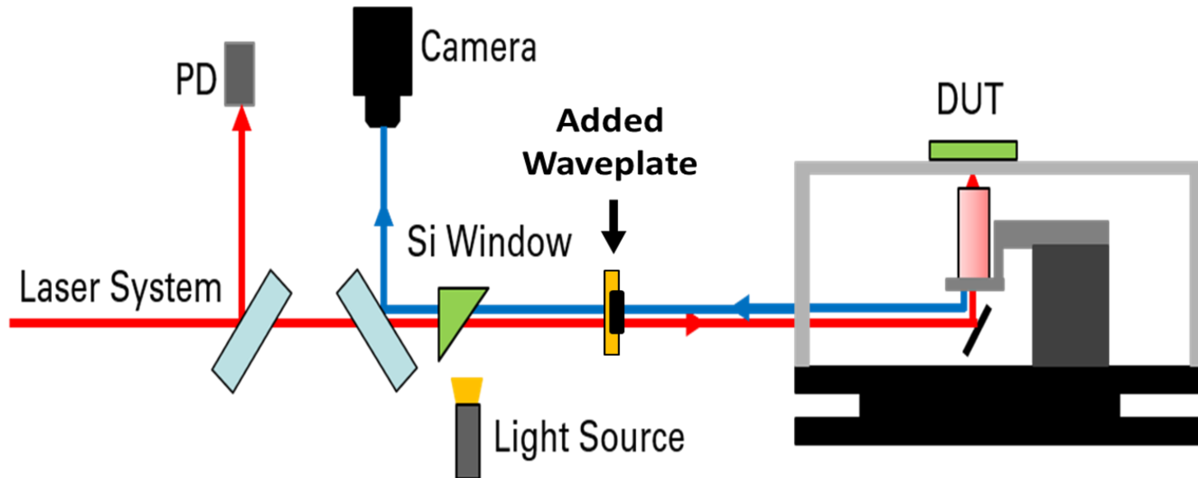

Figure V.2. Modified PL-SEE measurement system used for testing FinFETs. The waveplate is added after any polarization-dependent optical components to ensure that no polarization-dependent losses in the laser pulse were introduced.

current traces. Measurements on the FinFETs were conducted with the gate and source grounded and a safe operation drain-source voltage of 1 V for the 40 nm structure and 0.5 V for the 30 nm structure using Keithley 2410 sourcemeters. The silicon diode was reverse biased to 5 V for the polarization measurements. A half-wave plate was placed between the optical components used in a pulsed laser measurement setup and the device under test (DUT) in order to provide manual polarization control of the pulse incident on the DUT without impacting the performance of the optical components in the measurement setup (Fig. V.2). Once a device package was mounted to the testbench, the complete set of measurements was collected without moving the device package.

C. Measurements

For all measurement campaigns, the contacts of the DUT were monitored to capture individual current transients induced by a single laser pulse. An initial area scan was performed with the waveplate oriented at an arbitrary angle to find the position of the laser on the active region of the device that produced the largest current transients. This laser position was then kept constant for the duration of the device measurement campaign. Due to the 180 degrees periodicity of polarization, the half wave plate was used to rotate the polarization of the initial incident light by up to 360 degrees to produce up to two full rotations of the polarization. It should be noted that

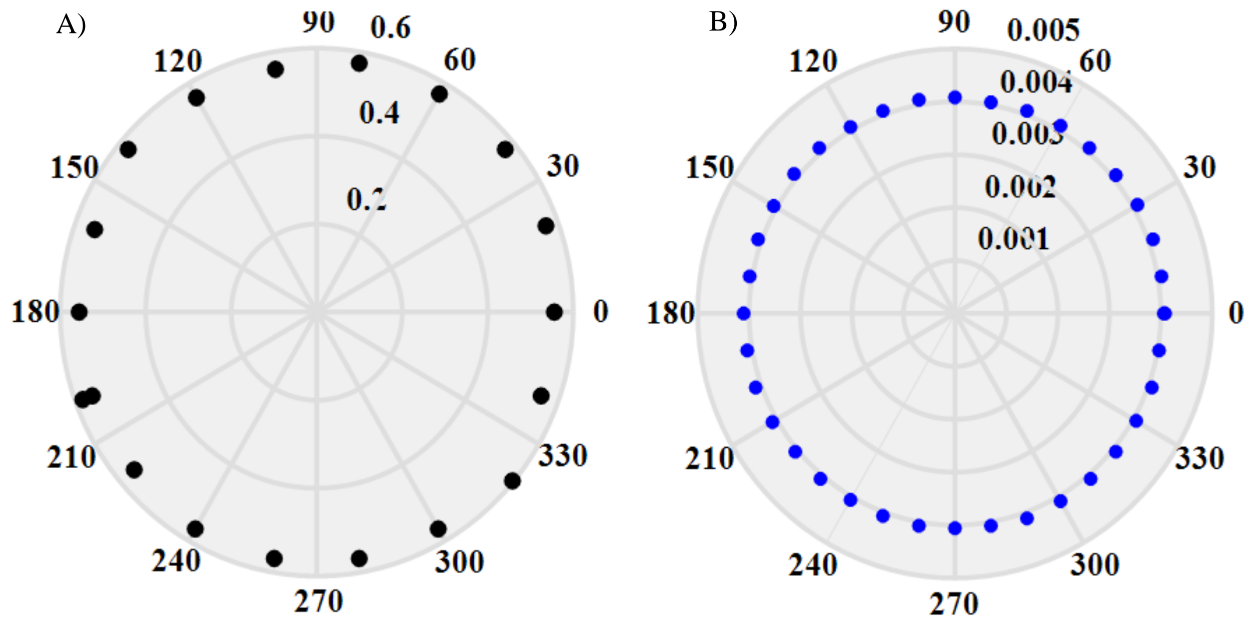

Figure V.3. (A) Voltage response [V] as a function of polarization angle rotation for a power meter placed at the DUT location in the measurement system. Uniform response shows there are no polarization dependent losses in the measurement system. The two measurements at 200 degrees represent the initial and final polarization angle measured. (B) Average peak photodiode response [V] as a function of polarization angle. Photodiode response is used to monitor the energy of individual pulses during measurements. Uniform response shows there is no variation in pulse energy over the course of the measurement. After [112].

the two full rotations of the polarization were performed with a non-repeating range of waveplate angles. Current transients were captured at discrete waveplate angles. In order to verify that rotation of the waveplate does not impact the pulse energy that reaches the DUT through the introduction of polarization dependent losses, an energy probe was placed at the DUT location and monitored as the waveplate angle was rotated. The average pulse energy, as a function of waveplate angle, characterized by the voltage response of the photodiode, is displayed in Fig. V.3A, which demonstrates that the pulse energy at the DUT is independent of polarization.

Every laser pulse that is used to induce a transient is also monitored with a photodiode in order to assign an individual pulse energy to each measured transient. Photodiode response can be used to ensure that a consistent pulse energy is provided by the laser system for the duration of a complete polarization sweep. For each polarization sweep presented in this work, a corresponding photodiode response was captured to ensure that the pulse energy was consistent during the measurements. An example photodiode response for a polarization sweep is displayed in Fig.

V.3B, showing a uniform response consistent with uniform pulse energies during the course of the measurements.

For measurements conducted on FinFETs, the drain contact was monitored to capture current transients. Fig. V.4A and Fig. V.4B display the average peak current of the transients as a function of the rotation of the incident light polarization for fin widths of 40 nm and 30 nm, respectively. For both FinFETs, the average peak current is periodic, with a full cycle occurring over 180 degrees displaying the characteristic lobes of angular dependence. As the two lobes are symmetric, it can be concluded that any periodic error induced by rotation of the waveplate during measurements has minimal impact on the results; the use of non-repeating waveplate angles during the measurement implies that any periodic error associated with the waveplate would be expressed with a periodicity of 360 degrees. A polarization sweep of the silicon diode is shown in Fig. V.5 with the average peak current response of the diode as a function of the rotation of the incident light polarization. The uniformity of the silicon diode response is indicative of polarization independence.

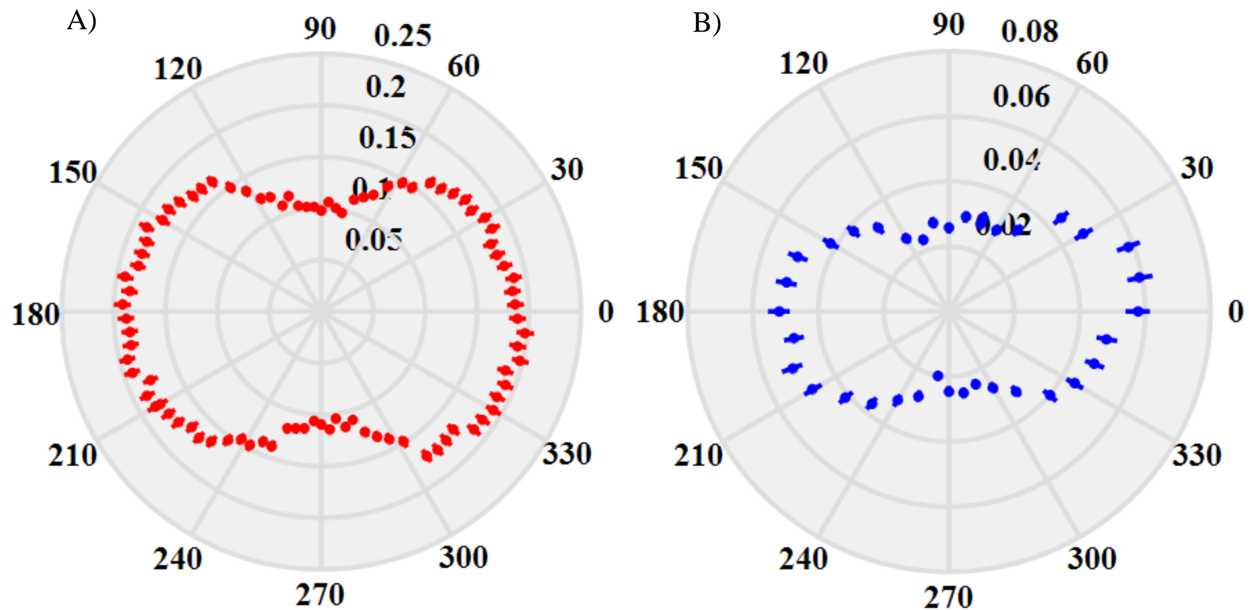

Figure V.4. (A) Average peak current response [mA] of the 40 nm fin width FinFET as a function of polarization angle. Error bars represent one standard deviation of the collected transients. Initial rotation angle is 120 degrees. (B) Average peak current response [mA] of the 30 nm fin width FinFET as a function of polarization angle. Error bars represent one standard deviation of the collected transients. Initial rotation angle is 70 degrees. After [112].

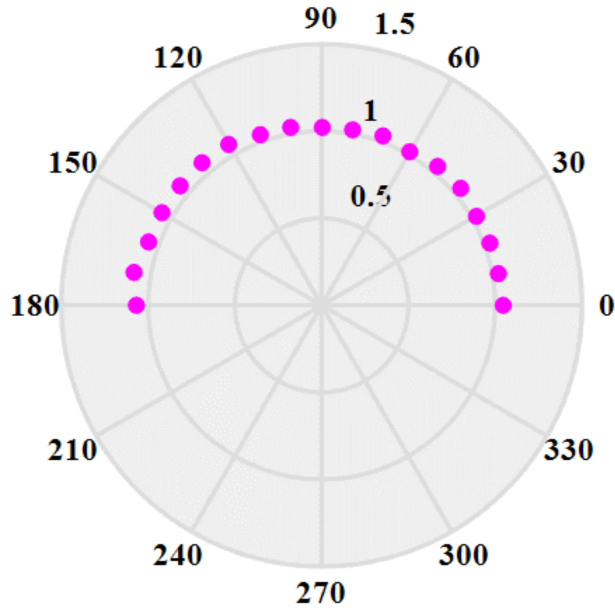

Figure V.5. Average peak current response [mA] of the large area silicon diode as a function of polarization angle. Error bars, representing one standard deviation of the collected transients, fall within the extent of the data point. After [112].

D. Discussion

The polarization of a propagating electromagnetic field defines the direction in which the electric field component is oscillating in a plane orthogonal to the direction of propagation. Two orthogonal directions within the plane of polarization are defined as unique and used as the basis to define any polarization as a combination of the two specified directions. Conversion from one polarization to another is accomplished by rotating the polarization along a central axis. Definition of the polarization of a wave is essential when describing light interaction with materials and interfaces because the direction of the electric field relative to a relevant physical direction impacts the interaction, such as with Fresnel reflection coefficients, birefringent crystals, and in nanostructured materials [129], [130].

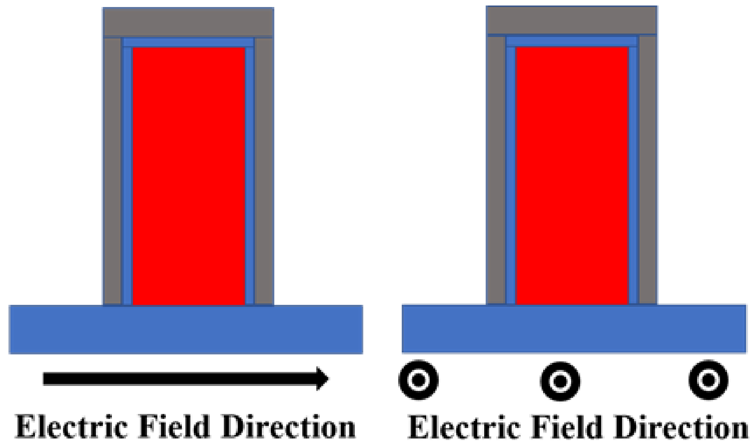

Figure V.6. The two polarization directions in this work are defined by the geometry of the device, as shown with respect to the fin cross-section. Note that the field direction is directed out of the page in the right image. After [112].

In this work, we define the two orthogonal polarization directions relative to the device geometry such that in one case the electric field is polarized along the channel and in the other case the electric field is polarized across the fin (Fig. V.6). To best examine the polarization dependence and ascribe physical significance to the device response, the polarization of light should be considered relative to the device geometry. With knowledge of the device layout on the chip, chip orientation on the test package, package orientation on the test measurement table, and polarization of the laser with respect to the table, the polarization angle relative to the device geometry could be estimated within an error of ten degrees (Fig. V.7). The manual rotation of the waveplate contributes an additional error of approximately two degrees. Accordingly, with a potential error of approximately twelve degrees, Fig. V.4 is plotted with the minima and maxima peak current responses aligned with laser polarization directions along the channel and across the fin, respectively. We note that the initial waveplate angle does not correspond to the waveplate angle that results in the maximum device response for the polarization sweep in either device, which suggests that beam walk-off during the experiment is not occurring. In the case of the 30 nm fin width FinFET shown in Fig. V.4B, the initial waveplate angle was 70 degrees. Since the laser beam position was initially selected to be at a maximum peak current value for this initial

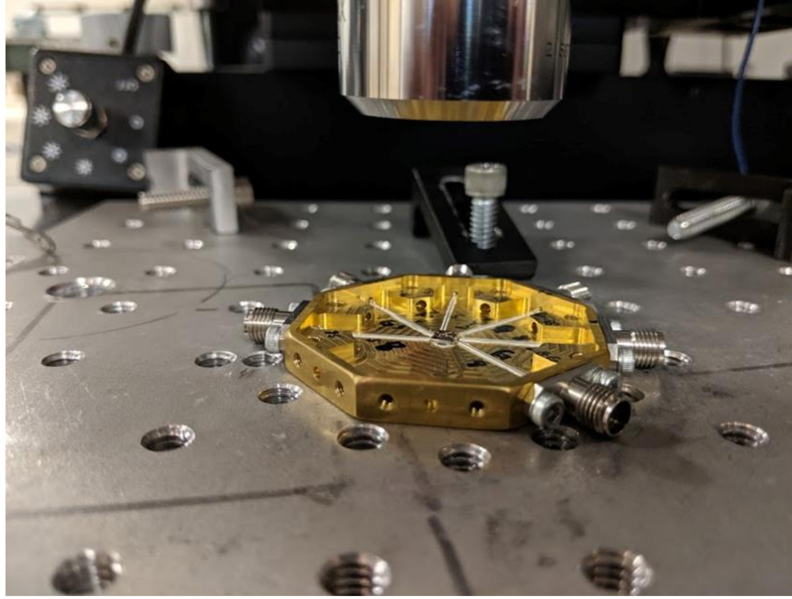

Figure V.7. FinFET device under test in a high-speed packaging used for transient capture. Device orientations were estimated relative to the features on the package itself. These package features were then used to estimate the orientation relative to features on the optical measurement system, where the polarization of the light is known.

waveplate angle, beam walk-off due to rotation of the waveplate would lead to a reduced device response; however, Fig. V.4B shows that the device response increases for some waveplate angles measured after the initial 70 degree position. Furthermore, because the widths of the active regions of the FinFETs are small compared to the laser spot size, the device would remain under constant illumination even in the event of small amounts of beam walk-off.

While the measurements in this work were performed with a stationary device and manually rotated waveplate to minimize the chance of beam walk-off, in a typical laser measurement setup, the polarization of the incident light is fixed and any changes in polarization arise due to rotation of the device, which could be unintentional if the device is moved between measurements. Hence, for devices whose response may be polarization dependent, additional consideration of the device orientation during pulsed laser testing is necessary to ensure results are consistent across measurement campaigns.

E. Mechanism

The polarization independence experimentally observed in the silicon diode suggests that the polarization dependence is connected with the fin region of the FinFET. From the perspective of laser light interacting with a FinFET, the fin can be simply represented as a subwavelength structure with an appropriate dielectric function surrounded by metal/dielectric interfaces. In general, polarization-dependent electric field amplitudes and optical energy densities are known to occur at metal/dielectric interfaces due to surface waves propagating along the interfaces, referred to as surface plasmon polaritons (SPPs) [129]. Due to the confinement of the wave to the metal/dielectric interface, SPPs exhibit large energy densities in the regions close to the interface that may be used to enhance light-matter interaction. Constraints imposed by Maxwell's equations require that SPPs can only be excited at a metal/dielectric interface by (1) light with an electric field polarization orthogonal to the interface and (2) sufficient wavevector matching of the incident light with the SPP [122]. Hence, in general, plasmonic effects could impact both single photon and two photon absorption based puled laser SEE testing. Furthermore, the laser spot size does not impact the ability to excite SPPs, only the spatial extent to which the SPPs are excited. In the fin region of the device under test, the presence of the metal/dielectric interface associated with the gate/insulator/channel provides the potential for excitation of SPPs that contribute to the generation of carriers in the channel due to their increased energy density. While a common technique to satisfy wavevector matching conditions for exciting SPPs requires coupling evanescent light from an adjacent prism, incident light can be directly coupled into SPP modes through end-fire mode coupling to offer direct broadband excitation of SPPs [131], [132]. Rotation of the polarization of the incident light modulates the amount of light that can satisfy the required excitation conditions of SPPs, and therefore modulates the magnitude of the energy density enhancement provided by the SPPs. Optically, the role of SPPs propagating along slits and ridges in a metallic film [133], [134] – test structures that resemble the FinFET [135] – has been well-established and corroborates the polarization dependence of the SPP energy density enhancement.

1) Optical Simulations

Optical simulations can be used to examine the spatial distribution of electron-hole pairs generated by a laser pulse; however, this distribution constitutes the initial state of the injected charge. An experimental device response, such as that presented in Section C, requires consideration of device physics processes to model the transport of charge through the device. The consequence of this distinction is that a quantitative, analytical comparison between optical simulations and experimental device responses is not always practical; rather, direct comparison between optical simulations can be used to examine qualitative characteristics of experimental results. As polarization is a property of the laser pulse used for charge injection, the polarization dependent device response is the consequence of optical charge generation.

To assist in the investigation of physical mechanisms underlying the polarization dependence observed in the pulsed laser measurements of FinFETs, nanophotonic simulations were conducted to elucidate the field distributions as a function of incident polarization. Lumerical FDTD Solutions, a three-dimensional finite-difference time-domain solver that incorporates nanophotonic physical processes through the solution of Maxwell's equations, was utilized for the simulations. SPPs are a direct consequence of applying Maxwell's equations at the interface of a metal and a dielectric, and therefore plasmonic physics are inherently captured by Lumerical FDTD Solutions without any additional considerations [136], [137]. Qualitatively, an individual fin of a FinFET can be simplified to a dielectric fin (channel and gate oxide) on a substrate with a metal gate that encompasses the outside of the fin. Additional device details that are important for modeling electrical properties and device physics can be neglected for optical simulations. The dimensionality of the device can be decomposed into a subwavelength gate width and a gate length that creates an asymmetry between the two directions. As long as this dimensionality is maintained, the impact of gate length is negligible for qualitative simulations. For the optical simulations conducted in this work, a single 40 nm wide silicon fin of height 60 nm and length 1 μm on a silicon substrate was encompassed with metal to approximate a single fin FinFET. The fin was illuminated through the substrate by a laser pulse with a wavelength of 1260 nm for two orthogonal polarization directions: along the fin and across the fin (Fig. V.6).

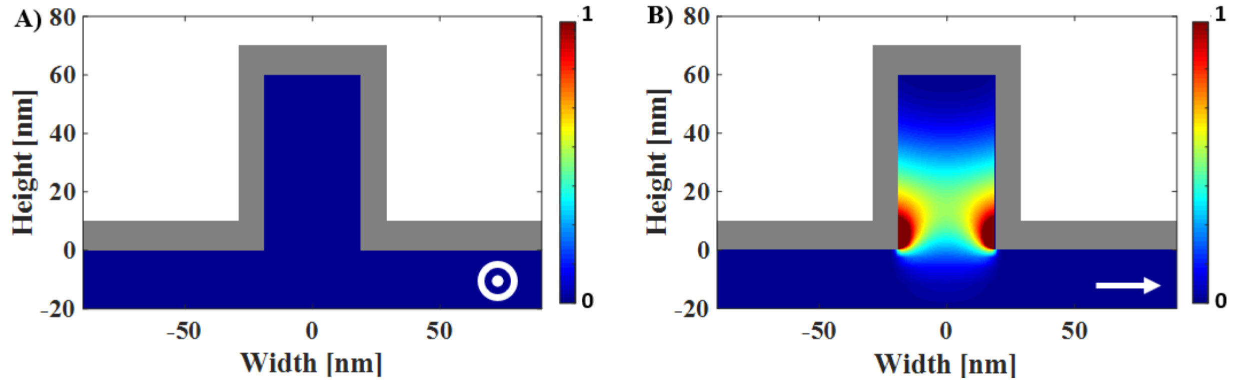

Figure V.8. Normalized cross-section of optical energy density squared induced in a single silicon fin structure from optical simulations to estimate distribution of optically generated charge. White symbols in the lower right corner of each plot indicate the direction of electric field polarization. Color bar scales are equivalent. After [112].

Following completion of the optical simulations, three-dimensional spatial field profiles can be extracted to examine the distribution of fields in the simulated structure. For each polarization direction, a cross sectional cut of the fin structure is taken to examine the optical energy density, as depicted in Fig. V.8. As energy density is proportional to the intensity of the fields, charge generation from two photon absorption is proportional to the square of the energy density and is used to estimate the initial distribution of optical generated charge. Significant enhancement in the energy density is observed in the fin region for polarization directions across the fin (Fig. V.8B) compared to polarization along the fin (Fig. V.8A) The enhancement is largest near the silicon/metal interface at the base of the fin and decreases as the distance from that interface increases. The optical constants of the dielectric material dictate the confinement of SPPs through the decay length of the optical field into the dielectric, with multiple dielectrics near the interface resulting in different decay lengths. Therefore, optical simulations of the device with a complete material system rather than the approximate structure would only serve to perturb the decay of the energy distribution from the interfaces, but would not disrupt the underlying physics.

To further emphasize that the fin structure is capable of supporting SPPs, the fin can be examined with metal-dielectric-metal (MDM) waveguide theory to characterize the plasmonic modes that are supported by the fin structure for comparison with the FDTD simulations. Individual SPPs supported along each side of the fin can potentially interact with each other to form a single plasmonic mode referred to as a gap surface plasmon (GSP) that can be characterized

with an effective index [138]. In the case of the fin structure, SPPs originating at the base of the fin will propagate up the height of the fin before being reflected from the topside metallization. This reflection at the topside will result in the creation of an interference pattern where the spacing in the fringes correspond to the effective index of the GSP mode. In the case of the FinFET structure in this work, the height of the fin is short enough to preclude a resulting interference pattern; simulations of the FinFET structure using a greater fin height reveal the creation of the expected interference patterns (Fig. V.9). The presence of interference fringes in the fin region creates the potential for more height-dependent optical energy deposition than by simply scaling the silicon volume of the device.

Under the appropriate Maxwell's equation boundary conditions for the plasmonic electric fields, a transcendental equation can be defined to compute the effective refractive index (n_{eff}) of the plasmonic mode:

$$\tanh\left(\frac{w}{2}\sqrt{n_{eff}^2 k_0^2 - \varepsilon_d k_0^2}\right) = -\frac{\varepsilon_d}{\varepsilon_m}\frac{\sqrt{n_{eff}^2 k_0^2 - \varepsilon_m k_0^2}}{\sqrt{n_{eff}^2 k_0^2 - \varepsilon_d k_0^2}} \tag{V.1}$$

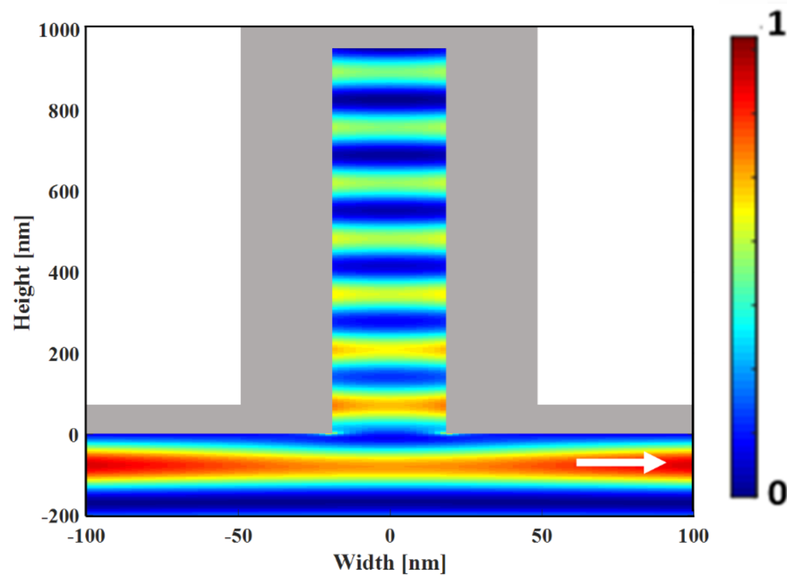

Figure V.9. Normalized cross-section of the electric field intensity induced in a single elongated silicon fin structure. Note the interference fringes associated with reflections from the metallization at the top of the fin. White symbols in the lower right corner of plot indicates the direction of electric field polarization.

where w is the width of the fin region, ε_m is the permittivity of the metal, ε_d is the permittivity of the dielectric material, and k_0 is the free space wavenumber [138]. In the case of the simplified optical structure considered in this work for a testing wavelength of 1260 nm, the permittivity of the silicon fin and the surrounding metal is 12.25 and -153.73+i33.083 respectively [103]. For the two widths of FinFETs used in this work (30 nm and 40 nm), the effective index of the GSP mode can be computed using Eqn. V.1. The effective index of the GSP supported by the fin can be independently calculated using: 1) waveguide theory, 2) interference fringes from 3D-FDTD simulations, and 3) using an eigenmode solver. Lumerical MODE [139], a finite-difference eigenmode solver that computes spatial profiles of electromagnetic fields supported by an optical structure through the solution of Maxwell equations was used to calculate the effective index of the plasmonic mode supported by the fin. The effective index of the GSP modes supported by the fin structure from these methods are provided in Table V.1, showing good agreement between the methods and affirming the potential for the fin region of the device to support GSPs.

Width	Effective Index		
	Waveguide Theory	3D-FDTD	MODE Solutions
30 nm	5.165	5.208	5.16
40 nm	4.81	4.84	4.79

Table V.1. Table of effective refractive index of the GSP optical mode supported by the fin structure computed by independent methods. The agreement between the methods affirms the potenital for SPPs to contribute to optical energy deposition from PL-SEE testing of FinFET devices.

Additional observations related to the optical simulations further support the assertion that SPPs are the dominant physical process in the simulations. Additional simulations carried out on the same single silicon fin, but without the gate metal, did not reveal the same large polarization-dependent enhancement that resulted when the gate metal was present, establishing the role of the metal in the enhancement observed in the simulations. Furthermore, as the simulated structure is a single fin, the polarization dependence observed in optical simulations cannot be associated with any potential optical grating effect established by multiple adjacent fins. In conjunction with the simulation results and plasmonic literature, these observations establish SPPs as a probable

mechanism for the experimentally measured polarization dependence of the pulsed laser induced current transients on the FinFETs examined in this work.

F. Conclusions

Pulsed-laser induced current transients in an SOI FinFET were measured as a function of device orientation relative to the optical polarization of the laser. A dependence in the device response is experimentally observed, demonstrating that device orientation impacts pulsed laser testing measurements. A systematic effect resulting from the measurement setup was ruled out and the geometry and feature size of the device preclude a subwavelength grating-based optical response. Similar polarization measurements conducted on a large area Si diode show no polarization dependence, affirming the role of the small feature size and radial asymmetries of a FinFET in the polarization dependence. Optical simulations were conducted to further examine the impact of incident laser polarization on the optical field distribution within a single fin. A plausible mechanism for the polarization dependent transient current response is proposed based on the polarization dependence of SPPs, which affects the energy density available for charge generation in the fin region.

Based on this work, it can be predicted that this polarization dependence could be observed in nanoscale devices with metal/dielectric/metal interfaces near the active region of the device, such as in multi-gate transistors. Planar devices, due to lack of the metal/dielectric/metal interface and asymmetries, would not be expected to exhibit polarization dependence. Indeed, optical simulations employing bulk materials to model planar devices have shown agreement with experiments, affirming nanoscale optical processes are not dominating charge generation in planar devices. During pulsed laser testing of devices that could exhibit polarization dependence, the device orientation must be considered and documented to ensure robust and repeatable testing of devices that are not rotationally symmetric. Any adjustments of a given device or package between measurements, such as storage for multiday testing, or different orientations of similar devices to be compared, may result in testing under a different polarization configuration and a different measured device response (Fig. V.10). Due to the fundamental difference between energy deposition from light-matter interaction and heavy-ion collisions, such care with device orientation in the measurement setup is not necessary for heavy ion testing. A device that exhibits a

polarization dependence in pulsed laser testing will exhibit that dependence for any configuration of pulsed laser testing using wavelengths larger than the critical feature size of the device.

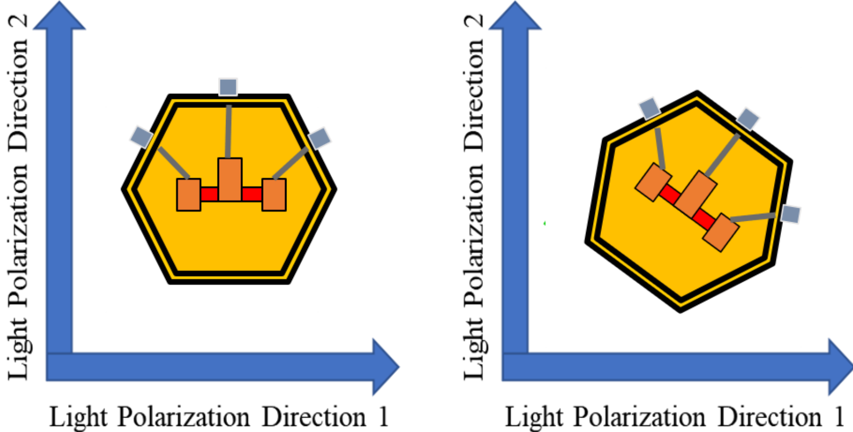

Figure V.10. An visual representation of the impact of package placement relative to the polarization direction of light from the measurement setup.

CHAPTER VI

PULSED LASER SINGLE EVENT EFFECTS TESTING OF WAVEGUIDE-INTEGRATED PHOTODIODES

The following chapter contains materials adapted with permission from L. D. Ryder *et al*, "Single Event Transient Response of Vertical and Lateral Waveguide-Integrated Germanium Photodiodes," *IEEE Trans. Nucl. Sci.*, vol. 68, no. 5, pp. 801–806, 2021 [72]. This chapter focuses on the examination of the PL-SEE measurements conducted on two commonly fabricated waveguide-integrated germanium photodiode geometries that would provide optical-to-electrical signal conversion in an integrated photonic system. Photodiodes typically rely on the high electric field established in the intrinsic region of a PIN junction to ensure that carriers move across the junction at saturation velocity, so the ability for a diode to maintain a high electric field is crucial for consistent operation at maximum bandwidth. Vertical PIN (VPIN) photodiodes typically provide higher electric field amplitude even at lower applied biases due to direct doping of the germanium compared to Lateral PIN (LPIN) photodiodes which are fabricated without direct contact with the germanium. It is shown in this chapter that VPIN devices provide consistent transient durations independent of the operating voltage while LPIN devices exhibit a distinct operating voltage-dependent transient response. This experimentally observed behavior is attributed to the perturbation of the junction electric field and corroborated through simplified TCAD simulations.

A. Introduction

Integrated silicon photonics offer the potential for significant reduction in energy consumption and increased data throughput while leveraging the existing silicon fabrication infrastructure that underpins modern silicon electronics [47], [140]. The production of integrated photonic devices at commercial foundries foreshadows the impending adoption of silicon photonics alongside traditional electronic devices in a variety of commercial applications [141], [142]. The allure of incorporating integrated photonics for improved performance and reduced resource consumption drives the examination of the technology for space-based applications operating with constrained resource budgets. Given the harsh radiation environment, the

investigation of the radiation response of integrated silicon photonic devices is required prior to utilization in space applications. However, to date, there have been relatively few studies evaluating silicon photonic components, including modulators [57],[64], waveguides [65], [67], [143], and photodiodes [57],[144],[145]) for use in radiation environments.

A critical aspect of the integration of silicon photonics with standard electronic devices is the conversion of signals between the optical and electrical domains. Photodiodes are the key component for optical to electrical signal conversion. Due to its compatibility with CMOS manufacturing and large absorption in the telecommunication band of wavelengths, germanium has become the preferred material for on-chip photodiodes. Most commonly, germanium PIN diodes are used to convert optical signals routed in silicon waveguides to electrical signals [146]–[148].

As photodiodes generate electrical signals based on the collection of carriers generated by an incoming optical signal, processes that perturb the collection of the carriers can potentially distort the signal conversion. Cumulative parametric degradation induced by total ionizing dose [57], [144] and displacement damage [145] in waveguide-integrated germanium photodiodes has been examined and the impact on device performance was found to be minimal. Consequently, single event transient (SET) sensitivity will likely be the dominant radiation concern for waveguide-integrated germanium photodiodes, with charge deposited from an ionizing particle interacting with the optical signal [67] or being collected by the photodiode and corrupting the signal integrity if it overwhelms the electronic response of the device.

To examine the SET sensitivity of waveguide-integrated germanium photodiodes, the pulsed-laser induced single event effect (PL-SEE) technique was employed to spatially induce SETs in the sensitive region of the photodiodes. In contrast to standard operation where light is routed from elsewhere on-chip using a waveguide, PL-SEE testing generates charge using highly focused laser pulses that propagate perpendicular to the substrate of the device [149]. In this work, the pulsed-laser induced SET response of waveguide-integrated germanium photodiodes is examined for two geometries: vertical PIN (VPIN) and lateral PIN (LPIN) devices. VPIN devices produce transients with temporal durations that are largely independent of reverse bias while transients collected from LPIN devices increase in duration as reverse bias decreases; these trends hold for a range of pulse energies. As SET duration correlates to the length of time a signal is corrupted, understanding the impact of photodiode geometries on SET response will prove

valuable for the design of integrated silicon photonic systems for use in radiation environments by connecting performance metrics with radiation mitigation concerns.

Photodiode geometries and dimensions significantly impact device performance and can therefore be optimized for a specific performance metric, such as high bandwidth or high conversion efficiency, although a given design sometimes requires a tradeoff between performance metrics. VPIN designs maximize bandwidth by ensuring high fields, enabling carriers to drift at saturation velocity, even at low reverse biases. However, the required structure not only increases fabrication complexity, but also results in high leakage current and low conversion efficiency. The high electric field, coupled with defects due to the lattice mismatch between silicon and germanium, results in leakage paths responsible for increased leakage current [146], [147]. The required doping to facilitate direct contact with germanium results in parasitic absorption of the optical signal from free carriers, which reduces the energy available for electron-hole pair generation and therefore reduces the conversion efficiency of the device. LPIN designs, on the other hand, result in higher conversion efficiency and lower leakage current, but traditionally require higher reverse bias to achieve maximum bandwidth [147], [150]. Importantly, beyond its effect on device performance metrics under typical terrestrial operating conditions, the geometry of the photodiode also dictates the SET response. Understanding the implications of design choices is critical for designing integrated photonic systems that balance system performance with tolerance for radiation degradation.

B. Experimental Setup

Two geometries of waveguide-integrated germanium photodiodes, fabricated by *imec* [148], were used as the test structures for this work. VPIN devices comprise an intrinsic germanium layer with an *n*-doped silicon layer below the germanium and a *p*-doped implantation on top of the germanium. LPIN devices comprise an intrinsic germanium region laterally contacted by doped silicon to form the p-type and n-type contacts. For both geometries, the doped silicon regions are fabricated on a buried oxide. Cross-sections and dimensions for both geometries are provided in Fig. VI.1. A key distinction between the geometries is the lack of metal contacts and doping of the germanium for the LPIN devices compared to the VPIN devices. In the case of either

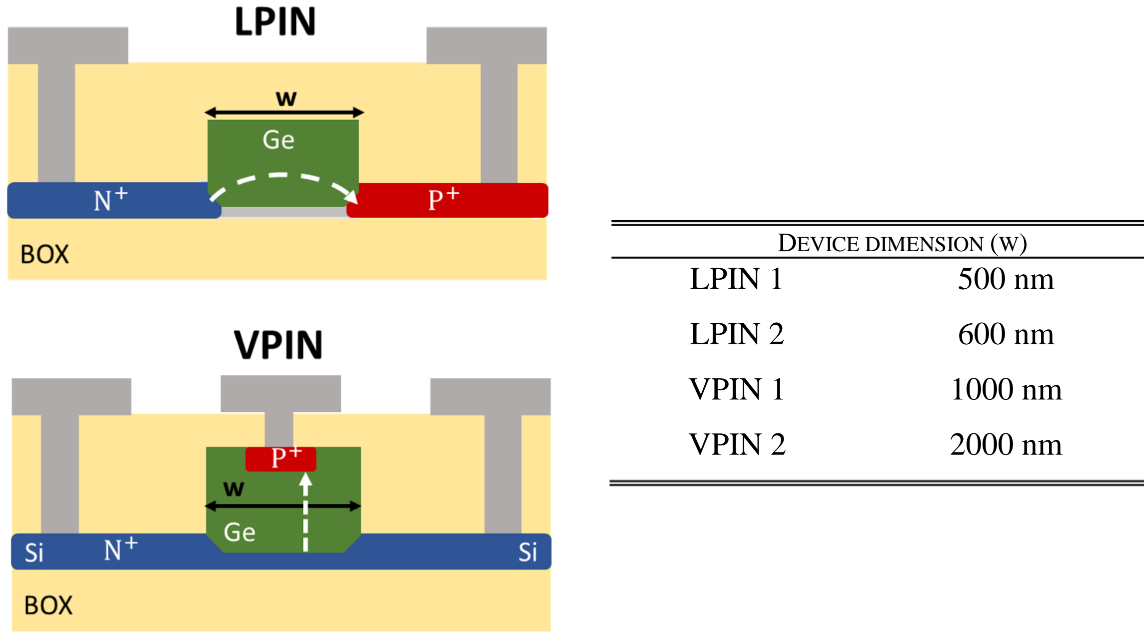

DEVICE DIMENSION (W)	
LPIN 1	500 nm
LPIN 2	600 nm
VPIN 1	1000 nm
VPIN 2	2000 nm

Figure VI.1. Cross-sectional cut of waveguide integrated photodiodes for LPIN, VPIN device geometries considered in this work. In standard operation, the optical signal propagates perpendicular to these cross-sections. White dashed lines denote the direction of the electric field lines in germanium. After [139].

geometry, a PIN diode is created from doped regions contacting the intrinsic region, resulting in an electric field that spans the extent of the germanium region and is used to collect carriers via drift processes. As the PIN diode ensures the presence of an electric field across the intrinsic germanium, an applied reverse bias will primarily modulate the amplitude of the electric field in the germanium and therefore the drift velocity of carriers in the germanium [99].

Measurements were conducted at Vanderbilt University's pulsed-laser testing facility [127]. Devices were packaged on custom high-speed packages, allowing each terminal to be connected to a 40 GHz bias tee that splits the AC response of the device to an oscilloscope using high-speed cables [128]. A 36 GHz bandwidth, 80 GS/s Teledyne Lecroy Labmaster oscilloscope was used to record individual current traces induced by each laser pulse. To avoid the topside metallization of the device, through-substrate illumination was employed using a laser wavelength of 1260 nm to generate charge in the active region of the device with a full-width half maximum (FWHM) beam spot size of 1.6 µm. At a laser wavelength of 1260 nm (0.98 eV), charge generation in silicon is dominated by two photon absorption while charge generation in germanium is dominated by single photon absorption. From the perspective of the device response, charge

generated in the surrounding silicon will be small [109] compared to charge generated in the germanium due to the large single photon absorption coefficient of the germanium [103]. Given the asymmetry of the devices, the orientation of the devices relative to the polarization of the laser was kept consistent to ensure measurements are subjected to the same optical processes [113].

As heavy ions and pulsed-lasers deposit energy through different physical mechanisms, the spatial distribution of deposited energy will be unique to each technique [101], [109]. For the photodiodes tested in this work, the oxide layer below the silicon region of the photodiode truncates the potential charge collection volume and eliminates any contributions to the transient response from the silicon substrate, similar to silicon-on-insulator transistors. Hence, given the small collection depth of the devices, the radial extent rather than the depth profile of deposited energy will be more important to consider when comparing heavy ion and pulsed-laser testing. While the radial extent of the deposited energy from a laser pulse is larger than that from a heavy ion, the prompt transient response from both heavy ions and pulsed-lasers will be dominated by energy deposited in the active region of the device (the intrinsic region in these devices). Accordingly, important insights for understanding the radiation response of germanium photodiodes can be gained from pulsed-laser testing experiments.

C. Measurements

The p-side contact of each device was monitored to capture an individual SET induced by a single laser pulse. Because the energy of each laser pulse used to induce a SET is measured, each SET can be associated with the pulse energy used to create it. The pulse energy reported for the PL-SEE measurements is the pulse energy prior to interaction with a device; attenuation mechanisms such as interfacial reflections [151] are not included in the reported values. For each device, the n-side contact is grounded and a bias is applied to the p-side contact. Measurements were conducted with a null input optical signal state, analogous to an SET occurring during the creation of a low voltage logic state in the electrical domain. An initial area scan was performed to spatially map the device response and identify the center of the germanium channel. Once the position was selected, individual SETs were captured for a range of pulse energies under four bias conditions: -0.5 V, -1.0 V, -1.5 V, and -2.0 V (Fig. VI.2). As PL-SEE testing does not result in total ionizing dose and displacement damage, repeated measurements do not cause permanent

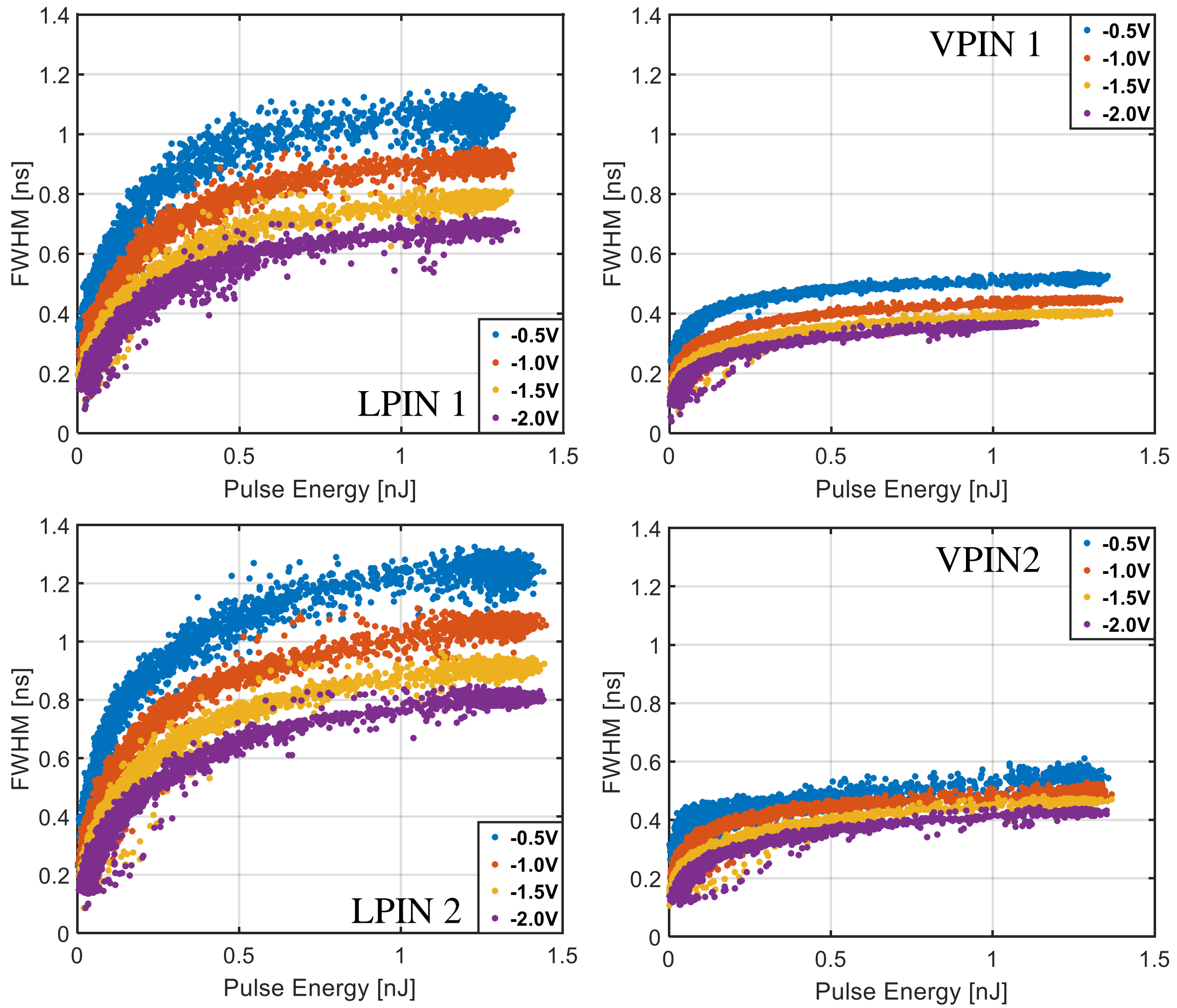

Figure VI.2. Full-width half-maximum (FWHM) of SETs collected as a function of laser pulse energy under four bias conditions: -0.5 V, -1.0 V, -1.5 V, -2.0 V. Device labels correspond to dimensions outlined in Fig. VI.1. After [139].

radiation-induced device degradation [149]. Figure VI.3 compares typical SETs from LPIN and VPIN devices as a function of bias for a fixed pulse energy of 500 pJ. As on-chip data transmission is a key application for integrated photonics, this work examines SET duration because it represents the period of time in which the signal may be corrupted by the ionizing particle. Transients collected from VPIN devices exhibit a consistent temporal duration for each bias condition, while transients collected from LPIN devices display an increasing temporal duration for decreasing reverse bias. The temporal duration of SETs as a function of bias and pulse energy are compiled in Fig. VI.2, demonstrating that VPIN devices display a much more consistent, and shorter, transient duration for all pulse energies and bias conditions compared to LPIN devices.

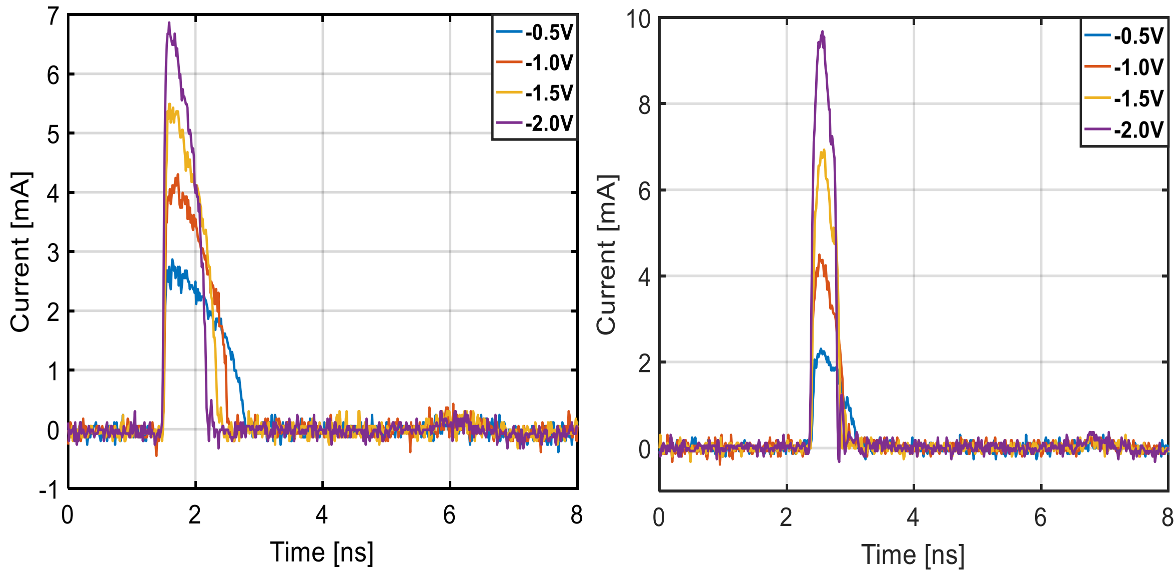

Figure VI.3. SETs as a function of bias for the same laser pulse energy (500 pJ) for LPIN (left) and VPIN (right). After [139].

Carriers contributing to the device response from the overlap of the laser pulse with the doped silicon regions are collected via diffusion processes, implying that those carriers do not result in the voltage-dependent transient response. In addition to comparing the impact of device geometries on SETs, the impact of device dimensions can be examined by comparing device responses for devices of the same geometry. For the same bias (-0.5 V), transient duration as a function of pulse energy is compared for each device measured (Fig. VI.4). While the change in the germanium dimension for the LPIN devices (~15%) impacts the temporal response of the device, the temporal response of the VPIN devices remains consistent when the germanium width doubles.

D. Discussion

The temporal response of a photodiode to an optical signal can be decomposed into four physical processes: carriers drifting across depleted regions, minority carrier diffusion across undepleted regions of a device, the junction capacitance of the photodiode, and the impact of charge trapping at heterojunctions [152]. Under intended electro-optic operation, charge generation in a waveguide-integrated photodiode is localized to the intrinsic germanium layer as the wavelength of the optical signal is sub-bandgap to the surrounding silicon contacts;

contribution to charge collection from diffusion is minimal. Therefore, the dimensionality of the intrinsic germanium region is a design feature that is inextricably linked to the optical performance of a device. For instance, as the intrinsic germanium region is responsible for electron-hole pair generation, a larger collection volume typically results in improved metrics associated with conversion efficiency, such as responsivity and induced photocurrent. However, increasing the dimensionality of the intrinsic germanium also results in performance penalties. Leakage current and junction capacitance increase as the junction area increases; moreover, increasing the transit distance across the junction increases the transit time for carriers crossing the junction [146], [147], [152].

The impact of the design considerations discussed above can also guide understanding of SETs induced during SEE testing. Due to the typical dimensions of the germanium in waveguide-integrated photodiodes, it would be expected that the device response would not be limited by the junction capacitance [153],[154]. As the temporal behavior of the waveguide-integrated photodiodes is dominated by the transit time of carriers, increasing the transit distance results in longer temporal duration of SETs induced in the photodiodes. Therefore, as long as the photodiode temporal response is dominated by the transit distance, junction area has minimal impact on the temporal duration of the SET. For each of the device geometries examined in this work, two intrinsic germanium widths were used in the fabrication of the photodiodes. In the case of the LPIN devices, the width of the intrinsic germanium region inversely affects the magnitude of the electric field and directly corresponds to the transit distance of the junction; therefore, the temporal duration of SETs increases for a larger intrinsic region width at the same bias. For the VPIN devices, the width of the intrinsic germanium constitutes one dimension of the junction area; minimal change in the temporal response occurs for a larger germanium width. Experimentally, this expected behavior for LPIN and VPIN devices of different widths is verified by comparing FWHM as a function of pulse energy for devices with different germanium widths under a -0.5 V bias (Fig. VI.4). Two photon absorption is an intensity-dependent process so that the contribution of charge generated in the silicon would be more pronounced as the pulse energy increases. As the device responses can be related to the width of the intrinsic germanium across the range of pulse energies, it can be concluded that the device response is dominated by charge deposited in the germanium.

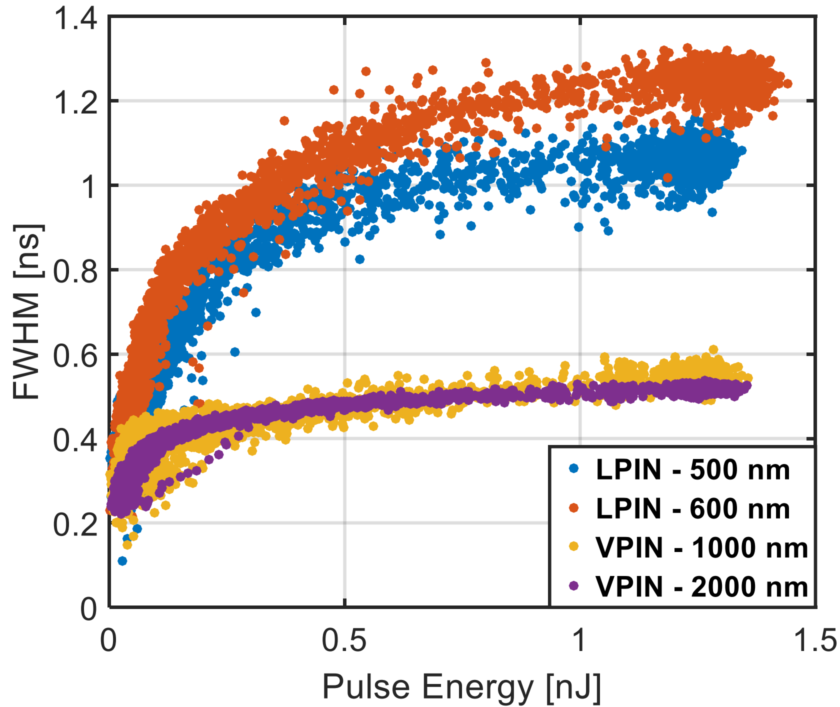

Figure VI.4. FWHM of SETs as a function of pulse energy for all devices under the same bias condition. After [139].

The creation of PIN diodes through the use of the intrinsic germanium in these devices ensures an electric field throughout the germanium, crucial for carrier collection via drift processes. As the drift velocity of carriers is a function of the electric field, establishing sufficiently high electric field amplitudes in the intrinsic germanium region such that carriers move at saturation velocity is often a concern for operation of photodiodes. In most cases, the built-in electric field is not large enough for carriers to drift at saturation and additional bias is required to enhance the electric field in the depleted region of the device [153], [155]. The modification of the spatial distribution of the electric field from the applied bias in turn results in a spatial distribution of drift velocities and transit times for carriers in the junction. As transit time across the junction dominates the temporal response of waveguide-integrated photodiodes, the modulation of the electric field with applied bias constitutes a voltage dependent temporal response of the photodiode. The metal contact with the germanium in the VPIN geometry ensures that the electric field is directed through the intrinsic germanium region, resulting in electric field amplitudes that support saturation velocity even at low biases. As the LPIN devices rely on the doped silicon below

the intrinsic germanium to establish and modulate the electric field in the photodiode (as shown in Fig. VI.1), the amplitude of the electric field is higher near the silicon interface, impacting the drift velocity of carriers [147]. As the reverse bias is increased, the electric field distribution in the intrinsic germanium region results in an increased spatial extent that carriers travel at saturation velocity. Under standard operation, charge generated in the germanium from an absorbed optical signal effectively screens the electric field, impairing the ability for carriers to move at saturation velocity in the germanium and reducing the electrical bandwidth of the device under illumination (referred to as opto-electric bandwidth) [156]. This type of device behavior, related to the electric field distribution and corroborated by charge transport simulations [146],[147],[156],[157], results in LPIN devices exhibiting more pronounced voltage-dependent bandwidths than VPIN devices. The same principles that govern charge collection from an absorbed optical signal are responsible for charge generated by an ionizing particle. Therefore, it would be expected that (1) SET duration will increase as deposited charge increases, and (2) the temporal duration of SETs induced in a VPIN device would be independent of applied bias while the temporal duration of SETs induced in LPIN devices would decrease as a function of applied bias. These hypotheses are validated through experimental data by comparing the FWHM of SETs in VPIN and LPIN devices as a function of voltage (Fig. VI.2). While these measurements were conducted without an input optical signal, these trends will be consistent for measurements with an incident optical signal as is the case for voltage-dependent opto-electric bandwidths under standard operation [156],[158].

1) Device Physics Simulations

TCAD software tools are critical to the design and development of microelectronic devices by modelling the electronic behavior of a device through numerical solutions of Poisson's equation and continuity equations. Given the importance of the electric field strength within the intrinsic germanium to device operation, the capability to capture the electric field distribution within the device from pre- and post-charge injection is crucial to modelling the device response to charge injection. While fabricated devices will have a more complex doping profile and material stack optimized for device performance, TCAD simulations with simplified device geometries still allow for the examination of physical mechanisms. For the TCAD simulation results discussed here, notional dimensions and doping profiles were estimated based upon similar photodetectors VPIN and LPIN structures examined independently in literature [146], [147], [158]. Schematics

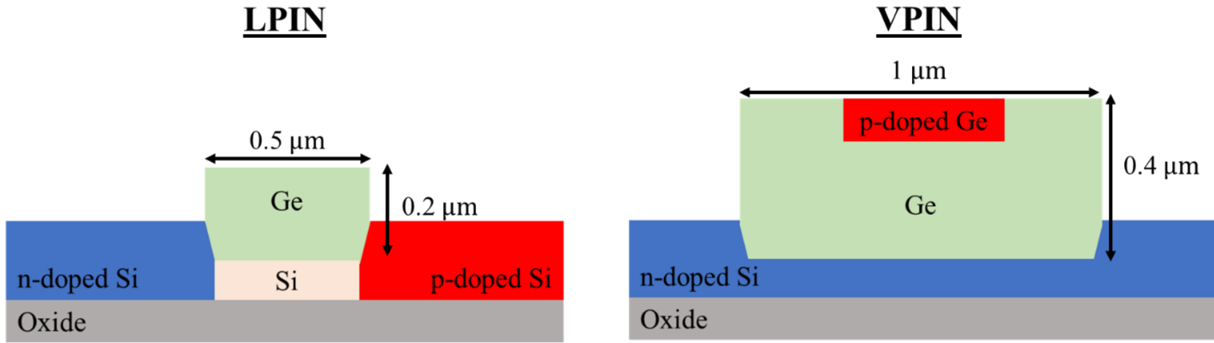

Figure VI.5. A schematic diagram of the simplified LPIN and VPIN photodiodes that were used in transient TCAD simulations. Doped regions used a dopant density of 10^{19} based on similar structures in literature.

of the simplified VPIN and LPIN structures used in the following simulations are provide in Fig. VI.5.

Prior to charge injection, the electric field of a device is in an equilibrium state that is dependent upon the applied bias. For VPIN devices, the placement of the doped regions along the top and bottom side of the intrinsic germanium ensures a strong electric field even at low biases. In contrast, the location of the doped regions in LPIN devices results in the peak electric field amplitude within the intrinsic silicon region and the electric field in the intrinsic germanium penetrating from the silicon below. This notional model of the electric field profile prior to charge injection is confirmed through comparison of the equilibrium electric field at -0.5V and -2.0V, provided in Fig. VI.6. In the LPIN devices, it can be seen that increasing the reverse bias applied to the junction substantially increases the electric field amplitude within the intrinsic germanium region. The voltage-dependent bandwidth associated with VPIN and LPIN photodiodes is a consequence of this electric field modulation.

2D TCAD transient simulations were conducted for a column of charge injected into the intrinsic germanium region analogous to the charge track from an ion passing through a photodetector. Transients were captured for a range of charge injection conditions for four bias conditions: -0.5V, -1.0V, -1.5V, -2.0V (Fig. VI.7). Similar to the PL-SEE measurements, the LPIN device exhibits a pronounced bias-dependent transient duration while the transients observed from the VPIN devices are largely independent of the applied voltage. Furthermore, individual transients can be compared as a function of bias and display the same trends observed in experiments (Fig. VI.8). Since these simulations were conducted with charge injected in the

intrinsic germanium, the potential for contribution from charge generated in the silicon due to the spot size of the laser relative to the device footprint was removed. The simulated results still show the trends observed in the experimental results, demonstrating that this behavior is a consequence of the electric field of the devices.

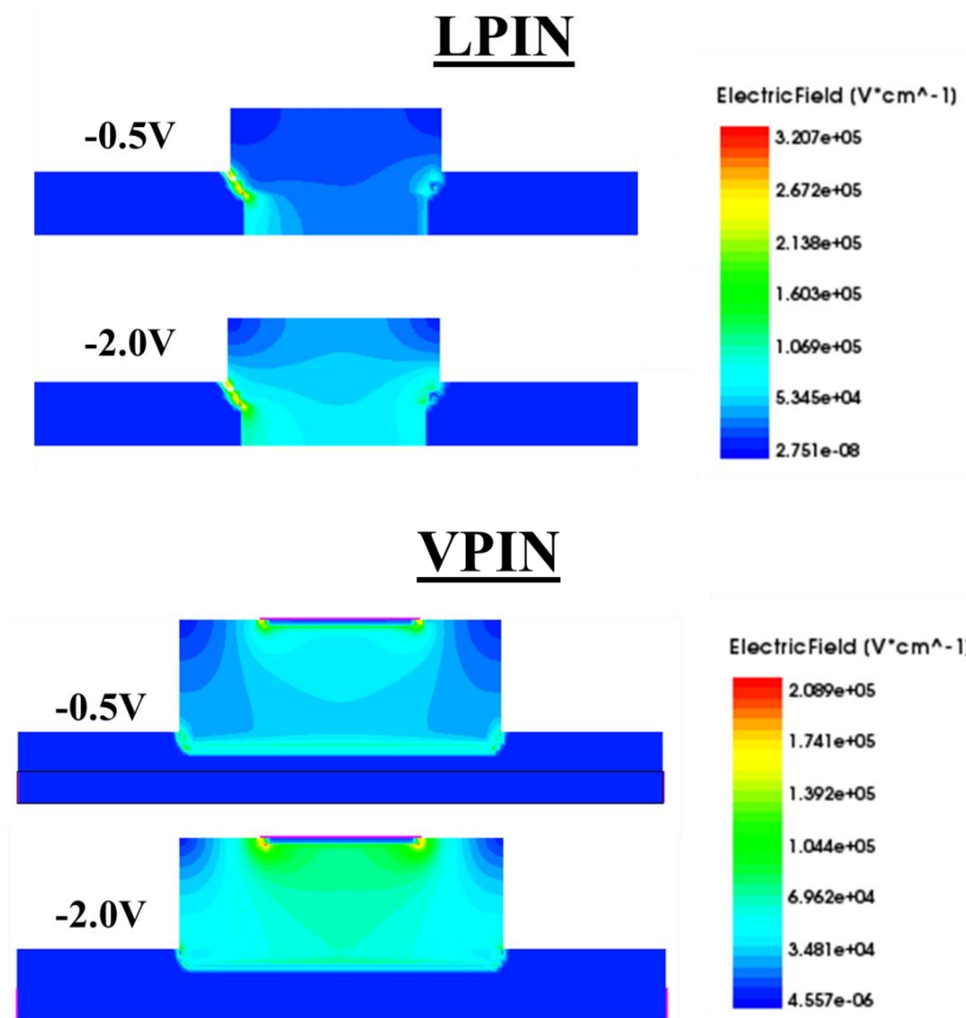

Figure VI.6. Electric field distributions of the photodiodes under two bias conditions: -0.5 V and -2.0 V. For the LPIN device, increasing the bias results in an increased electric field amplitude in the germanium for charge collection. In the case of the VPIN device, there is a strong electric field across the germanium even at low bias.

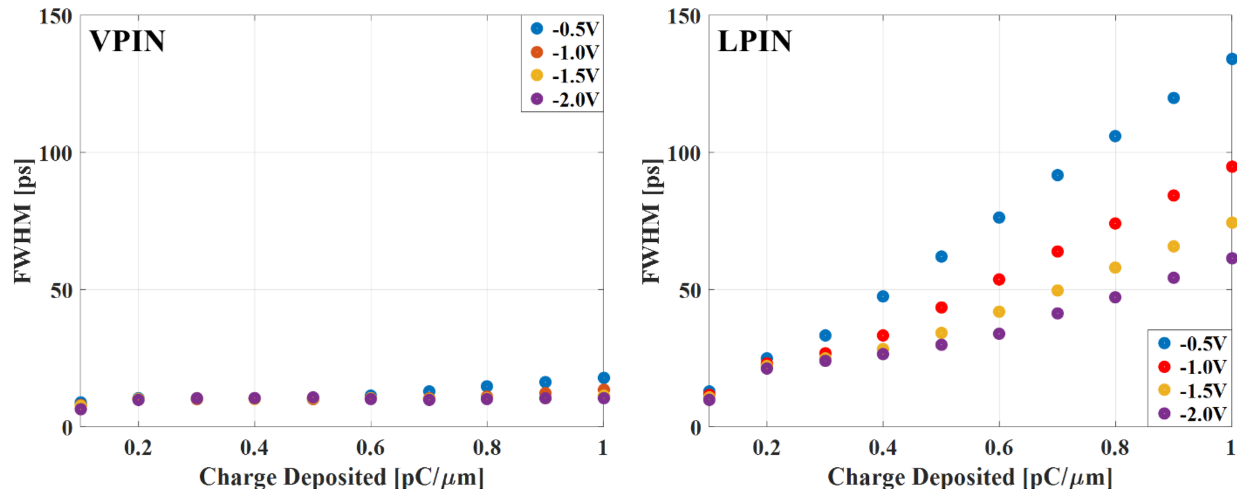

Figure VI.7. FWHMs of simulated SETs in VPIN and LPIN photodetectors as a function of charge injection under four bias conditions: -0.5V, -1.0V, -1.5V, -2.0V. Note that the LPIN devices demonstrate the similar trend of dependence on the injected charge on the induced device response (Fig. VI.2).

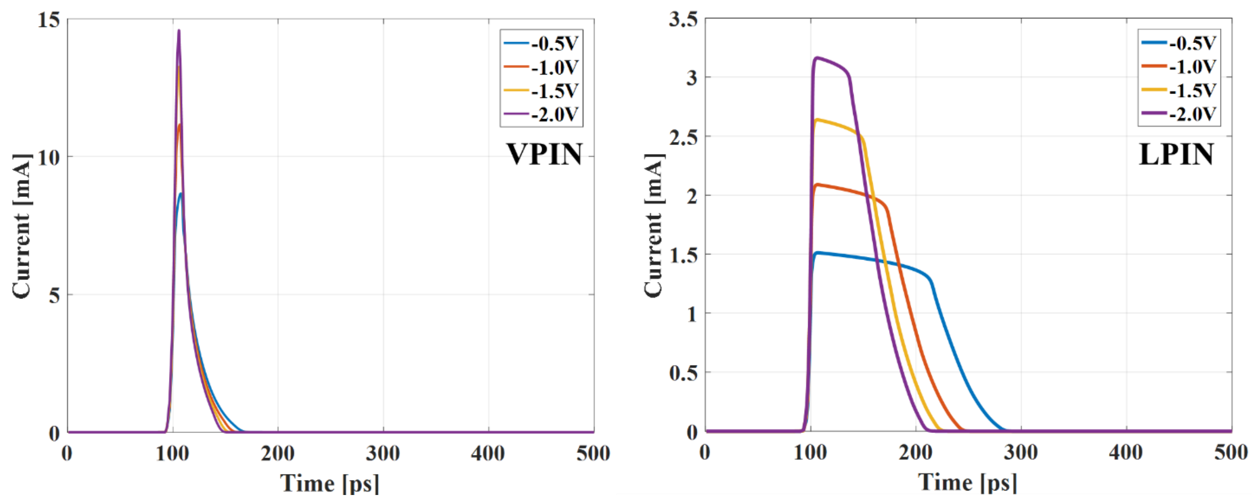

Figure VI.8. Simulated SETs as a function of bias for the same charge injection conditions (1 pC/μm) for VPIN and LPIN devices. Note that the simulated SETs demonstrate the same bias-dependent behavior that was observed during PL-SEE testing. As these are 2D simulations, the normalization length used was 1 μm.

2) *Potential Mitigation Approaches*

Photodiodes convert signals from the photonic to the electronic domain, so a SET induced in the photodiode will serve to corrupt the amplitude of the electronic signal that can propagate downstream to components along that signal path. Even when the amplitude of the transient falls

below the threshold to completely disrupt the signal state, the transient will still temporarily degrade the signal-to-noise ratio of the signal and result in an increase in the bit error rate during the duration of the transient. Therefore, an individual transient not only impacts the signal state in which the transient originates but any subsequent signal states that occur until the conclusion of the transient. As the bit period is inversely related to the bit rate, for a given transient duration the number of impacted signal states will increase as the bit rate increases.

In addition to standard circuit-level mitigation techniques such as parity checking, two types of passive radiation mitigation design considerations could be employed when working with waveguide-integrated photodiodes based on observations made in this work. The first mitigation principle is to minimize device dimensions that contribute to the radiation response of the device. Photodiodes intended for use in silicon photonics application are likely to be limited by the transit time of carriers across the intrinsic germanium region so selecting a device with features that minimize this distance will reduce the duration of transients induced within the device. Furthermore, dimensions that contribute to the areal footprint of the device will impact the rate at which transients occur; with smaller footprints resulting in smaller error rates. For either geometry, reducing the length of the photodiode (direction perpendicular to the cross-sectional cut) offers the potential for greater areal reduction with less impact on the performance of the device compared to reducing the width or height of the photodiode. For the devices considered in work where the width of the germanium region is a tunable dimension, reducing the width dimension will reduce the sensitive error in both geometries while the transient duration will also be reduced in the LPIN geometries.

The second mitigation principle relies on leveraging the voltage-dependent response of the geometries. The minimal voltage-dependent transient duration in the VPIN photodiode geometry lends itself to applications that operate within a range of operation voltages. As the duration of transients induced in the photodiode will remain relatively constant, predicted error rates should remain valid even if the operating voltage varies. In contrast, the voltage-dependent transient duration in the LPIN photodiode geometry affords the potential to reduce the transient duration in the photodiode by increasing the operating voltage. From a performance and manufacturing perspective the LPIN geometry is the preferable option for inclusion in silicon photonic circuits, so it is likely that these geometries will appear in commercial-off-the-shelf systems intended for

radiation environments. While increasing the operating voltage will incur a power penalty, the transient duration can be reduced and result in lower error rates for the same photodiode design.

E. Conclusion

In this work, the pulsed-laser induced SET response of waveguide-integrated germanium photodiodes was experimentally examined for two common geometries – vertical PIN junctions and lateral PIN junctions – under different bias and pulse energy conditions. The SETs of VPIN devices exhibited a voltage-independent temporal duration that was consistently smaller than transients collected from LPIN devices at the same pulse energies. Moreover, the SETs of LPIN devices exhibited a voltage-dependent temporal duration. As the temporal response of photodiodes is dominated by the transit of carriers across the junction, design choices that impact the transit time of carriers by either changing the distance that carriers must cross or the speed at which they can drift have a significant impact on device performance. Charge transport simulations suggest that the voltage-dependent temporal response of the LPIN devices is associated with electric field amplitudes that directly affect carrier velocity [146],[147],[156]-[158]. The impact of device geometry on the transients can be related to the impact that design parameters have on the performance metrics of a device operating under more typical terrestrial conditions. Similar to other SET susceptible devices, radiation tolerance of the device depends on the system response to the injected transient and the operating environment of the device, such as temperature [159]. Relating the radiation response of the photodiode to its geometry is critical for evaluating the impact of a design decision not only on traditional performance metrics but also on the radiation tolerance to ensure the reliability of integrated photonic systems in radiation environments.

CHAPTER VII

RADIATION-INDUCED TRANSIENT OPTICAL RESPONSE OF PHOTONIC DEVICES

In this chapter, the radiation-induced optical response of a silicon photonic waveguide to the injection and subsequent movement of charge is examined. The presence of charge within the waveguide locally modifies the refractive indices of the material and in turn impacts the optical mode propagating within the waveguide. Since the optical mode is not uniformly distributed within the waveguide core, the spatial distribution of charge injected into the waveguide will drive the optical response of the waveguides as the charge moves via diffusive processes. The dependence on the spatial distribution is a particular concern for alternative SEE testing techniques such as pulsed lasers, that utilize charge distributions that are significantly larger than the radial confinement associated with charge tracks from ionizing particles.

A. Radiation-Induced Optical Response

As the effective refractive index of an optical mode is derived from the optical parameters of the constitutive materials of the waveguide, local modification of the refractive index of the waveguide materials will result in modification of the effective refractive index of the mode [48], [160]. Engineered control over the effective index of an optical mode through mechanisms such as thermorefractive, electro-optic, and free carrier effects are critical to development of active photonic modulators for on-chip manipulation of light. However, these same processes can also result in the introduction of parasitic optical effects induced by the operating environment (e.g. thermal environment, radiation environment) that degrade device performance. To ensure reliable operation of photonic devices in harsh environments either through innate tolerance or mitigation techniques, examination of these degradation mechanisms must be examined.

For an optical mode, the wavelength of the light is typically subbandgap to remove any parasitic attenuation of the optical signal due to interband absorption, resulting in bending losses and scattering from sidewall roughness being the dominant optical loss mechanisms for undoped optical waveguides. However, in the case that impurities are introduced via contamination or intentional doping processes, the excess density of free carriers from the ionized impurities will

interact with the photons through intraband absorption, with sufficiently large carrier densities able to completely attenuate the signal. In a similar sense, the charge injected into a waveguide from an ionizing particle can be conceptualized as a spatial distribution of charge that locally modifies the refractive index of the waveguide core material. As the optical mode supported by a waveguide is a consequence of the refractive indices of the materials composing the waveguide, the modification of the refraction induced by the free carriers temporarily distorts the optical signal propagating along the waveguide analogous to a single event transient in a microelectronic device. From the notional model of the effective refractive index of an optical mode as a spatial weighted average of the electric field with the refractive indices of the waveguide, the overlap of the free carriers injected into a waveguide with the electric field of the mode will drive the radiation-induced response. For example, consider the TE optical mode depicted in Fig. VII.1 which displays a peak electric field intensity at the center of the waveguide core and with decreasing field at the Si/SiO_2 boundary of the waveguide. Carriers injected from an ionizing particle the along the center of the waveguide would more greatly impact the optical mode then the same carriers injected near the boundary due to the greater electric field intensity localized at the center of the waveguide core. While this notion of modal overlap with free carrier distributions may be relatively new to field of radiation effects, this principle is a significant design metric for photonic modulators that want to modulate the optical signal with as little resource investment as possible [161]–[163].

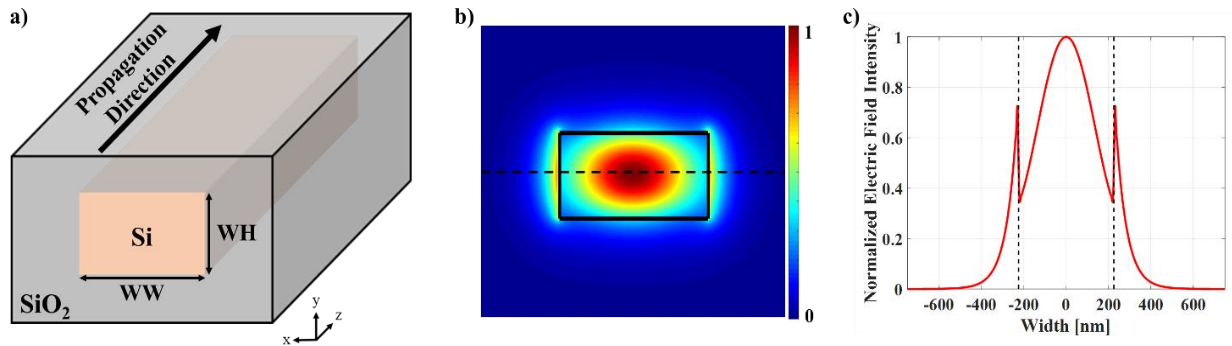

Figure VII.1. a) A diagram of a silicon ridge waveguide with the waveguide width and height denoted as the WW and HH. Light confined to the waveguide will propagate along the along the waveguide in the z-direction. b) The optical mode profile for a TE mode supported by a waveguide with dimensions of WW = 450nm and WH = 220 nm. c) A plot of the optical mode along the dashed line in (b) with the dotted lines corresponding to the Si/SiO_2 interface. Note that the optical mode practically extents into the surrounding oxide and is not uniformly distributed within the waveguide.

B. Modeling

The push to develop alternative SEE measurement techniques have led the adoption of techniques such as pulsed-laser testing and focused X-ray testing to inject charge through different mechanisms to traditional ionizing particles. A consequence of this reliance on alternative mechanisms for charge injection is that these spatial distributions of the charge will vary between the techniques. As discussed in previous chapters, the charge tracks from an ionizing particle are described as thin cylinders (radius on the order of nanometers) of high carrier densities while alternative techniques generate charge with a radial confinement on the order of micrometers. As photonic technologies mature and begin to demand characterization of the radiation response to ionizing particles, PL-SEE testing will likely serve as a popular preliminary technique to screen devices prior to costly heavy ion testing. In this case, it is imperative that 1) the impact of the spatial extent of the charge on the device response is understood and 2) there is sufficient computational approaches for estimating the device response to a given charge injection profile.

As the spatial distribution of charge will impact the subsequent optical response of the waveguide, it is useful to define a common analytic representation of the spatial extent of the injected charge. The radial charge track structure from an ionizing particle can be quite complex due to the potential creation of secondary particles and other nuclear processes [24], [164]–[166], so there is ongoing effort to 1) computationally model these charge tracks and 2) determine the minimum level of complexity that is required to accurately model ion-induced radiation effects. For the purposes of this work, a Gaussian distribution is used to define the radial confinement (x- and y- axes) carriers injected into a device

$$N(x,y,z) = N_0 e^{\frac{-(x^2+y^2)}{\sigma^2}} \qquad \text{(VII.1)}$$

where the peak carrier density and e^{-1} half-width are denoted as N_0 and σ receptively. This simplified approach of representing charge as a spatial Gaussian distribution is consistent with common approximation techniques for ion-induced SEE modelling [165] and a natural consequence of treating laser-based testing with Gaussian optics approximations [46]. Based upon

the functional form of carrier densities in Eqn. VII.2, the total amount of charge contained with a distribution Q_{dist} can be expressed as

$$Q_{dist} = qh\pi\sigma^2 N_0 \quad \text{(VII.2)}$$

where h is the thickness of the charge distribution. It should be noted that for the same peak carrier density, increasing the width increases the total charge described by the distribution. In the case that charge distributions corresponding to the same total charge are to be compared

$$N(x, y, z) = \frac{Q_{dist}}{h\pi\sigma^2} e^{\frac{-(x^2+y^2)}{\sigma^2}} \quad \text{(VII.3)}$$

Eqn. VII.3 can be used to scale the peak carrier density in accordance with the width of the distribution. This representation of the carrier density emphasizes a key comparison between ionizing particle tracks and charge injected through alternative techniques: ions create much higher peak carrier densities than the alternative techniques, but over a small smaller area. As the intent is to emulate the ionizing particles, is useful to refer to Q_{dist} as the equivalent charge deposited by an ionizing particle of a given LET.

Simulating the radiation-induced transient optical response of waveguides requires capturing both the initial distribution of charge as well as the subsequent transport of the charge through the waveguide. The temporal evolution of the charge within the device results in a corresponding perturbation to the optical modes that presents as a radiation-induced phase shift and attenuation. Similar to the PL-SEE simulation infrastructure discussed in previous Chapter IV, TCAD and nanophotonic software tools are perfectly suited to modelling charge transport and optical phenomena respectively. In the case of the optical simulations, 3D FDTD simulations provide the most rigorous approach to modelling the optical response to the carriers due to the potential for sharp carrier density gradients induced by charge injection. It should be noted that while 3D FDTD simulations provide the most rigorous approaches, the FDTD algorithm is resource intensive and typically optimized within commercial solvers, significantly limiting the potential for application within the radiation effects community.

As opposed to leveraging FDTD simulations as broadly applicable to nanophotonic problems due the brute force computation of Maxwell's equations, a more specialized computational technique to describe optical mode propagation can be used estimate the optical response to distribution of charge in a waveguide. Electromagnetic perturbation theory allows for representation of carriers in a waveguide as a perturbation to the optical mode and represented by a change in the effective refractive index [160] (Δn_{eff})

$$\Delta \mathrm{n}_{\mathrm{eff}} = c\varepsilon_0 \frac{\iint n(x,y,z)\Delta n(x,y,z)|\boldsymbol{E}|^2 dxdy}{\iint \mathrm{Re}[(\boldsymbol{E}\times\boldsymbol{H}^*)\cdot\hat{\boldsymbol{z}}]dxdy} \tag{VII.4}$$

where c is the speed of light, ε_0 is the permittivity of free space, and Δn is the perturbed refractive indices of the waveguide materials. Similar to a bulk material, the perturbation of the effective refractive is complexed-valued with the imaginary component corresponding to attenuation of the optical mode. The unperturbed optical mode (pre-charge injection) is defined by the distribution of the electric field (E) and magnetic density (H) as the well as the unmodified refractive indices of the waveguide materials. Based upon the notional weighted average model of the effective refractive index of the optical mode, the local modification of the refractive index of the waveguide core material perturbs the effective refractive index in accordance with overlap of the injected charge with the optical mode. Importantly, this perturbation only requires a single optical simulation of the unperturbed optical mode as an initial condition that can then be used to estimate the perturbation of the effective refractive index of an optical mode for any charge distribution characterized by $\Delta n(x,y,z)$. Furthermore, the spatial integrals of Eqn. VII.4 can be quickly solved by numerical techniques without any specialized software, positioning the perturbation technique as a low barrier-to-entry method for estimating radiation-induced optical responses in photonic devices.

To provide a benchmark for the perturbation approach, 3D FDTD simulations using Lumerical FDTD Solutions were conducted on a C-band silicon ridge waveguide with a height and width of 220 nm and 450 nm, respectively. Changes in the accumulated phase and transmission of the optical mode induced by a spatial distribution of charge injected in the waveguide were monitored as function of the width defined in Eqn. VII.1. Two cases were considered for the deposited charge when the width of the charge distribution was varied: constant

peak charge density (Eqn. VII.1) and constant total deposited charge (Eqn. VII.3). The carrier density-to-refractive index modification of silicon empirically determined by *Soref* [105] was used for these simulations, however it should be noted that the simulations can be conducted with alternative models (different materials or analytic models) without any loss of generality. To perform the perturbation computations, an eigenmode solver (Lumerical MODE [139]) was used to compute the unperturbed optical mode to be used with Eqn.VII.4. to compute optical response induced by the charge distribution in the waveguide. A compilation of the FDTD simulations (data points) and the perturbation approach (solid lines) for a variety of charge distributions are provided in Fig. VII.2 [167]. It can be seen that by matching the peak carrier density with increasing widths increases the magnitude of radiation-induced phase shift and attenuation. On the other hand, ensuring that distributions represent the same amount of charge results in reduced peak carrier densities as the width increases and a reduction in the radiation-induced degradation. Therefore, it can be said that trying to match the peak carrier density of an ionizing particle with a wider charge distribution will overestimate the device response while matching the total charge will underestimate the response. Furthermore, it can be seen that there is good agreement between both the rigorous 3D FDTD simulations and the perturbative approach, demonstrating the potential for the perturbative approach to estimate the radiation-induced response of the device in place of more complicated optical simulations.

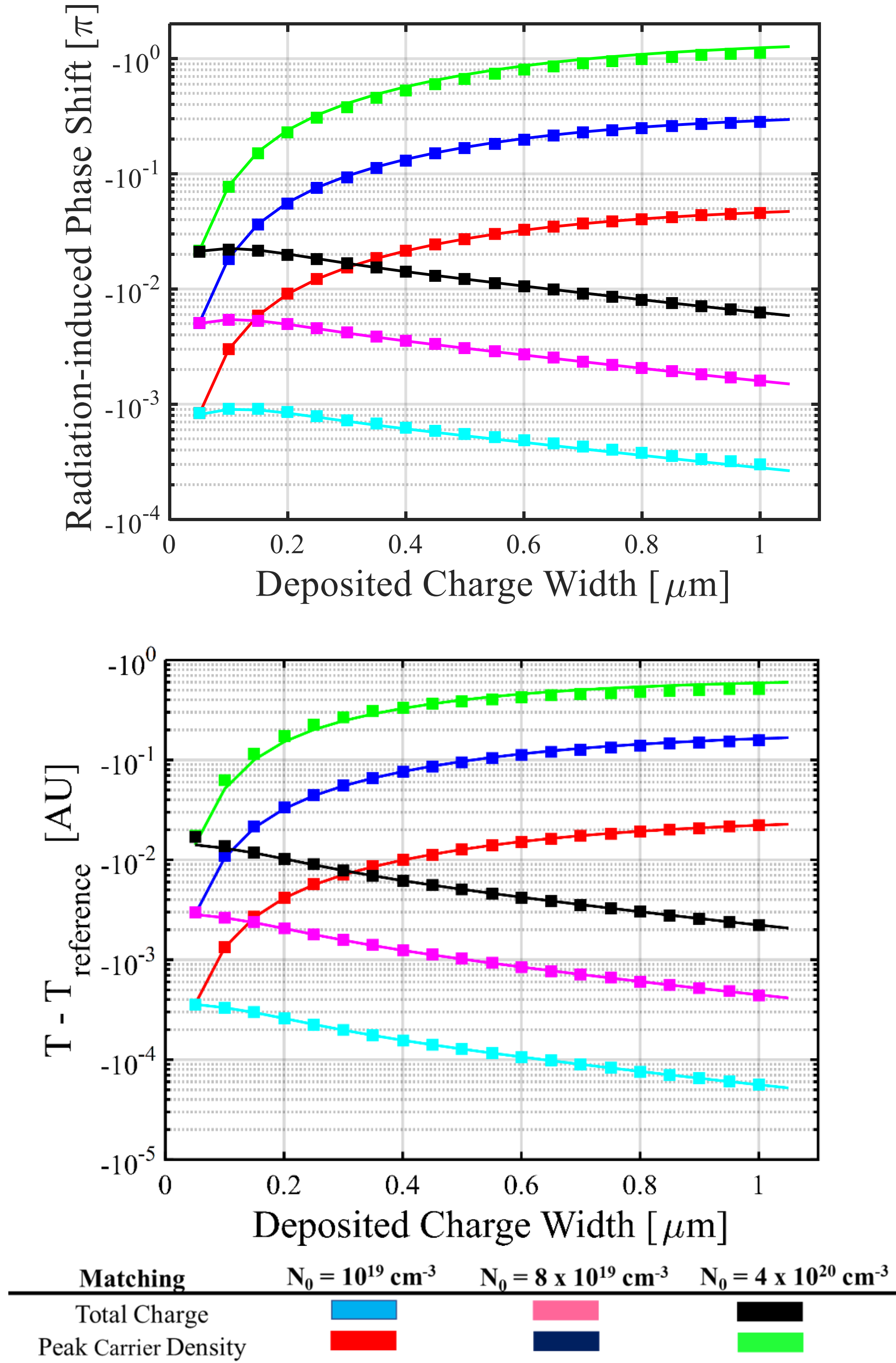

Figure VII.2. (Top) Radiation-induced phase shift and (bottom) change in transmission in reference to standard operation. Data points represent results from 3D FDTD simulations and solid lines represent effective index perturbation calculations. After [167].

C. Charge Transport

A common technique used in SEE testing is the decomposition of transient waveforms into features that can be correlated to a charge transport mechanism that is driving the device response at that time. In the case of microelectronic devices, this often takes the form of denoting the sharp peak of a transient waveform as a consequence of the prompt collection via drift of carriers deposited within a junction while the subsequent tail is related to the slower collection via diffusion. Based upon the correlation of features with charge collection mechanism, monitoring of these waveform features can be used to understand the predominant mechanisms (e.g. SOI devices have durations as there is no diffusion from the substrate [168]). This feature approach can be a seen in the previous chapter as the duration of the photodetectors reveals information related to the amplitude of the electric field in the junction.

In this section, the transient optical response of a passive photonic waveguide was examined using TCAD simulations coupled with the perturbation approach to examine the temporal characteristics of the response and the underlying mechanisms. A benefit of the perturbation approach is that it can be directly incorporated into Sentaurus TCAD through the physical model interface and used to estimate the instantaneous optical response of the waveguide to the distribution of charge currently within the waveguide at every timestep that is used for the charge transport solutions. For these simulations, a silicon ridge waveguide embedded in silicon with a height and width of 220 nm and 450 nm was used as test structure. Following standard practice, charge was injected through the middle of the waveguide with a temporal Gaussian with an envelope with a e^{-1} value of 150 fs to ensure numerical stability of the solver. No additional optical loss mechanisms were considered so the waveguide will provide unity transmission prior to charge injection. Since injected charge results in both a phase shift and attenuation of the optical mode, the temporal response of the on optical signal within the waveguide will exhibit both a phase and amplitude transient. In the case of an isolated waveguide, the transmission is the only measurable quantity and will be the focus of these discussion for simplicity. However, the mechanisms and waveform characteristics will be generalizable to the phase transient response

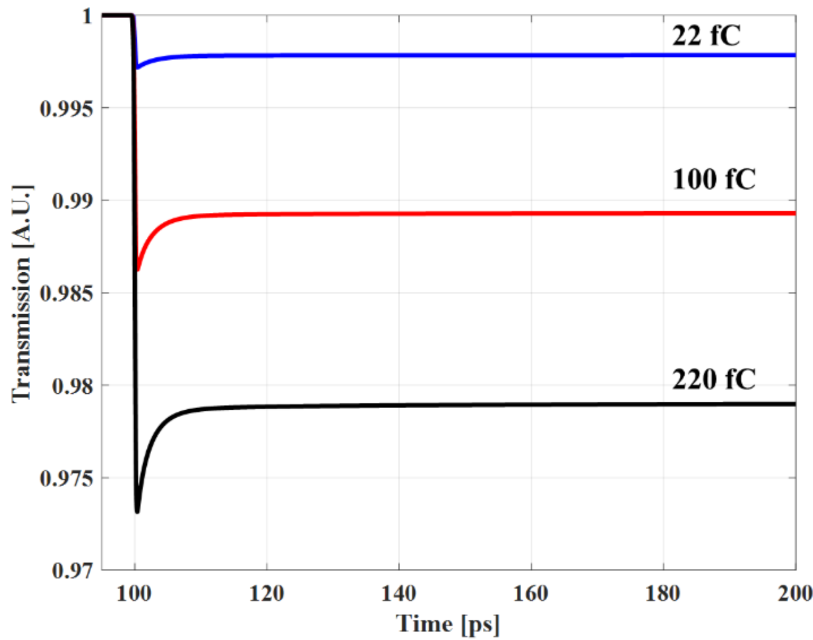

Figure VII.3. Radiation-induced change in transmission in a ridge waveguide for charge deposited of 22 fC, 110 fC and 220 fC (equivalent to a particle LET of 10, 50, and 100 MeV•cm^2/mg) with a width of σ = 10 nm. Charge injection occurs at 100 ps.

and is still computed. To begin the process of identifying features of the optical transient response, simulations of charge injection from an ionizing particle (width of σ = 10 nm) were used to inject a total charge of 22 fC, 110 fC, and 220 pC (charge equivalent of a particle with an LET of 10, 50, and 100 MeV•cm^2/mg respectively) into waveguides with the simulated transients provided in Fig. VII.3. From a radiation environment perspective, the fluence of particles greatly decreases as a function of LET with several orders of magnitude difference between the fluence of 10 and 100 MeV•cm^2/mg particles. In most cases, the impact of a 100 MeV•cm^2/mg is not even considered due to the likelihood of a device not interacting with such a particle during a mission lifetime. Therefore it can be said that if an application can tolerate the relatively small change in the transmission of the signal then then single event effects from ionizing particles will be of negligible concern. However, when testing with alternative testing techniques the wider spatial extent of the charge and the ability to easily modulate the total charge deposited will allow for testing that will show large changes in transmission (e.g. all-optical switching [169], [170]) not practically seen in a space environment.

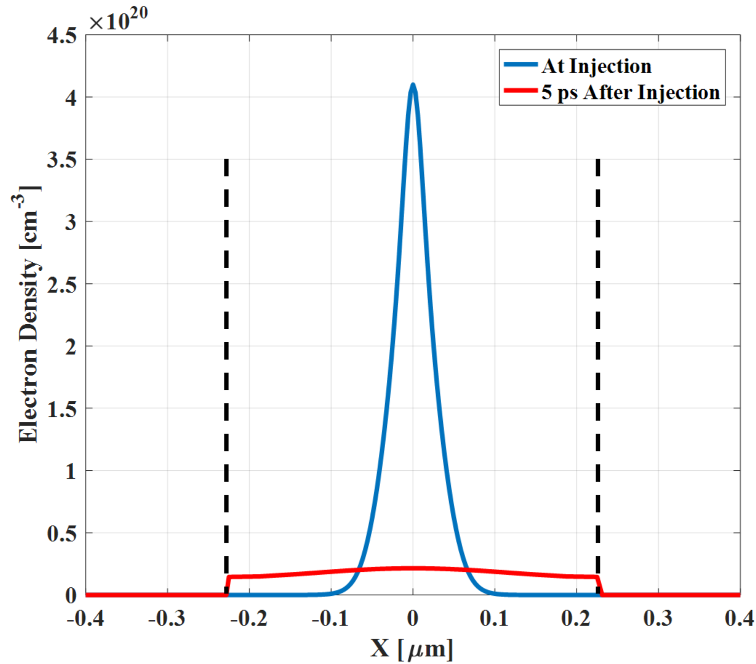

Figure VII.4. A linecut of the hole density along the width of the waveguide (dashed lines correspond to silicon boundary) at injection and 5 ps after injection of charge equivalent to a particle LET of 50 MeV•cm²/mg. The prompt lateral diffusion reduces the peak electron density, resulting in a more uniform distribution of carriers.

In each waveguide response the same prominent features can be identified: a sharp drop in transmission, a quick initial recovery, and a long tail that slowly returns to the pre-injection transmission. Contrary to microelectronic devices, passive photonic waveguides have minimal interaction with electric fields (lack of doped junctions or externally applied fields) that can drive movement of charge via drift. Therefore, the movement of charge within the waveguide will be driven by diffusion of carriers from the carrier density gradient induced by the injection of charge. While the initial distribution of charge from an ionizing particle will be represented as high carrier densities with radial confinement on the order of nanometers, the extremely large carrier density gradient created with the surrounding silicon will results in a prompt diffusion of carriers away from the strike location as the carrier densities tries to homogenize. In the event that the spatial extent of the charge distribution is less than the width of the waveguide, carriers will be able to diffuse in both lateral and longitudinal directions within the waveguide. Waveguides are fabricated with highly asymmetric dimensions (width << length), resulting in carriers diffusing laterally quickly reaching the Si/SiO_2 boundary and beginning to reduce the lateral carrier density gradient as they build up at the boundary (Fig. VII.4). As the carrier density homogenizes in the lateral

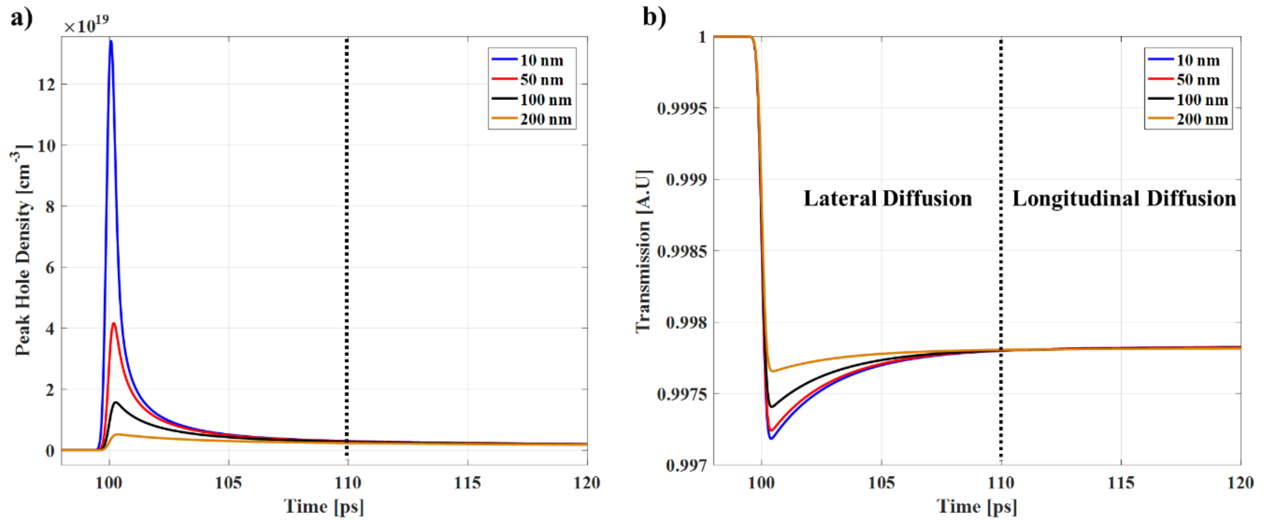

Figure VII.5. a) Peak hole density and b) Transmission for an injection event with an equivalent charge of a particle with an LET of 10 MeV•cm^2/mg injected at 100 ps for four different widths: 10 nm, 50 nm, 100 nm, 200 nm. Though there is an initial difference in the device response, the prompt lateral diffusion results across the waveguide results in equivalent device response on the order of picoseconds. Subsequent charge movement is longitudinal and as the deposited charge will remain in the waveguide core, the response remains consistent. The dotted line notionally separates the two diffusion regimes.

direction, the lateral diffusion of carriers will be minimal shortly after charge injection. Due to the effectively infinite extent that carriers can diffuse into in the longitudinal direction of the waveguide, longitudinal diffusion will continue to reduce the overall peak carrier density after lateral diffusion has ceased. It should be noted that surrounding oxides necessary to confine the optical mode to the waveguide core also ensures that carriers cannot escape the waveguide core and will remain overlapping with the optical mode until they are removed via recombinative processes. For the purposes of this work, the bulk carrier of lifetime for silicon was used (3 µs and 10 µs for electrons and holes respectively [171]) resulting in recovery to nominal transmission on the order of microseconds. Introduction of additional recombination mechanisms, such as surface recombination at the Si/SiO_2 interface introduced by fabrication imperfections [169]–[171], will result in reduced carrier lifetimes and result in faster recovery of the transmission signal similar to the impact of surface recombination on the radiation response of microelectronic devices [172].

Now that distinct features of the transient optical response of the waveguide can be related to charge transport phenomena, the significance of the spatial extent of the charge distribution injected into the waveguide can be examined. Since the sharp drop in transmission is associated with the brief time following injection were the confined carriers overlap with region of peak

electric field intensity within the waveguide, injecting the same amount of charge for increasing widths will result in smaller changes in transmission. To demonstrate this, the transient optical response of the waveguide was simulated for 22 fC injected into waveguide using the four different widths: 10 nm, 50 nm, 100 nm, and 200 nm. In order to succinctly represent diffusion in 3D, the peak hole density in the entire waveguide was monitored as a function of time and provided in Fig. VII.5a. It can be seen that increasing the width reduces the maximum peak hole density observed in the device, but quickly after injection (<10 ps) the peak hole density for the different charge distributions become effectively equal. Referring to device response (Fig. VII.5b), the expected dependence of the transmission minimum on the charge width is observed but shortly after injection the transient response become equivalent. It can be seen that with sufficiently wide charge distributions the transmission drop and the start of the tail become indistinguishable as the wide charge distribution results in minimal carrier gradient in the lateral direction, effectively eliminating the lateral diffusion process from the response.

The equivalent tails of the transients after lateral diffusion is indicative of the fact that the tail behavior is driven by the total charge injected. These observations can be corroborated by

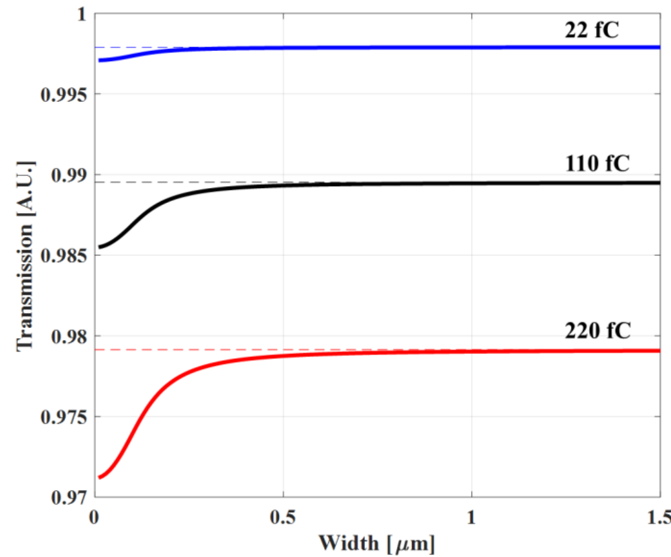

Figure VII.6. Transmission as function of the width of the charge distribution for total charge deposited of 22 fC, 110 fC and 220 fC, corresponding to charge deposited from particles with an LET of 10 MeV•cm^2/mg, 50 MeV•cm^2/mg, and 100 MeV•cm^2/mg respectively. As the width of the distribution increases, the transmission asymptotically approaches a transmission value consistent with a uniform density of carriers in the waveguide. This behavior is analogous to the transmission response of the device in time as the carriers diffuse in the waveguide.

comparing the optical response of the device for the injected charge distribution as a function of width (Fig. VII.6). To demonstrate that the response is bounded by the total charge injected into the waveguide, a total charge Q was injected in the waveguide as uniform carrier density defined by dimensions (width, thickness, length) of the waveguide in the simulation

$$N_{dep} = \frac{Q}{qwtl} \tag{VII.5}$$

and is provide by the dotted lines that the simulated results asymptotically approach. In total the observations made in this section have significant implications for alternative testing techniques attempting to emulate the device response of an ionizing particle with a larger charge distribution. Due to the larger spatial widths, alternative techniques will not be able to match both the total injected charge and the peak carrier density of the charge injected by an ionizing particle. Opting to match the charge will result in underestimating the optical response during the initial charge injection and lateral diffusion, but the transient responses will be equivalent following the completion of the lateral diffusion.

D. Mitigation Techniques - Waveguide Geometries

The mechanisms section above centered around the simulation of the movement of charge injected into waveguide within a ridge waveguide, showing that the while the initial transient response is dominated by diffusion processes, the tails of the optical responses are dictated by the total charge injected in the waveguide. The same oxide that is used to confine the optical mode to the waveguide core also ensures that carries remain overlapping with the optical mode until they are removed. In general, the carriers do not need to be removed from the waveguide materials for the waveguide to return to pre-injection behavior, the carriers just need to be delocalized from optical mode. While a ridge waveguide was used for simulations above, it by no means represents the only waveguide geometry commonly used in photonic devices [141]. Rather than completely etching the silicon away from the sides of the waveguide core, a partial etch of the silicon can be performed to leave a thin slab of silicon on the oxide substrate for a waveguide geometry referred to as rib waveguide. Since waveguides require the index contrast for confinement of the optical

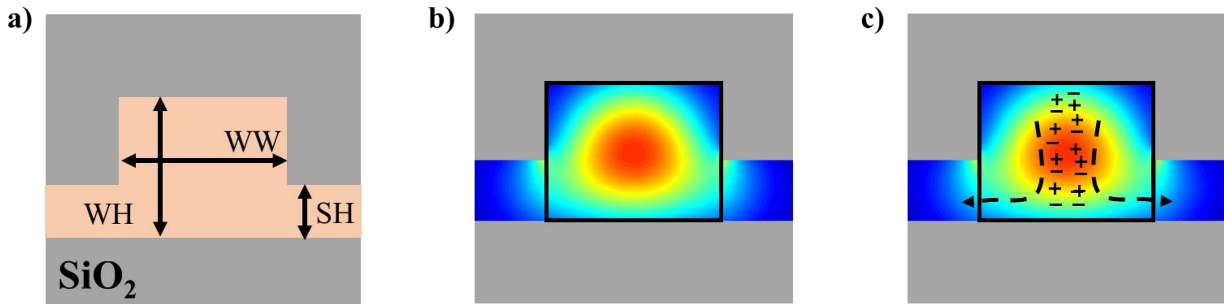

Figure VII.7. a) Cross-sectional cut of a rib waveguide. In addition to the width (WW) and height (WH) of the waveguide, the slab height (SH) is a device dimension that impacts the optical mode. b) An optical mode of rib waveguide with WW = 450 nm, WH = 220 nm, and SH of 100 nm. c) Charge deposited in the waveguide core can diffuse into the silicon and delocalize from the mode. Note the presence of the field in the silicon slab as the mode is less confined. The black box notionally defines the waveguide for comparisons.

mode, the addition of silicon pad will result in a more delocalized optical mode than in the case of the ridge waveguide. However, the silicon slab contacting the waveguide core from below creates a diffusion path for charge to diffuse away from the injection location and delocalize from the optical mode confided to the core (Fig. VII.7).

To examine the impact of carrier diffusion away from the waveguide core of a rib waveguide, the transient optical response of rib waveguides with three slab heights (50 nm, 100 nm, and 150 nm) were simulated. For each device, the total charge equivalent of a 50 MeV•cm^2/mg particle was injected with a 10 nm width into center of the waveguide. Since the silicon slab allows for charge to escape from the waveguide core, it is expected that as the pad height increases, the ratio of the charge in the waveguide core compared to the total charge injected would decrease (demonstrated in Fig. VII.8a). The reduction of charge in the waveguide will not only reduce the sharp drop in transmission, but also expedite the recovery of the waveguide transmission typified by the confinement of charge in the waveguide core in ridge waveguides as shown in Fig. VII.8b. These observations demonstrate the potential for waveguides with continuous semiconductor regions that allow for the delocalization of the carriers from the optical mode confined to the core of the waveguide to serve as a passive radiation mitigation technique for photonic devices.

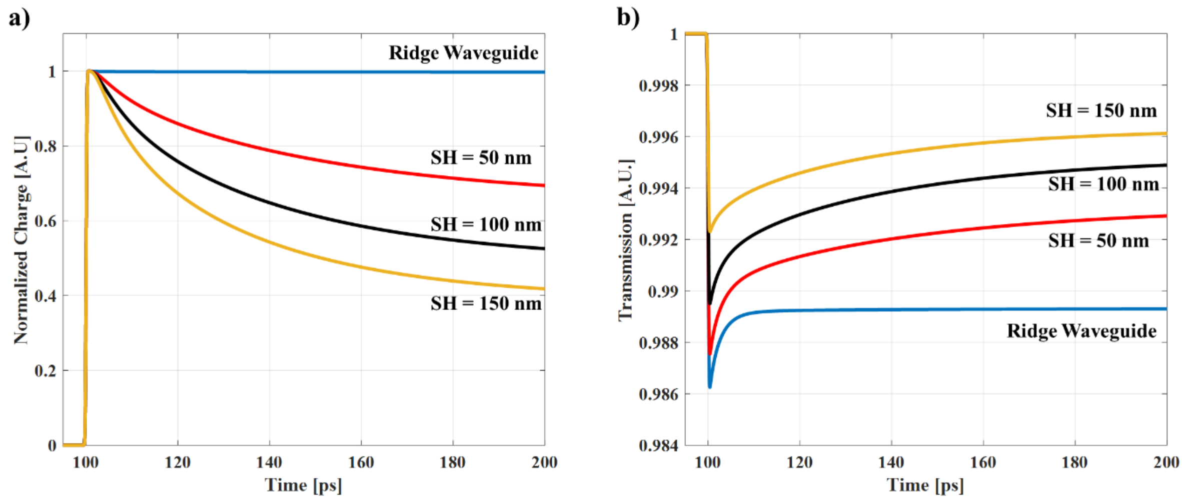

Figure VII.8. The radiation-induced response from an ionizing particle with an LET of 50 MeV•cm^2/mg is examined for a ridge waveguide and rib waveguide with three different slab heights: 50 nm, 100 nm, 150 nm. a) Charge in the waveguide core (black box in Fig. VIII.7) normalized to the total deposited charge and b) The transient response of the transmission of the waveguide. As the slab allows for carriers to diffuse away from the waveguide core, the duration of the transient will be decreased.

E. Photonic Integrated Circuits

While considering the SEE response of an individual device is informative from a mechanism perspective, it does not capture the feedback imposed by the neighboring circuits that can impact the propagation of an SEE in a circuit or system. Oftentimes these circuit responses (i.e., capacitive and resistive loading or feedback delay) can be fortuitously used to mitigate the SEE response of a circuit to ensure that even if an SET occurs at a device, the overall system response is minimal. Circuit-level simulations for assessing the radiation tolerance of a circuit topology commonly represent the radiation-induced response of a device as a parametrized compact model that can be readily integrated within a circuit model [26], [27], [173]. Photonic integrated circuit (PIC) solvers serve as the analog to electronic SPICE solvers, modelling photonic devices as transfer functions that impact the phase and amplitude of an optical signal [94]. Since the radiation-induced optical response of a photonic device can be expressed as a phase and amplitude modulation, PIC-level radiation responses to a strike on a waveguide can be characterized through optical simplified optical compact models.

Passive silicon waveguides were considered in the previous sections as they represent one of the fundamental building blocks used to construct other photonic devices such as Mach-Zehdner Modulators (MZM) and ring resonators. Therefore, the optical responses simulated by the approach outlined in the previous sections can be incorporated in PIC simulations to compute overall response of these composite photonic devices. Since there is an optical signal path between the input and output sides of these devices, a particle strike at a location in the device will impact photonic structures further down the signal path. Using Lumerical's PIC solver INTERCONNECT [174], the radiation-induced response of a ring resonator structures and MZM and ring resonator structures are considered for charge injected into a waveguide used to construct the device.

1) Passive Ring Resonator Filter

While modulation regions can be inserted into ring resonators to provide inline modulation of an input optical signal, they can find use as passive ring resonators can be used to demultiplex an input signal with multiple wavelengths by exploiting the resonant condition of the ring [53]. The simplest realization of this wavelength filtering functionality is a single waveguide ring with top and bottom waveguides optically coupled to the ring (Fig. VII.9). An input optical signal can be decomposed into a wavelength spectrum, with each wavelength component either propagating to the "Through" port (off-resonance) or coupling into the ring and passing through the "Drop" port (on-resonance). To evaluate the impact of the long tail of the radiation-induced response for a strike at the waveguide ring on the filtering capability a passive ring resonator, the uniform charge density approximation described in Eqn. VII.5 can be used to parameterize the transmission as function of charge for on and off resonance wavelengths. For simplicity, the transmission of an on-resonance wavelength in the "Through" and "Drop" ports are provided in Fig. VII.10. As the total charge injected into the waveguide increases, the resonance wavelength of the ring begins to shift eventually resulting in the input optical signal switching output optical ports as the charge imparts additional phase on the light passing through the ring.

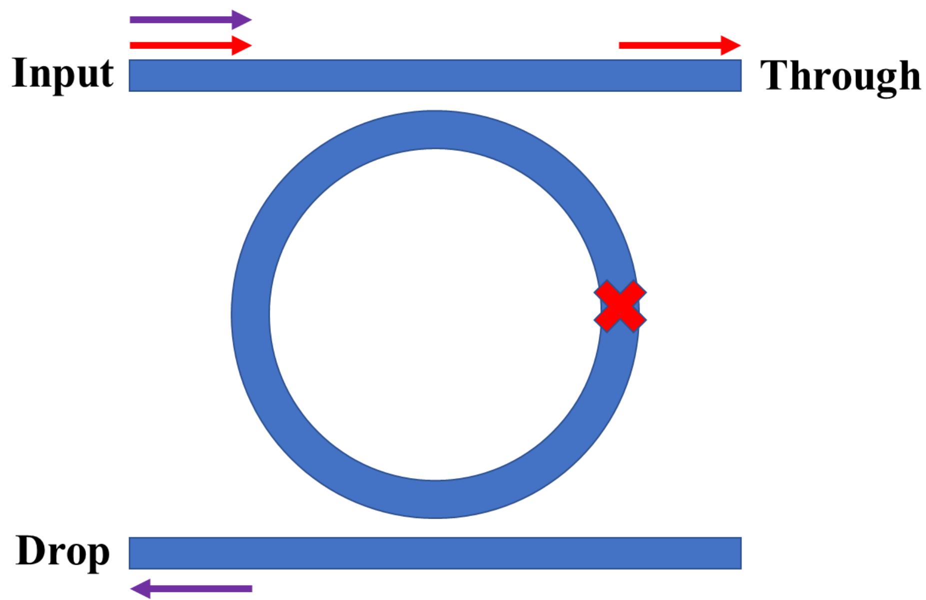

Figure VII.9. A schematic of a ring resonator used as wavelength filter. On-resonance wavelength light (purple arrow) passes through the ring to the "Drop" port while non-resonance wavelength light (red arrow) passes to the "Through" port of the device.

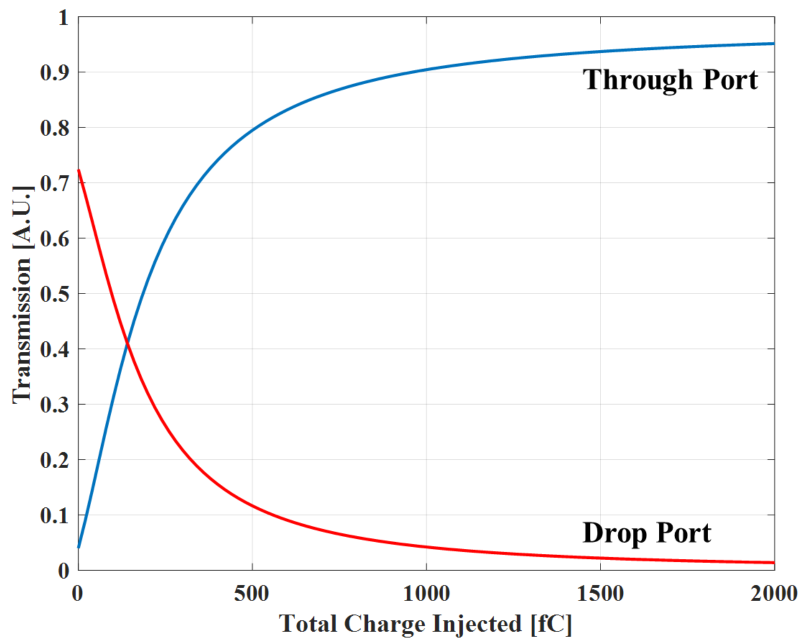

Figure VII.10. Transmission of an on-resonance signal at the Through and Drop ports of the ring resonator filter as a function of the charge injected into the waveguide. Note that as the charge increases, the resonance of the ring shifts, resulting in the signal becoming routed through the incorrect port.

2) *Mach-Zehdner Modulator*

As an MZM is commonly utilized to encode data carried by a voltage signal onto an optical signal, the input is a continuous wave optical signal that is transformed into an output signal that falls within an intensity range that can be used to denote signal states. Using the ridge waveguides examined above, an MZM with modulation in a single arm was "struck" with a 10 nm wide charge distribution that deposits equivalent charge of particle with an LET of 100 MeV cm^2/mg. In an attempt to emulate on-chip operation with a 3 dB transmission range centered on the quadrature point, the MZM was held at a nominal transmission of 0.75. The radiation-induced change in transmission of the MZM were considered for two strike locations: in the input waveguide and in the arm without the active phase modulator (Fig. VII.11). Since the operation of MZMs are interferometric in nature, both the radiation-induced phase and amplitude response must be considered in the waveguide to fully model the response of the MZM to a particle strike (Fig. VII.12). A particle strike at the input of the waveguide will attenuate the incoming optical signal prior to being split, but as the modulation in an MZM is driven by the phase difference from in the waveguide arms, the radiation-induced phase shift does not contribute to the radiation response of MZM. For a particle strike in the arm, the transmission of the MZM is sensitive both the phase shift and amplitude modulation of the light. Furthermore, the magnitude of radiation-induced device response induced by a strike in the modulator arm is dependent on the operating condition of the device; the closer the nominal state is to the quadrature point, the more susceptible the MZM will be to charge injection.

Spatial SEE sensitivity is a common occurrence during testing of devices and circuits as some structures are inherently more radiation tolerant than others. At heavy ion facilities

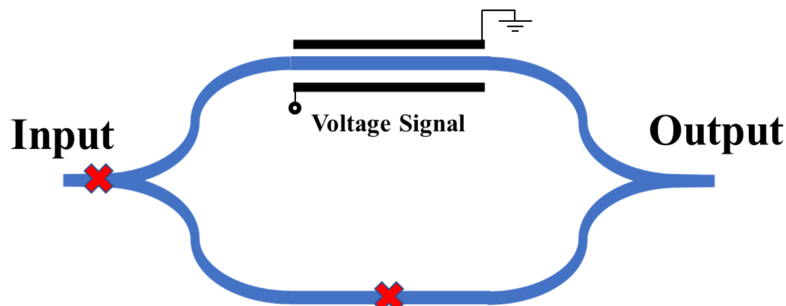

Figure VII.11. A schematic of a Mach-Zehnder modulator with active phase in the bottom arm. An input continuous wave (CW) signal is input into the device and a voltage signal is encoded onto the device. The impact of the device response for a particle strike (red x) at the input and at the arm is considered.

traditionally used for SEE testing the potential location that an ionizing particle will strike can be confined to diameters on the order of centimeters, typically resulting in the potential for particle strikes in multiple devices within a circuit. The indiscriminate area over which the particle can be strike ensures that output measurements will be a combination of SEEs originating at distinct locations within the devices circuit. In the case of the MZM simulations described above, Radiation-induced optical measurements will be a dataset that is a combination of strikes on the input and output waveguides as well as the modulator arms. In the case of less complex structures, it is reasonable to include reference structures (such as a simple waveguide) that can be used to try and categorize measurements into strike locations, but this quickly becomes infeasible with large structures and PICs with many components. Therefore, incorporation of radiation-induced optical responses at the waveguide level as compact models in PIC solvers will provide predictive capabilities for circuit level response as well as a strategy to help isolate the origin of SEEs within a PIC.

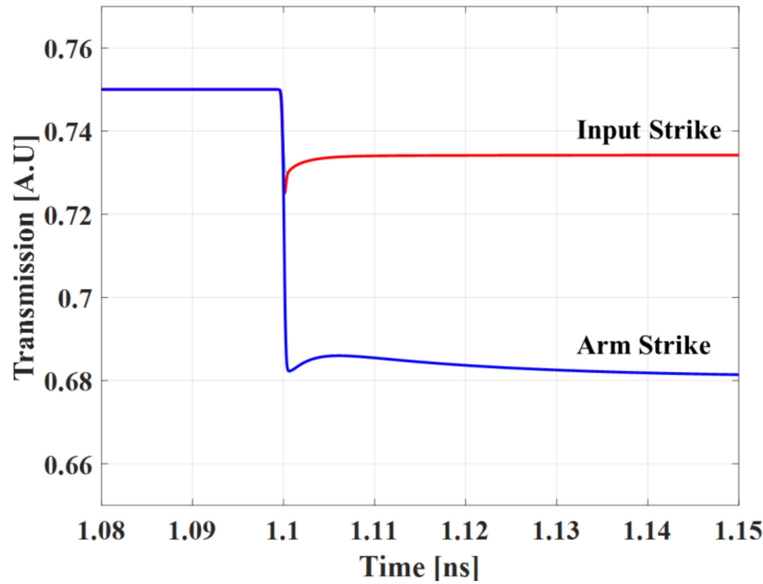

Figure VII.12. The change in transmission of the MZM as function of time for a particle strike at two locations: the input (red) and the arm (blue). For this operating condition, the strike at the arm results in a greater decrease in transmission than for a strike at the input as the radiation-induced phase shift also impacts the interferometric behavior of the MZM.

3) PL-SEE Testing

There has been growing push within the PL-SEE testing community to treat the spot size of the laser pulse as a tunable parameter to attempt to calibrate the laser-induced transient response with the response induced by an ionizing particle [175]. For a constant pulse energy, increasing the spot size of the laser pulse decreases both the intensity and radial confinement of the light. In the case of PL-SEE testing at TPA wavelengths, an increasing spot size decreases the peak and increases the width of the injected charge distribution. Since both the peak carrier density and the total charge injected in the waveguide impact the radiation-induced optical response, the adjustment of the laser spot size used during PL-SEE testing will significantly impact the measured response.

A common practice in SEE testing is the identifying a threshold testing value (LET for particles, pulse energy for lasers) that is necessary for inducing a functional change in the device or circuit. In the case of the MZM described within this section held at unity transmission, the functional change can be considered as 50% transmission. Using a simplified analytic model for TPA charge generation [175], the charge profile deposited by a pulsed laser with a pulse duration of 150 fs can be parameterized as a function of pulse energy and beam spot size and used with the perturbation approach to estimate the optical response of a struck waveguide at the time of injection. For PL-SEE testing on a MZM arm, the transmission as a function of pulse energy for three different spot sizes is provided in Fig. VII.13. As expected, increasing the spot size of the

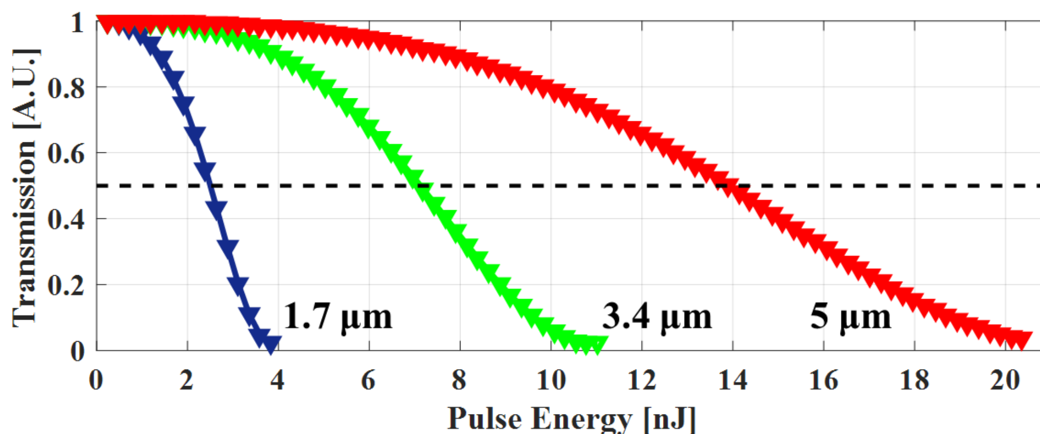

Figure VII.13. Transmission as a function of pulse energy for TPA charge injection for three spot size (e^{-2}): 1.7 µm, 3.4 µm, and 5.0 µm. Note that increasing the beam spot size increases the threshold pulse energy.

laser pulse increases the threshold energy characterized by the PL-SEE measurements, complicating comparisons of measurements conducted with different beam spot size (and by extension ionizing particles).

F. Conclusion

In this work, the radiation-induced transient optical response of a passive silicon waveguide under a variety of charge injection conditions was computationally examined using the combination of a computationally efficient optical estimation technique and Sentaurus TCAD. It was shown that the optical response of the waveguide depends on both the peak carrier density and total charge injected into the waveguide, a potential complication for alternative testing techniques which will likely overestimate the radiation-induced response. The transient optical response of the waveguide is driven by diffusion of charge and can be decomposed into a 1) transmission drop, 2) short recovery, and 3) long tail. While the initial response (transmission drop and short recovery) is dependent upon the spatial distribution of charge, the diffusion of charge will homogenous the carrier distribution resulting in the tail of the response dependent upon the total charge injected into the waveguide. Since waveguides serve as the fundamental building blocks of photonic devices and PICs, the radiation-induced optical response of the waveguide was used to develop radiation compact model for PIC solvers to estimate system level radiation responses. Overall, the oxide cladding necessary for optical confinement also truncates the semiconductor region of the waveguide, reducing the total amount of charge deposited by an ionizing particle similar to silicon-on-insulator microelectronics. From the perspective of integrated photonics, it would be expected that the photonic devices will be inherently radiation tolerant, with any susceptibility occurring in the electronic device layer.

CHAPTER VIII

CONCLUSIONS AND FUTURE WORK

The shortage of testing hours at high energy particle accelerators has long been a concern within the radiation effects community and a burgeoning space industry is only going to exacerbate the demand for these facilities. To partially satisfy the demand for preliminary SEE testing hours, alternative testing techniques have been proposed to emulate the injection of charge in a device using alternative charge generation mechanisms. Pulsed laser testing is one such technique that has enjoyed considerable use within the radiation effects community, relying on tabletop pulsed laser systems to deposit localized regions of charge through photon energy absorption as opposed to the columbic interaction of ionizing particles. As the intent of ground-based testing is to emulate the operation environment, the differences between the physical processes as well as the resultant charge distribution need to be critically examined to understand the potential pitfalls and limitations of using alternative testing techniques.

This dissertation focuses on the development of simulation tools that can be used to provide qualitative estimates of SEE measurements as well as facilitate the examination of the underlying mechanisms driving these device responses. A PL-SEE simulation infrastructure was developed using rigorous nanophotonic optical solvers and charge transport solvers to quantitatively simulate the current transients that would be measured from a PL-SEE measurement system. The decision to use a nanophotonic optical solver was driven by the fact that the small features of modern microelectronics are well below the testing wavelength of PL-SEE systems. Based on nanophotonic simulations of simplified FinFET structures, an experimental campaign measured a polarization-dependent PL-SEE device response that is due to energy enhancement from plasmonic interactions within the fin of the device. The potential for nanophotonic processes to contribute to charge generation is a problematic notion for reliably extrapolating PL-SEE measurements to the traditional SEE measurements.

As integrated photonics technologies continue to mature, the moniker of next generation devices will not only apply to FinFETs and Gate-All-Around nanowire transistors but to on-chip photonic structures that provide significantly improved performance metrics over traditional microelectronics. Given the impending adoption of integrated photonics in space-based

applications, it is reasonable to preemptively examine photonic devices to assess potential sensitive devices and identify the degradation mechanisms that drive device response. While some efforts have been expended for characterizing TID and DD on various photonic components, little has been done for SEE. Therefore, the second half of this work focuses on the measurement and simulation of SEEs in photonic components. The impact of two commonly fabricated photodiode geometries on PL-SEE measurements were examined, with vertical PIN photodiodes exhibiting much less susceptibility to SEEs than lateral PIN photodiodes. Finally, a computationally efficient technique for estimating the optical response of waveguides induced by a charge distribution is discussed and used to simulate the optical transient response of waveguides. The optical response induced in a waveguide is shown to be dependent on both the peak carrier density as well as the width of the charge injected into a waveguide, a problematic notion for alternative techniques that create charge distributions with less lateral confinement and lower peak carrier densities.

As the need to characterize integrated photonics increases so too will the available devices and the necessary modifications of existing measurement systems to accommodate the additional equipment needed to directly measurement optical signals. A particular challenge for measuring integrated photonic devices is coupling light on/off chip as both edge coupled and grating coupled configurations require relatively precise positioning to ensure consistent optical measurements. These challenges will be overcome first in PL-SEE measurement systems, allowing the mapping of spatial sensitivity of photonic devices and PICs. Based on the simulation efforts in this work, it would be expected that passive photonic structures will be rather tolerant to SEEs, with resonant structures like the waveguide rings being the most likely place to observe a potential SEE. It is expected that the SEE sensitivity in integrated photonics will be primarily attributed to the electronics (i.e. modulators, photodiode, driver circuitry) and not the photonic structures themselves.

REFERENCES

[1] ESA, "Space debris by the numbers." Accessed: Apr. 2021. [Online]. Available: https://www.esa.int/Safety_Security/Space_Debris/Space_debris_by_the_numbers.

[2] K. M. Warren, B. D. Sierawski, R. A. Reed, R. A. Weller, C. Carmichael, A. Lesea, M. H. Mendenhall, P. E. Dodd, R. D. Schrimpf, L. W. Massengill, T. Hoang, H. Wan, J. L. De Jong, R. Padovani, and J. J. Fabula, "Monte-Carlo based on-orbit single event upset rate prediction for a radiation hardened by design latch," *IEEE Trans. Nucl. Sci.*, vol. 54, no. 6, pp. 2419–2425, 2007.

[3] R. A. Reed, J. Kinnison, J. C. Pickel, S. Buchner, P. W. Marshall, S. Kniffin, and K. A. LaBel, "Single-event effects ground testing and on-orbit rate prediction methods: The past, present, and future," *IEEE Trans. Nucl. Sci.*, vol. 50 III, no. 3, pp. 622–634, 2003.

[4] E. L. Petersen, "The seu figure of merit and proton upset rate calculations," *IEEE Trans. Nucl. Sci.*, vol. 45, no. 6 PART 1, pp. 2550–2562, 1998.

[5] P. Blasi, "The origin of galactic cosmic rays," *Astron. Astrophys. Rev.*, vol. 21, no. 70, pp. 1–73, Nov. 2013.

[6] R. A. Mewaldt, "Elemental Composition and Energy Spectra of Galactic Cosmic Rays," in *Proc. Workshop on the Interplanetary Charged Particle Environment*, 1988, pp. 121–132.

[7] E. G. Stassinopoulos and J. P. Raymond, "The Space Radiation Environment for Electronics," *Proc. IEEE*, vol. 76, no. 11, pp. 1423–1442, Nov. 1988.

[8] J. L. Barth, C. S. Dyer, and E. G. Stassinopoulos, "Space, atmospheric, and terrestrial radiation environments," *IEEE Trans. Nucl. Sci.*, vol. 50 III, no. 3, pp. 466–482, 2003.

[9] M. A. Xapsos, P. M. Neill, and T. P. Brien, "Near-earth space radiation models," *IEEE Trans. Nucl. Sci.*, vol. 60, no. 3, pp. 1691–1705, 2013.

[10] P. Jiggens, M. A. Chavy-Macdonald, G. Santin, A. Menicucci, H. Evans, and A. Hilgers, "The magnitude and effects of extreme solar particle events," *J. Sp. Weather Sp. Clim.*, vol. 4, 2014.

[11] A. J. Tylka, "CREME96: A Revision of the Cosmic Ray Effects on Micro-Electronics Code," vol. 44, no. 6, pp. 2150–2160, 1997.

[12] R. A. Weller, M. H. Mendenhall, R. A. Reed, R. D. Schrimpf, K. M. Warren, B. D. Sierawski, and L. W. Massengill, "Monte Carlo simulation of single event effects," *IEEE Trans. Nucl. Sci.*, vol. 57, no. 4 PART 1, pp. 1726–1746, 2010.

[13] M. H. Mendenhall and R. A. Weller, "A probability-conserving cross-section biasing mechanism for variance reduction in Monte Carlo particle transport calculations," *Nucl. Instruments Methods Phys. Res. Sect. A Accel. Spectrometers, Detect. Assoc. Equip.*, vol. 667, pp. 38–43, 2012.

[14] D. Heynderickx, B. Quaghebeur, J. Wera, E. J. Daly, and H. D. R. Evans, "New radiation environment and effects models in the European Space Agency's Space Environment Information System (SPENVIS)," *Sp. Weather*, vol. 2, no. 2, pp. 26–29, 2005.

[15] R. C. Baumann, “Radiation-induced soft errors in advanced semiconductor technologies,” *IEEE Trans. Device Mater. Reliab.*, vol. 5, no. 3, pp. 305–315, 2005.

[16] P. E. Dodd and L. W. Massengill, “Basic mechanisms and modeling of single-event upset in digital microelectronics,” *IEEE Trans. Nucl. Sci.*, vol. 50, no. 3, pp. 583–602, Jun. 2003.

[17] F. B. McLean and T. R. Oldham, “Charge Funneling in N- and P-Type Si Substrates,” *IEEE Trans. Nucl. Sci.*, vol. 29, no. 6, pp. 2017–2023, Dec. 1982.

[18] P. E. Dodd, “Device Simulation of Charge Collection and Single-Event Upset,” *IEEE Trans. Nucl. Sci.*, vol. 43, no. 2, pp. 561–575, Apr. 1996.

[19] J. F. Ziegler, “SRIM - The Stopping and Range of Ions in Matter.” Accessed: Apr. 2021. [Online]. Available: www.srim.org/SRIM/SRIM2011.htm.

[20] K. M. Warren, R. A. Weller, B. D. Sierawski, R. A. Reed, M. H. Mendenhall, R. D. Schrimpf, L. W. Massengill, M. E. Porter, J. D. Wilkinson, K. A. LaBel, and J. H. Adams, “Application of RADSAFE to model the single event upset response of a 0.25 µm CMOS SRAM,” *IEEE Trans. Nucl. Sci.*, vol. 54, no. 4, pp. 898–903, 2007.

[21] K. M. Warren, R. A. Weller, M. H. Mendenhall, R. A. Reed, D. R. Ball, C. L. Howe, B. D. Olson, M. L. Alles, L. W. Massengill, R. D. Schrimpf, N. F. Haddad, S. E. Doyle, D. McMorrow, J. S. Melinger, and W. T. Lotshaw, “The contribution of nuclear reactions to heavy ion single event upset cross-section measurements in a high-density SEU hardened SRAM,” *IEEE Trans. Nucl. Sci.*, vol. 52, no. 6, pp. 2125–2131, 2005.

[22] B. D. Sierawski, J. A. Pellish, R. A. Reed, R. D. Schrimpf, K. M. Warren, R. A. Weller, M. H. Mendenhall, J. D. Black, A. D. Tipton, M. A. Xapsos, R. C. Baumann, X. Deng, M. J. Campola, M. R. Friendlich, H. S. Kim, A. M. Phan, and C. M. Seidleck, “Impact of low-energy proton induced upsets on test methods and rate predictions,” *IEEE Trans. Nucl. Sci.*, vol. 56, no. 6, pp. 3085–3092, 2009.

[23] P. E. Dodd, M. R. Shaneyfelt, K. M. Horn, D. S. Walsh, G. L. Hash, T. A. Hill, B. L. Draper, J. R. Schwank, F. W. Sexton, and P. S. Winokur, “SEU-sensitive volumes in bulk and SOI SRAMs from first-principles calculations and experiments,” *IEEE Trans. Nucl. Sci.*, vol. 48, no. 6 I, pp. 1893–1903, 2001.

[24] N. A. Dodds, R. A. Reed, M. H. Mendenhall, R. A. Weller, M. A. Clemens, P. E. Dodd, M. R. Shaneyfelt, G. Vizkelethy, J. R. Schwank, V. Ferlet-Cavrois, J. H. Adams, R. D. Schrimpf, and M. P. King, “Charge generation by secondary particles from nuclear reactions in BEOL materials,” *IEEE Trans. Nucl. Sci.*, vol. 56, no. 6, pp. 3172–3179, 2009.

[25] K. M. Warren, A. L. Sternberg, R. A. Weller, M. P. Baze, L. W. Massengill, R. A. Reed, M. H. Mendenhall, and R. D. Schrimpf, “Integrating circuit level simulation and Monte-Carlo radiation transport code for single event upset analysis in SEU hardened circuitry,” *IEEE Trans. Nucl. Sci.*, vol. 55, no. 6, pp. 2886–2894, 2008.

[26] J. S. Kauppila, A. L. Sternberg, M. L. Alles, A. Matt Francis, J. Holmes, O. A. Amusan, and L. W. Massengill, “A bias-dependent single-event compact model implemented into BSIM4 and a 90 nm CMOS process design kit,” *IEEE Trans. Nucl. Sci.*, vol. 56, no. 6, pp. 3152–3157, 2009.

[27] D. A. Black, W. H. Robinson, I. Z. Wilcox, D. B. Limbrick, and J. D. Black, “Modeling of Single Event Transients with Dual Double-Exponential Current Sources: Implications for Logic Cell Characterization,” *IEEE Trans. Nucl. Sci.*, vol. 62, no. 4, pp. 1540–1549, 2015.

[28] L. W. Massengill, B. L. Bhuva, W. T. Holman, M. L. Alles, and T. D. Loveless, “Technology scaling and soft error reliability,” *IEEE Int. Reliab. Phys. Symp. Proc.*, 2012.

[29] M. P. King, R. A. Reed, R. A. Weller, M. H. Mendenhall, R. D. Schrimpf, B. D. Sierawski, A. L. Sternberg, B. Narasimham, J. K. Wang, E. Pitta, B. Bartz, D. Reed, C. Monzel, R. C. Baumann, X. Deng, J. A. Pellish, M. D. Berg, C. M. Seidleck, E. C. Auden, *et al.*, “Electron-induced single-event upsets in static random access memory,” *IEEE Trans. Nucl. Sci.*, vol. 60, no. 6, pp. 4122–4129, 2013.

[30] S. Girard, A. Alessi, N. Richard, L. Martin-Samos, V. De Michele, L. Giacomazzi, S. Agnello, D. Di Francesca, A. Morana, B. Winkler, I. Reghioua, P. Paillet, M. Cannas, T. Robin, A. Boukenter, and Y. Ouerdane, “Overview of radiation induced point defects in silica-based optical fibers,” *Rev. Phys.*, vol. 4, no. April, p. 100032, 2019.

[31] H. J. Barnaby, “Total-ionizing-dose effects in modern CMOS technologies,” *IEEE Trans. Nucl. Sci.*, vol. 53, no. 6, pp. 3103–3121, 2006.

[32] D. M. Fleetwood, “Evolution of total ionizing dose effects in MOS devices with moore’s law scaling,” *IEEE Trans. Nucl. Sci.*, vol. 65, no. 8, pp. 1465–1481, 2018.

[33] T. R. Oldham and F. B. McLean, “Total Ionizing Dose Effects in MOS Oxides and Devices,” *IEEE Trans. Nucl. Sci.*, vol. 50, no. 3, pp. 1706–1730, 2003.

[34] X. Shen, Y. S. Puzyrev, D. M. Fleetwood, R. D. Schrimpf, and S. T. Pantelides, “Quantum mechanical modeling of radiation-induced defect dynamics in electronic devices,” *IEEE Trans. Nucl. Sci.*, vol. 62, no. 5, pp. 2169–2180, 2015.

[35] J. R. Srour and J. W. Palko, “A framework for understanding displacement damage mechanisms in irradiated silicon devices,” *IEEE Trans. Nucl. Sci.*, vol. 53, no. 6, pp. 3610–3620, 2006.

[36] J. R. Srour, C. J. Marshall, and P. W. Marshall, “Review of displacement damage effects in silicon devices,” *IEEE Trans. Nucl. Sci.*, vol. 50, no. 3, pp. 653–670, Jun. 2003.

[37] J. R. Srour and J. M. McGarrity, “Radiation Effects on Microelectronics in Space,” *Proc. IEEE*, vol. 76, no. 11, pp. 1443–1469, 1998.

[38] G. P. Summers, E. A. Burke, and M. A. Xapsos, “Displacement damage analogs to ionizing radiation effects,” *Radiat. Meas.*, vol. 24, no. 1, pp. 1–8, 1995.

[39] M. Fox, *Optical Properties of Solids*, 2nd ed. Oxford University Press, 2002.

[40] J. D. Jackson, *Classical Electrodynamics Third Edition*. John Wiley & Sons, 2007.

[41] R. W. Boyd, *Nonlinear Optics*. Elsevier, 2007.

[42] R. F. Pierret and G. W. Neudeck, *Advanced semiconductor fundamentals*, vol. 6. Addison-Wesley Reading, MA, 1987.

[43] J. Fang, M. Reaz, S. L. Weeden-Wright, R. D. Schrimpf, R. A. Reed, R. A. Weller, M. V. Fischetti, and S. T. Pantelides, "Understanding the Average Electron-Hole Pair-Creation Energy in Silicon and Germanium Based on Full-Band Monte Carlo Simulations," *IEEE Trans. Nucl. Sci.*, vol. 66, no. 1, pp. 444–451, 2019.

[44] B. Goldstein, "Electron-hole pair creation in gallium phosphide by α particles," *J. Appl. Phys.*, vol. 36, no. 12, pp. 3853–3856, 1965.

[45] M. Nedeljkovic, R. Soref, and G. Z. Mashanovich, "Free-carrier electrorefraction and electroabsorption modulation predictions for silicon over the 1-14-μm infrared wavelength range," *IEEE Photonics J.*, vol. 3, no. 6, pp. 1171–1180, 2011.

[46] J. N. Howard, "Laser beams and resonators," *Appl. Opt.*, vol. 26, no. 4, pp. 593–593, 1987.

[47] Y. A. Vlasov, "Silicon CMOS-integrated nano-photonics for computer and data communications beyond 100G," *IEEE Commun. Mag.*, vol. 50, no. 2, pp. 67–72, Feb. 2012.

[48] A. Yariv and P. Yeh, *Photonics: optical electronics in modern communications*. Oxford University Press, 2007.

[49] R. Soref, "Mid-infrared photonics in silicon and germanium," *Nat. Photonics*, vol. 4, no. 8, pp. 495–497, 2010.

[50] D. F. G. Gallagher and T. P. Felici, "Eigenmode expansion methods for simulation of optical propagation in photonics: pros and cons," *Integr. Opt. Devices, Mater. Technol. VII*, vol. 4987, no. June 2003, p. 69, 2003.

[51] Z. Zhou, B. Yin, and J. Michel, "On-chip light sources for silicon photonics," *Light Sci. Appl.*, vol. 4, no. 11, pp. 1–13, 2015.

[52] M. J. R. Heck and J. E. Bowers, "Energy efficient and energy proportional optical interconnects for multi-core processors: Driving the need for on-chip sources," *IEEE J. Sel. Top. Quantum Electron.*, vol. 20, no. 4, 2014.

[53] W. Bogaerts, P. de Heyn, T. van Vaerenbergh, K. de Vos, S. Kumar Selvaraja, T. Claes, P. Dumon, P. Bienstman, D. van Thourhout, and R. Baets, "Silicon microring resonators," *Laser Photonics Rev.*, vol. 6, no. 1, pp. 47–73, 2012.

[54] J. E. Heebner, V. Wong, A. Schweinsberg, R. W. Boyd, and D. J. Jackson, "Optical transmission characteristics of fiber ring resonators," *IEEE J. Quantum Electron.*, vol. 40, no. 6, pp. 726–730, 2004.

[55] P. Gunter, "Electro-optical effects in ferroelectrics," *Ferroelectrics*, vol. 74, no. 1, pp. 305–307, 1987.

[56] Z. Y. Li, D. X. Xu, R. Mckinnon, S. Janz, J. H. Schmid, J. Lapointe, P. Cheben, and J. Z. Yu, "Low driving-voltage optical modulator based on carrier depletion in silicon with periodically interleaved p-n junctions," *2008 5th Int. Conf. Gr. IV Photonics, GFP*, vol. 17, no. 18, pp. 13–15, 2008.

[57] M. Zeiler, S. S. El Nasr-Storey, S. Detraz, A. Kraxner, L. Olantera, C. Scarcella, C. Sigaud, C. Soos,

J. Troska, and F. Vasey, “Radiation Damage in Silicon Photonic Mach-Zehnder Modulators and Photodiodes,” *IEEE Trans. Nucl. Sci.*, vol. 64, no. 11, pp. 2794–2801, Nov. 2017.

[58] Q. Xu, S. Manipatruni, B. Schmidt, J. Shakya, and M. Lipson, “125 Gbit/s carrier-injection-based silicon micro-ring silicon modulators,” *Opt. Express*, vol. 15, no. 2, p. 430, 2007.

[59] K. Debnath, D. J. Thomson, W. Zhang, A. Z. Khokhar, C. Littlejohns, J. Byers, L. Mastronardi, M. K. Husain, K. Ibukuro, F. Y. Gardes, G. T. Reed, and S. Saito, “All-silicon carrier accumulation modulator based on a lateral metal-oxide-semiconductor capacitor,” *Photonics Res.*, vol. 6, no. 5, p. 373, 2018.

[60] F. Gan, T. Barwicz, M. A. Popović, M. S. Dahlem, C. W. Holzwarth, P. T. Rakich, H. I. Smith, E. P. Ippen, and F. X. Kärtner, “Maximizing the thermo-optic tuning range of silicon photonic structures,” *2007 Photonics Switch. PS*, pp. 67–68, 2007.

[61] A. Masood, M. Pantouvaki, D. Goossens, G. Lepage, P. Verheyen, J. Van Campenhout, P. Absil, D. Van Thourhout, and W. Bogaerts, “Fabrication and characterization of CMOS-compatible integrated tungsten heaters for thermo-optic tuning in silicon photonics devices,” *Opt. Mater. Express*, vol. 4, no. 7, p. 1383, 2014.

[62] I. Young, E. M. Mohammed, J. T. S. Liao, A. M. Kern, S. Palermo, B. A. Block, M. R. Reshotko, and P. L. D. Chang, “Optical technology for energy efficient I/O in high performance computing,” *IEEE Commun. Mag.*, vol. 48, no. 10, pp. 184–191, 2010.

[63] T. Tsuchizawa, K. Yamada, T. Watanabe, S. Park, H. Nishi, R. Kou, H. Shinojima, and S. I. Itabashi, “Monolithic integration of silicon-, germanium-, and silica-based optical devices for telecommunications applications,” *IEEE J. Sel. Top. Quantum Electron.*, vol. 17, no. 3, pp. 516–525, 2011.

[64] S. Bhandaru, S. Hu, D. M. Fleetwood, and S. M. Weiss, “Total ionizing dose effects on silicon ring resonators,” *IEEE Trans. Nucl. Sci.*, vol. 62, no. 1, pp. 323–328, Feb. 2015.

[65] F. Morichetti, S. Grillanda, S. Manandhar, V. Shutthanandan, L. Kimerling, A. Melloni, and A. M. Agarwal, “Alpha Radiation Effects on Silicon Oxynitride Waveguides,” *ACS Photonics*, vol. 3, no. 9, pp. 1569–1574, 2016.

[66] Q. Du, J. Michon, B. Li, D. Kita, D. Ma, H. Zuo, S. Yu, T. Gu, A. Agarwal, M. Li, and J. Hu, “Real-time, in situ probing of gamma radiation damage with packaged integrated photonic chips,” *Photonics Res.*, vol. 8, no. 2, p. 186, 2020.

[67] P. S. Goley, Z. E. Fleetwood, and J. D. Cressler, “Potential Limitations on Integrated Silicon Photonic Waveguides Operating in a Heavy Ion Environment,” *IEEE Trans. Nucl. Sci.*, vol. 65, no. 1, pp. 141–148, Jan. 2018.

[68] G. N. Tzintzarov, S. P. Buchner, D. Mcmorrow, J. H. Warner, M. Kaynak, L. Zimmermann, J. D. Cressler, A. Ildefonso, P. S. Goley, M. Frounchi, D. Nergui, S. G. Rao, J. Teng, J. Campbell, and A. Khachatrian, “Electronic-to-Photonic Single-Event Transient Propagation in a Segmented Mach-Zehnder Modulator in a Si/SiGe Integrated Photonics Platform,” *IEEE Trans. Nucl. Sci.*, vol. 67, no. 1, pp. 260–267, 2020.

[69] C. J. Marshall, “Proton Effects and Test Issues for Satellite Designers: Displacement Effects,” in *NSREC Short Course*, 1999, pp. 1–62.

[70] M. Caussanel, A. Canals, S. K. Dixit, M. J. Beck, A. D. Touboul, R. D. Schrimpf, D. M. Fleetwood, and S. T. Pantelides, “Doping-type dependence of damage in silicon diodes exposed to X-ray, proton, and He+ irradiations,” *IEEE Trans. Nucl. Sci.*, vol. 54, no. 6, pp. 1925–1930, 2007.

[71] N. E. Lourenco, S. Zeinolabedinzadeh, A. Ildefonso, Z. E. Fleetwood, C. T. Coen, I. Song, S. Jung, F. Inanlou, N. J. H. Roche, A. Khachatrian, D. McMorrow, S. P. Buchner, J. H. Warner, P. Paki, and J. D. Cressler, “An Investigation of Single-Event Effect Modeling Techniques for a SiGe RF Low-Noise Amplifier,” *IEEE Trans. Nucl. Sci.*, vol. 63, no. 1, pp. 273–280, 2016.

[72] L. D. Ryder, K. L. Ryder, A. L. Sternberg, J. A. Kozub, E. X. Zhang, D. Linten, K. Croes, R. A. Weller, R. D. Schrimpf, S. M. Weiss, and R. A. Reed, “Single Event Transient Response of Vertical and Lateral Waveguide-Integrated Germanium Photodiodes,” *IEEE Trans. Nucl. Sci.*, vol. 68, no. 5, pp. 801–806, 2021.

[73] K. A. Label, “External Radiation Test Facilities for Testing of Electronics: NASA Overview with Emphasis on Single Event Effects (SEE),” 2017.

[74] V. Pouget, P. Fouillat, D. Lewis, H. Lapuyade, L. Sarger, F. M. Roche, S. Duzellier, and R. Ecoffet, “An overview of the applications of a pulsed laser system for SEU testing,” *Proc. - 6th IEEE Int. On-Line Test. Work.*, pp. 52–57, 2000.

[75] D. Cardoza, S. D. Lalumondiere, N. P. Wells, M. A. Tockstein, D. L. Brewe, W. T. Lotshaw, and S. C. Moss, “Investigating Pulsed X-ray Induced SEE in Analog Microelectronic Devices,” *IEEE Trans. Nucl. Sci.*, vol. 62, no. 6, pp. 2458–2467, 2015.

[76] S. P. Buchner, F. Miller, V. Pouget, and D. P. McMorrow, “Pulsed-laser testing for single-event effects investigations,” *IEEE Trans. Nucl. Sci.*, vol. 60, no. 3, pp. 1852–1875, 2013.

[77] S. Buchner, N. Roche, J. Warner, D. McMorrow, F. Miller, S. Morand, V. Pouget, C. Larue, V. Ferlet-Cavrois, F. El Mamouni, H. Kettunen, P. Adell, G. Allen, and D. Aveline, “Comparison of single event transients generated at four pulsed-laser test facilities-NRL, IMS, EADS, JPL,” *IEEE Trans. Nucl. Sci.*, vol. 59, no. 4, pp. 988–998, 2012.

[78] D. McMorrow, J. S. Melinger, and S. Buchner, “Application of a pulsed laser for evaluation and optimization of seu-hard designs,” *IEEE Trans. Nucl. Sci.*, vol. 47, no. 3, pp. 559–565, 2000.

[79] A. Zanchi, S. Buchner, C. Hafer, S. Hisano, and D. B. Kerwin, “Investigation and mitigation of analog SET on a bandgap reference in triple-well CMOS using pulsed laser techniques,” *IEEE Trans. Nucl. Sci.*, vol. 58, no. 6, pp. 2570–2577, 2011.

[80] E. Faraud, V. Pouget, K. Shao, C. Larue, F. Darracq, D. Lewis, A. Samaras, F. Bezerra, E. Lorfevre, and R. Ecoffet, “Investigation on the SEL sensitive depth of an SRAM using linear and two-photon absorption laser testing,” *IEEE Trans. Nucl. Sci.*, vol. 58, no. 6, pp. 2637–2643, 2011.

[81] D. McMorrow, W. T. Lotshaw, J. S. Melinger, S. Buchner, and R. L. Pease, “Subbandgap laser-induced single event effects: Carrier generation via two-photon absorption,” *IEEE Trans. Nucl. Sci.*, vol. 49, no. 6, pp. 3002–3008, 2002.

[82] J. S. Laird, T. Hirao, S. Onoda, H. Itoh, and A. Johnston, "Comparison of above bandgap laser and MeV ion induced single event transients in high-speed Si photonic devices," *IEEE Trans. Nucl. Sci.*, vol. 53, no. 6, pp. 3312–3320, 2006.

[83] J. M. Hales, A. Khachatrian, S. Buchner, N. J. H. Roche, J. Warner, Z. E. Fleetwood, A. Ildefonso, J. D. Cressler, V. Ferlet-Cavrois, and D. McMorrow, "Experimental validation of an equivalent LET approach for correlating heavy-ion and laser-induced charge deposition," *IEEE Trans. Nucl. Sci.*, vol. 65, no. 8, pp. 1724–1733, 2018.

[84] V. Pouget, H. Lapuyade, P. Fouillat, D. Lewis, and S. Buchner, "Theoretical investigation of an equivalent laser LET," *Microelectronics Reliability*, vol. 41, no. 9–10. pp. 1513–1518, 2001.

[85] S. Agostinelli, J. Allison, K. Amako, J. Apostolakis, H. Araujo, P. Arce, M. Asai, D. Axen, S. Banerjee, G. Barrand, F. Behner, L. Bellagamba, J. Boudreau, L. Broglia, A. Brunengo, H. Burkhardt, S. Chauvie, J. Chuma, R. Chytracek, *et al.*, "GEANT4 - A simulation toolkit," *Nucl. Instruments Methods Phys. Res. Sect. A Accel. Spectrometers, Detect. Assoc. Equip.*, 2003.

[86] R. A. Reed, R. A. Weller, M. H. Mendenhall, D. M. Fleetwood, K. M. Warren, B. D. Sierawski, M. P. King, R. D. Schrimpf, and E. C. Auden, "Physical Processes and Applications of the Monte Carlo Radiative Energy Deposition (MRED) Code," *IEEE Trans. Nucl. Sci.*, vol. 62, no. 4, pp. 1441–1461, 2015.

[87] J. H. Adams, A. F. Barghouty, M. H. Mendenhall, R. A. Reed, B. D. Sierawski, K. M. Warren, J. W. Watts, and R. A. Weller, "CRÈME: The 2011 revision of the cosmic ray effects on micro-electronics code," *IEEE Trans. Nucl. Sci.*, 2012.

[88] L. D. Ryder, "Simulation of Optical Energy Deposition for Pulsed Laser-Induced Single Event Effects Testing in Microelectronic Devices," Masters Thesis, Dept. Elect. Eng. Comput. Sci., Vanderbilt Univ., Nashville, TN, USA, 2020.

[89] N. Suzuki, "FDTD Analysis of Two-Photon Absorption and Free-Carrier Absorption in Si High-Index-Contrast Waveguides," *J. Light. Technol.*, vol. 25, no. 9, pp. 2495–2501, 2007.

[90] A. Taflove and S. C. Hagness, *Computational Electrodynamics: The Finite-Difference Time-Domain Method*, 3rd ed. Artech House, 2005.

[91] M. Esposito, V. Tasco, F. Todisco, A. Benedetti, D. Sanvitto, and A. Passaseo, "Three Dimensional Chiral Metamaterial Nanospirals in the Visible Range by Vertically Compensated Focused Ion Beam," *Adv. Opt. Mater.*, vol. 2, no. 2, pp. 154–161, 2014.

[92] E. Almeida, O. Bitton, and Y. Prior, "Nonlinear metamaterials for holography," *Nat. Commun.*, vol. 7, no. 1, 2016.

[93] S. Hu, M. Khater, R. Salas-montiel, E. Kratschmer, S. Engelmann, W. M. J. Green, and S. M. Weiss, "Experimental realization of deep-subwavelength confinement in dielectric optical resonators," *Sci. Adv.*, vol. 4, no. 8, 2018.

[94] X. Wang, J. Pond, C. Cone, L. Chrostowski, J. Klein, J. Flueckiger, A. Liu, and D. McGuire, "Large-scale silicon photonics circuit design," in *Nanophotonics and Micro/Nano Optics II*, 2014, vol. 927706.

[95] Ansys. Lumerical FDTD Solutions. Accessed: Apr. 2021. [Online]. Available: https://www.lumerical.com/products/fdtd/.

[96] A. F. Oskooi, D. Roundy, M. Ibanescu, P. Bermel, J. D. Joannopoulos, and S. G. Johnson, "Meep: A flexible free-software package for electromagnetic simulations by the FDTD method," *Comput. Phys. Commun.*, vol. 181, no. 3, pp. 687–702, 2010.

[97] xFDTD Remcon. Accessed: Apr. 2020. [Online]. Available: https://www.remcom.com/xfdtd-3d-em-simulation-software.

[98] Synopsys Inc., *Sentaurus Device User Guide, Version G-2012.06*. 2012.

[99] R. S. Muller, T. I. Kamins, and C. Mansun, *Device Electronics for Integrated Circuits*, 3rd Revise. John Wiley & Sons, 2003.

[100] K. L. Ryder, "Comparison of Heavy Ion- and Laser- Induced Sensitive Volumes in an Epitaxial Silicon Diode," Masters Thesis, Dept. Elect. Eng. Comput. Sci., Vanderbilt Univ., Nashville, TN, USA, 2019

[101] K. L. Ryder, L. D. Ryder, A. L. Sternberg, J. A. Kozub, E. X. Zhang, S. D. La Lumondiere, D. M. Monahan, J. P. Bonsall, A. Khachatrian, S. P. Buchner, D. McMorrow, J. M. Hales, Y. Zhao, L. Wang, C. Wang, R. A. Weller, R. D. Schrimpf, S. M. Weiss, and R. A. Reed, "Comparison of Single-Event Transients in an Epitaxial Silicon Diode Resulting from Heavy Ion-, Focused X-Ray-, and Pulsed Laser-Induced Charge Generation," IEEE Trans. Nucl. Sci., vol. 68, no. 5, pp. 626–633, 2021.

[102] A. Khachatrian, N. J. H. Roche, D. McMorrow, J. H. Warner, S. P. Buchner, and J. S. Melinger, "A dosimetry methodology for two-photon absorption induced single-event effects measurements," *IEEE Trans. Nucl. Sci.*, vol. 61, no. 6, pp. 3416–3423, 2014.

[103] E. D. Palik, *Handbook of optical constants of solids*, 3rd ed. Academic press, 1998.

[104] J. M. Hales, D. McMorrow, N. J. H. Roche, A. Khachatrian, J. H. Warner, S. P. Buchner, J. S. Melinger, J. W. Perry, W. T. Lotshaw, and V. Dubikovsky, "Simulation of light-matter interaction and two-photon absorption induced charge deposition by ultrashort optical pulses in silicon," *IEEE Trans. Nucl. Sci.*, vol. 61, no. 6, pp. 3504–3511, 2014.

[105] R. Soref and B. R. Bennet, "Electrooptical Effects in Silicon," *Ferroelectrics*, vol. 74, no. 1, pp. 305–307, 1987.

[106] K. L. Ryder, L. D. Ryder, A. L. Sternberg, J. A. Kozub, E. X. Zhang, A. Khachatrian, S. P. Buchner, D. P. Mcmorrow, J. M. Hales, Y. Zhao, L. Wang, C. Wang, R. A. Weller, R. D. Schrimpf, S. M. Weiss, and R. A. Reed, "Comparison of Sensitive Volumes Associated with Ion- And Laser-Induced Charge Collection in an Epitaxial Silicon Diode," *IEEE Trans. Nucl. Sci.*, vol. 67, no. 1, pp. 57–62, 2020.

[107] R. A. Johnson, A. F. Witulski, D. R. Ball, K. F. Galloway, A. L. Sternberg, E. Zhang, L. D. Ryder, R. A. Reed, R. D. Schrimpf, J. A. Kozub, J.-M. Lauenstein, and A. Javanainen, "Enhanced Charge Collection in SiC Power MOSFETs Demonstrated by Pulse-Laser Two-Photon Absorption SEE Experiments," *IEEE Trans. Nucl. Sci.*, vol. 66, no. 7, pp. 1694–1701, 2019.

[108] A. Ildefonso, Z. E. Fleetwood, G. N. Tzintzarov, J. M. Hales, D. Nergui, M. Frounchi, A. Khachatrian, S. P. Buchner, D. McMorrow, J. H. Warner, J. Harms, A. Erickson, K. Voss, V. Ferlet-Cavrois, and J. D. Cressler, "Optimizing Optical Parameters to Facilitate Correlation of Laser-and Heavy-Ion-Induced Single-Event Transients in SiGe HBTs," *IEEE Trans. Nucl. Sci.*, vol. 66, no. 1, pp. 359–367, 2019.

[109] J. M. Hales, A. Khachatrian, S. Buchner, J. Warner, A. Ildefonso, G. N. Tzintzarov, D. Nergui, D. M. Monahan, J. D. Lalumondiere, Stephen Cressler, and D. Mcmorrow, "New Approach for Pulsed-Laser Testing That Mimics Heavy-Ion Charge Deposition Profiles," *IEEE Trans. Nucl. Sci.*, vol. 67, no. 1, pp. 81–90, Jan. 2020.

[110] J. M. Hales, A. Khachatrian, J. Warner, S. Buchner, A. Ildefonso, G. N. Tzintzarov, D. Nergui, D. M. Monahan, S. D. LaLumondiere, J. D. Cressler, and D. McMorrow, "Using Bessel beams and two-photon absorption to predict radiation effects in microelectronics," *Opt. Express*, vol. 27, no. 26, p. 37652, 2019.

[111] D. I. Kovsh, S. Yang, D. J. Hagan, and E. W. Van Stryland, "Nonlinear optical beam propagation for optical limiting," *Appl. Opt.*, vol. 38, no. 24, p. 5168, 1999.

[112] J. M. Hales, N. J. H. Roche, A. Khachatrian, D. McMorrow, S. Buchner, J. Warner, M. Turowski, K. Lilja, N. C. Hooten, E. X. Zhang, R. A. Reed, and R. D. Schrimpf, "Two-Photon Absorption Induced Single-Event Effects: Correlation between Experiment and Simulation," *IEEE Trans. Nucl. Sci.*, vol. 62, no. 6, pp. 2867–2873, 2015.

[113] L. D. Ryder, K. L. Ryder, A. L. Sternberg, J. A. Kozub, H. Gong, E. X. Zhang, D. Linten, J. Mitard, R. A. Weller, R. D. Schrimpf, S. M. Weiss, and R. A. Reed, "Polarization Dependence of Pulsed Laser-Induced SEEs in SOI FinFETs," *IEEE Trans. Nucl. Sci.*, vol. 67, no. 1, pp. 38–43, Jan. 2020.

[114] M. S. Min and C. H. Teng, "The Instability of the Yee Scheme for the 'Magic Time Step,'" *J. Comput. Phys.*, vol. 166, no. 2, pp. 418–424, 2001.

[115] K. Aydin, V. E. Ferry, R. M. Briggs, and H. A. Atwater, "Broadband polarization-independent resonant light absorption using ultrathin plasmonic super absorbers," *Nat. Commun.*, vol. 2, no. 1, pp. 1–7, 2011.

[116] E. Simoen, M. Gaillardin, P. Paillet, R. A. Reed, R. D. Schrimpf, M. L. Alles, F. El-Mamouni, D. M. Fleetwood, A. Griffoni, and C. Claeys, "Radiation effects in advanced multiple gate and silicon-on-insulator transistors," *IEEE Trans. Nucl. Sci.*, vol. 60, no. 3, pp. 1970–1991, 2013.

[117] P. Wang, A. L. Sternberg, J. A. Kozub, E. X. Zhang, N. A. Dodds, S. L. Jordan, D. M. Fleetwood, R. A. Reed, and R. D. Schrimpf, "Analysis of TPA Pulsed-Laser-Induced Single-Event Latchup Sensitive-Area," *IEEE Trans. Nucl. Sci.*, vol. 65, no. 1, pp. 502–509, 2018.

[118] D. McMorrow, W. T. Lotshaw, J. S. Melinger, S. Buchner, Y. Boulghassoul, L. W. Massengill, and R. L. Pease, "Three-Dimensional Mapping of Single-Event Effects Using Two Photon Absorption," *IEEE Trans. Nucl. Sci.*, vol. 50, no. 6 I, pp. 2199–2207, 2003.

[119] K. Ni, A. L. Sternberg, E. X. Zhang, J. A. Kozub, R. Jiang, R. D. Schrimpf, R. A. Reed, D. M. Fleetwood, M. L. Alles, D. McMorrow, J. Lin, A. Vardi, and J. Del Alamo, "Understanding Charge Collection Mechanisms in InGaAs FinFETs Using High-Speed Pulsed-Laser Transient Testing with

Tunable Wavelength," *IEEE Trans. Nucl. Sci.*, vol. 64, no. 8, pp. 2069–2078, 2017.

[120] H. Gong, K. Ni, E. X. Zhang, A. L. Sternberg, J. A. Kozub, M. L. Alles, R. A. Reed, D. M. Fleetwood, R. D. Schrimpf, N. Waldron, B. Kunert, and D. Linten, "Pulsed-Laser Induced Single-Event Transients in InGaAs FinFETs on Bulk Silicon Substrates," *IEEE Trans. Nucl. Sci.*, vol. 66, no. 1, pp. 376–383, 2019.

[121] J. M. Hales, N. J. H. Roche, A. Khachatrian, D. McMorrow, S. Buchner, J. Warner, M. Turowski, K. Lilja, N. C. Hooten, E. X. Zhang, R. A. Reed, and R. D. Schrimpf, "Strong Correlation Between Experiment and Simulation for Two-Photon Absorption Induced Carrier Generation," *IEEE Trans. Nucl. Sci.*, vol. 64, no. 5, pp. 1133–1136, 2017.

[122] J. A. Schuller, E. S. Barnard, W. Cai, Y. C. Jun, J. S. White, and M. L. Brongersma, "Plasmonics for extreme light concentration and manipulation," *Nat. Mater.*, vol. 9, no. 3, pp. 193–204, 2010.

[123] S. Gwo, C. Y. Wang, H. Y. Chen, M. H. Lin, L. Sun, X. Li, W. L. Chen, Y. M. Chang, and H. Ahn, "Plasmonic Metasurfaces for Nonlinear Optics and Quantitative SERS," *ACS Photonics*, vol. 3, no. 8, pp. 1371–1384, 2016.

[124] J. Langer, S. M. Novikov, and L. M. Liz-Marzán, "Sensing using plasmonic nanostructures and nanoparticles," *Nanotechnology*, vol. 26, no. 32, 2015.

[125] H. Choo, M. K. Kim, M. Staffaroni, T. J. Seok, J. Bokor, S. Cabrini, P. J. Schuck, M. C. Wu, and E. Yablonovitch, "Nanofocusing in a metal-insulator-metal gap plasmon waveguide with a three-dimensional linear taper," *Nat. Photonics*, vol. 6, no. 12, pp. 838–844, 2012.

[126] T. Chiarella, L. Witters, A. Mercha, C. Kerner, M. Rakowski, C. Ortolland, L. A. Ragnarsson, B. Parvais, A. De Keersgieter, S. Kubicek, A. Redolfi, C. Vrancken, S. Brus, A. Lauwers, P. Absil, S. Biesemans, and T. Hoffmann, "Benchmarking SOI and bulk FinFET alternatives for PLANAR CMOS scaling succession," *Solid. State. Electron.*, vol. 54, no. 9, pp. 855–860, 2010.

[127] N. C. Hooten, "Charge collection mechanisms in silicon devices during high-level carrier generation events," Ph.D. dissertation, Dept. Elect. Eng. Comput. Sci., Vanderbilt Univ., Nashville, TN, USA, 2014.

[128] J. A. Pellish, R. A. Reed, D. Mcmorrow, J. S. Melinger, P. Jenkins, A. K. Sutton, R. M. Diestelhorst, S. D. Phillips, J. D. Cressler, V. Pouget, N. D. Pate, J. A. Kozub, M. H. Mendenhall, R. A. Weller, S. Member, R. D. Schrimpf, P. W. Marshall, A. D. Tipton, and G. Niu, "Laser-Induced Current Transients in Silicon-Germanium HBTs," *IEEE Trans. Nucl. Sci.*, vol. 55, no. 6, pp. 2936–2942, Dec. 2008.

[129] W. L. Barnes, A. Dereux, and T. W. Ebbesen, "Surface plasmon subwavelength optics," *Nature*, vol. 424, no. 6950, pp. 824–830, 2003.

[130] S. Jahani and Z. Jacob, "All-dielectric metamaterials," *Nat. Nanotechnol.*, vol. 11, no. 1, pp. 23–36, 2016.

[131] H. Hu, X. Zeng, D. Ji, L. Zhu, and Q. Gan, "Efficient end-fire coupling of surface plasmons on flat metal surfaces for improved plasmonic Mach-Zehnder interferometer," *J. Appl. Phys.*, vol. 113, no. 5, 2013.

[132] T. Nikolajsen, K. Leosson, I. Salakhutdinov, and S. I. Bozhevolnyi, “Polymer-based surface-plasmon-polariton stripe waveguides at telecommunication wavelengths,” *Appl. Phys. Lett.*, vol. 82, no. 5, pp. 668–670, 2003.

[133] B. Wang and P. Lalanne, “Surface plasmon polaritons locally excited on the ridges of metallic gratings,” *Opt. Soc. Am. A*, vol. 27, no. 6, pp. 1432–1441, 2010.

[134] H. Liu, P. Lalanne, X. Yang, and J. P. Hugonin, “Surface plasmon generation by subwavelength isolated objects,” *IEEE J. Sel. Top. Quantum Electron.*, vol. 14, no. 6, pp. 1522–1529, 2008.

[135] S. Zhu, G. Q. Lo, and D. L. Kwong, “Phase modulation in horizontal metal-insulator-silicon-insulator-metal plasmonic waveguides,” *Opt. Express*, vol. 21, no. 7, p. 8320, 2013.

[136] E. X. Jin and X. Xu, “Plasmonic effects in near-field optical transmission enhancement through a single bowtie-shaped aperture,” *Appl. Phys. B Lasers Opt.*, vol. 84, no. 1–2, pp. 3–9, 2006.

[137] M. Wu, Z. Han, and V. Van, “Conductor-gap-silicon plasmonic waveguides and passive components at subwavelength scale,” *Opt. Express*, vol. 18, no. 11, p. 11728, 2010.

[138] C. L. C. Smith, N. Stenger, A. Kristensen, N. A. Mortensen, and S. I. Bozhevolnyi, “Gap and channeled plasmons in tapered grooves: A review,” *Nanoscale*, vol. 7, no. 21, pp. 9355–9386, 2015.

[139] Ansys. Lumerical MODE. Accessed: Apr. 2021. [Online]. Available: https://www.lumerical.com/products/mode/

[140] D. Thomson, A. Zilkie, J. E. Bowers, T. Komljenovic, G. T. Reed, L. Vivien, D. Marris-Morini, E. Cassan, L. Virot, J. M. Fédéli, J. M. Hartmann, J. H. Schmid, D. X. Xu, F. Boeuf, P. O’Brien, G. Z. Mashanovich, and M. Nedeljkovic, “Roadmap on silicon photonics,” *J. Opt. (United Kingdom)*, vol. 18, no. 7, p. 073003, Jun. 2016.

[141] P. Absil, P. De Heyn, H. Chen, P. Verheyen, G. Lepage, M. Pantouvaki, J. De Coster, A. Khanna, Y. Drissi, D. Van Thourhout, and J. Van Campenhout, “Imec iSiPP25G silicon photonics: a robust CMOS-based photonics technology platform,” in *Silicon Photonics X*, 2015, vol. 9367, no. February 2015, p. 93670V.

[142] A. E. J. Lim, J. Song, Q. Fang, C. Li, X. Tu, N. Duan, K. K. Chen, R. P. C. Tern, and T. Y. Liow, “Review of Silicon Photonics Foundry Efforts,” *IEEE J. Sel. Top. Quantum Electron.*, vol. 20, no. 4, pp. 405–416, Aug. 2014.

[143] G. N. Tzintzarov, A. Ildefonso, J. W. Teng, M. Frounchi, A. Djikeng, P. Iyengar, P. S. Goley, A. Khachatrian, J. Hales, R. Bahr, S. P. Buchner, D. McMorrow, and J. D. Cressler, “Optical Single-Event Transients Induced in Integrated Silicon-Photonic Waveguides by Two-Photon Absorption,” *IEEE Trans. Nucl. Sci.*, vol. XX, no. XX, pp. 1–8, 2021.

[144] P. S. Goley, G. N. Tzintzarov, S. Zeinolabedinzadeh, A. Ildefonso, K. Motoki, R. Jiang, E. X. Zhang, D. M. Fleetwood, L. Zimmermann, M. Kaynak, S. Lischke, C. Mai, and J. D. Cressler, “Total ionizing dose effects in 70-GHz bandwidth photodiodes in a SiGe integrated photonics platform,” *IEEE Trans. Nucl. Sci.*, vol. 66, no. 1, pp. 125–133, Jan. 2019.

[145] P. S. Goley, N. A. Dodds, M. Frounchi, G. N. Tzintzarov, R. N. Nowlin, and J. D. Cressler,

"Response of Waveguide-Integrated Germanium-on-Silicon p-i-n Photodiodes to Neutron Displacement Damage," *IEEE Trans. Nucl. Sci.*, vol. 67, no. 1, pp. 296–304, Jan. 2020.

[146] H. Chen, P. Verheyen, P. De Heyn, G. Lepage, J. De Coster, S. Balakrishnan, P. Absil, G. Roelkens, and J. Van Campenhout, "Dark current analysis in high-speed germanium p-i-n waveguide photodetectors," *J. Appl. Phys.*, vol. 119, no. 21, p. 213105, Jun. 2016.

[147] H. T. Chen, P. Verheyen, P. De Heyn, G. Lepage, J. De Coster, P. Absil, G. Roelkens, and J. Van Campenhout, "High-responsivity low-voltage 28-Gb/s Ge p-i-n photodetector with silicon contacts," *J. Light. Technol.*, vol. 33, no. 4, pp. 820–824, Feb. 2015.

[148] P. Absil, K. Croes, A. Lesniewska, P. De Heyn, Y. Ban, B. Snyder, J. De Coster, F. Fodor, and V. Simons, "Reliable 50Gb / s Silicon Photonics Platform for Next- Generation Data Center Optical Interconnects," in *IEEE International Electron Devices Meeting*, 2017, pp. 761–764.

[149] J. S. Melinger, S. Buchner, D. Mcmorrow, W. J. Stapor, T. R. Weatherford, and A. B. Campbell, "CRITICAL EVALUATION OF THE PULSED LASER METHOD FOR SINGLE EVENT EFFECTS TESTING AND FUNDAMENTAL STUDIES," *IEEE Trans. Nucl. Sci.*, vol. 41, no. 6, pp. 2574–2584, Dec. 1994.

[150] S. Lischke, D. Knoll, C. Mai, L. Zimmermann, A. Peczek, M. Kroh, A. Trusch, E. Krune, K. Voigt, and A. Mai, "High bandwidth, high responsivity waveguide-coupled germanium p-i-n photodiode," *Opt. Express*, vol. 23, no. 21, pp. 27213–27220, Oct. 2015.

[151] A. Ildefonso, G. N. Tzintzarov, D. Nergui, A. P. Omprakash, P. S. Goley, J. M. Hales, A. Khachatrian, S. P. Buchner, D. McMorrow, J. H. Warner, and J. D. Cressler, "Comparison of single-event transients in SiGe HBTs on Bulk and Thick-Film SOI," *IEEE Trans. Nucl. Sci.*, vol. 67, no. 1, pp. 71–80, Jan. 2020.

[152] J. E. Bowers and C. A. Burrus, "Ultrawide-Band Long-Wavelength p-i-n Photodetector," *J. Light. Technol.*, vol. 5, no. 10, pp. 1339–1350, Oct. 1987.

[153] J. Michel, J. Liu, and L. C. Kimerling, "High-performance Ge-on-Si photodetectors," *Nat. Photonics*, vol. 4, no. 8, pp. 527–534, Aug. 2010.

[154] L. Virot, L. Vivien, J. M. Fédéli, Y. Bogumilowicz, J. M. Hartmann, F. Boeuf, P. Crozat, D. Marris-Morini, and E. Cassan, "High-performance waveguide-integrated germanium PIN photodiodes for optical communication applications," *Photonics Res.*, vol. 1, no. 3, pp. 140–147, Oct. 2013.

[155] D. Feng, S. Liao, P. Dong, N. N. Feng, H. Liang, D. Zheng, C. C. Kung, J. Fong, R. Shafiiha, J. Cunningham, A. V. Krishnamoorthy, and M. Asghari, "High-speed Ge photodetector monolithically integrated with large cross-section silicon-on-insulator waveguide," *Appl. Phys. Lett.*, vol. 95, no. 26, pp. 15–18, Dec. 2009.

[156] A. Palmieri, M. Vallone, M. Calciati, F. Bertazzi, M. Goano, and G. Ghione, "Effect of Saturation Velocity in Germanium p-i-n Photodetectors," in *19th Italian National Conference on Photonic Technologies (Fotonica 2017)*, 2017, pp. 21–24.

[157] L. Virot, D. Benedikovic, B. Szelag, C. Alonso-Ramos, B. Karakus, J.-M. Hartmann, X. Le Roux, P. Crozat, E. Cassan, D. Marris-Morini, C. Baudot, F. Boeuf, J.-M. Fédéli, C. Kopp, and L. Vivien,

"Integrated waveguide PIN photodiodes exploiting lateral Si/Ge/Si heterojunction," *Opt. Express*, vol. 25, no. 16, pp. 19487–19496, Aug. 2017.

[158] H. Chen, P. Verheyen, P. De Heyn, G. Lepage, J. De Coster, S. Balakrishnan, P. Absil, W. Yao, L. Shen, G. Roelkens, and J. Van Campenhout, "−1 V bias 67 GHz bandwidth Si-contacted germanium waveguide p-i-n photodetector for optical links at 56 Gbps and beyond," *Opt. Express*, vol. 24, no. 5, pp. 4622–4631, Feb. 2016.

[159] G. Guo, T. Hirao, J. S. Laird, S. Onoda, T. Wakasa, T. Yamakawa, and T. Kamiya, "Temperature dependence of single-event transient current induced by heavy-ion microbeam on p+/n/n+ epilayer junctions," *IEEE Trans. Nucl. Sci.*, vol. 51, no. 5, pp. 2834–2839, Oct. 2004.

[160] Q. Lin, O. J. Painter, and G. P. Agrawal, "Nonlinear optical phenomena in silicon waveguides: modeling and applications," *Opt. Express*, vol. 15, no. 25, p. 16604, 2007.

[161] C. Li, R. Bai, A. Shafik, E. Z. Tabasy, B. Wang, G. Tang, C. Ma, C. H. Chen, Z. Peng, M. Fiorentino, R. G. Beausoleil, P. Chiang, and S. Palermo, "Silicon photonic transceiver circuits with microring resonator bias-based wavelength stabilization in 65 nm CMOS," *IEEE J. Solid-State Circuits*, vol. 49, no. 6, pp. 1419–1436, 2014.

[162] K. J. Miller, R. F. Haglund, and S. M. Weiss, "Optical phase change materials in integrated silicon photonic devices: review," *Opt. Mater. Express*, vol. 8, no. 8, p. 2415, 2018.

[163] J. Liu, M. Beals, A. Pomerene, S. Bernardis, R. Sun, J. Cheng, L. C. Kimerling, and J. Michel, "Waveguide-integrated, ultralow-energy GeSi electro-absorption modulators," *Nat. Photonics*, vol. 2, no. 7, pp. 433–437, 2008.

[164] O. Fageeha, J. Howard, and R. C. Block, "Distribution of radial energy deposition around the track of energetic charged particles in silicon," *J. Appl. Phys.*, vol. 75, no. 5, pp. 2317–2321, 1994.

[165] W. J. Stapor and P. T. McDonald, "Practical approach to ion track energy distribution," *J. Appl. Phys.*, vol. 64, no. 9, pp. 4430–4434, 1988.

[166] M. Raine, G. Hubert, M. Gaillardin, L. Artola, P. Paillet, S. Girard, J. E. Sauvestre, and A. Bournel, "Impact of the radial ionization profile on SEE prediction for SOI transistors and SRAMs beyond the 32-nm technological node," *IEEE Trans. Nucl. Sci.*, vol. 58, no. 3, pp. 840–847, Jun. 2011.

[167] L. D. Ryder, R. A. Reed, and S. M. Weiss, "Photonics in Extreme Environments: High Energy Radiation-Induced Optical Response in Silicon Waveguides," in *Conference on Lasers and Electro-Optics*, 2021, p. To be published.

[168] F. El-Mamouni, E. X. Zhang, D. R. Ball, B. Sierawski, M. P. King, R. D. Schrimpf, R. A. Reed, M. L. Alles, D. M. Fleetwood, D. Linten, E. Simoen, and G. Vizkelethy, "Heavy-ion-induced current transients in bulk and SOI FinFETs," *IEEE Trans. Nucl. Sci.*, vol. 59, no. 6, pp. 2674–2681, 2012.

[169] T. Tanabe, M. Notomi, S. Mitsugi, A. Shinya, and E. Kuramochi, "All-optical switches on a silicon chip realized using photonic crystal nanocavities," *Appl. Phys. Lett.*, vol. 87, no. 15, pp. 1–3, 2005.

[170] K. Nozaki, T. Tanabe, A. Shinya, S. Matsuo, T. Sato, H. Taniyama, and M. Notomi, "Sub-femtojoule all-optical switching using a photonic-crystal nanocavity," *Nat. Photonics*, vol. 4, no. 7,

pp. 477–483, 2010.

[171] D. Dimitropoulos, R. Jhaveri, R. Claps, J. C. S. Woo, and B. Jalali, "Lifetime of photogenerated carriers in silicon-on-insulator rib waveguides," *Appl. Phys. Lett.*, vol. 86, no. 7, pp. 1–3, 2005.

[172] A. M. Tonigan, D. Ball, G. Vizkelethy, J. Black, D. Black, J. Trippe, E. Bielejec, M. L. Alles, R. Reed, and R. D. Schrimpf, "Impact of Surface Recombination on Single-Event Charge Collection in an SOI Technology," *IEEE Trans. Nucl. Sci.*, vol. 68, no. 3, pp. 305–311, 2021.

[173] I. Sanchez Esqueda, H. J. Barnaby, and M. P. King, "Compact modeling of total ionizing dose and aging effects in MOS technologies," *IEEE Trans. Nucl. Sci.*, vol. 62, no. 4, pp. 1501–1515, 2015.

[174] Ansys. Lumerical INTERCONNECT. Accessed: Apr. 2021. [Online]. Available: https://www.lumerical.com/products/interconnect/.

[175] J. M. Hales, A. Khachatrian, S. Buchner, N. J. H. Roche, J. Warner, and D. McMorrow, "A simplified approach for predicting pulsed-laser-induced carrier generation in semiconductor," *IEEE Trans. Nucl. Sci.*, vol. 64, no. 3, pp. 1006–1013, 2017.